3-2007

Dynamic Response of a Collidant Impacting a Low Pressure Airbag

Peter A. Dreher

Dynamic Response of a Collidant Impacting a Low Pressure Airbag

DISSERTATION

Peter A. Dreher P.E.

AFIT/DS/ENY/07-09

DEPARTMENT OF THE AIR FORCE
AIR UNIVERSITY

AIR FORCE INSTITUTE OF TECHNOLOGY

Wright-Patterson Air Force Base, Ohio

The views expressed in this Dissertation are those of the author and do not reflect the official policy or position of the United States Air Force, Department of Defense, or the United States Government.

AFIT/DS/ENY/07-09

Dynamic Response of a Collidant Impacting a Low Pressure Airbag

DISSERTATION

Presented to the Faculty

Graduate School of Engineering and Management

Air Force Institute of Technology

Air University

Air Education and Training Command

In Partial Fulfillment of the Requirements for the

Degree of Doctor of Philosophy

Peter A. Dreher P.E., BSME, BSChE, BSNE, MSME, MBA

March 2007

AFIT/DS/ENY/07-09

Dynamic Response of a Collidant Impacting a Low Pressure Airbag

DISSERTATION

Peter A. Dreher P.E., BSME, BSChE, BSNE, MSME, MBA

Approved:

	Date
_____	_____
Robert A. Canfield (Chairman)	
_____	_____
Raymond C. Maple (Member)	
_____	_____
Mark E. Oxley (Member)	
_____	_____
Peter S. Maybeck (Dean's Representative)	

Accepted:

_____	_____
M. U. Thomas	Date
Dean, Graduate School of Engineering and Management	

Table of Contents

List of Figures

Abstract

There are many uses of low pressure airbags, both military and commercial. Many of these applications have been hampered by inadequate and inaccurate modeling tools.

This dissertation contains the derivation of a four degree-of-freedom system of differential equations from physical laws of mass and energy conservation, force equilibrium, and the Ideal Gas Law. Kinematic equations were derived to model a cylindrical airbag as a single control volume impacted by a parallelepiped collidant. An efficient numerical procedure was devised to solve the simplified system of equations in a manner amenable to discovering design trends. The largest public airbag experiment, both in scale and scope, was designed and built to collect data on low-pressure airbag responses, otherwise unavailable in the literature. The experimental results were compared to computational simulations to validate the simplified numerical model. Experimental response trends are presented that will aid airbag designers. The two objectives of using a low pressure airbag to demonstrate the feasibility to 1) accelerate a munition to 15 feet per second velocity from a bomb bay, and 2) decelerate humans hitting trucks below the human tolerance level of 50 G's, were both met.

DYNAMIC RESPONSE OF A COLLIDANT IMPACTING A LOW PRESSURE AIRBAG

Chapter I: Introduction

This dissertation addresses two practical applications of airbags in the real world. The first is accurately and efficiently modeling bumper airbags for trucks and buses to reduce the injuries and deaths of pedestrians and people in smaller vehicles hit by trucks and buses. The second problem is accurately and efficiently modeling airbags for ejecting munitions (bombs and missiles) from bomb bays. See Figures 1-1 for examples of these airbag applications.

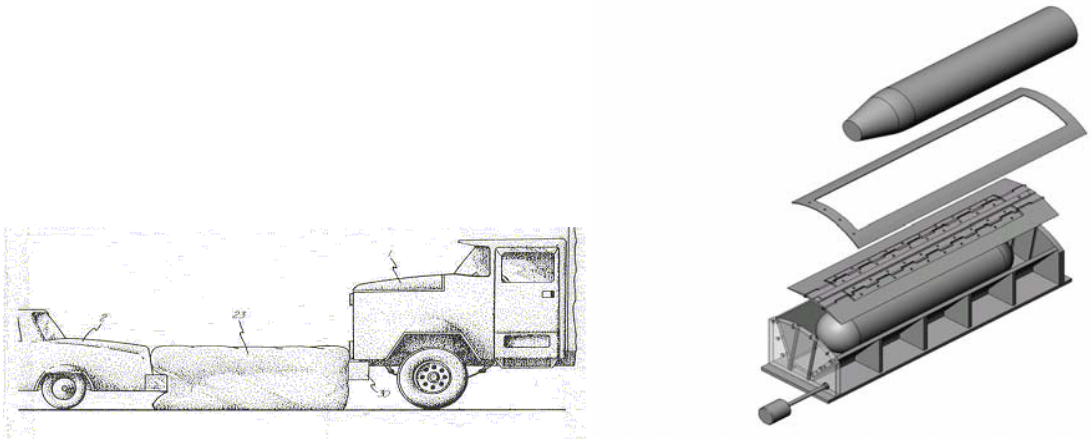

Figure 1-1: Low Pressure Airbag Applications

Objective: The objectives of this research were to demonstrate that airbags at low pressure could:

1. Accelerate a munition to 15 feet per second in a bomb bay
2. Decelerate humans hitting trucks at less than the human tolerance level of 50 Gs.

Airbags are one of the most difficult devices in mechanical engineering to model, and hence design. The physics of the fluids interacting with viscoelastic airbags that stretch and leak does not lend itself to the type of closed-form, analytical equations that can precisely model the behavior of many mechanical or fluid systems. The only way engineers have been able to model airbags is with non-linear, finite element, computer codes or numerical approximation [1-1]. The agreement of these models with experiments in the literature has shown errors from 14% to 174% even for models with hundreds of thousands of degrees-of-freedom. These codes can take thousands of processor hours to calculate the dynamic response of a single collidant hitting a single airbag.

A run of one of these finite element codes produces the solution to one specific geometry and set of initial conditions. The user must guess what airbag parameters to change, which direction, and how much, to get better airbag performance.

As a result, only a few large organizations, such as Delphi and AutoLiv, the largest airbag manufacturers and automakers, have made the effort to model airbag response. These firms use the non-linear dynamics, finite element program, LSDyna, from Livermore Systems Technology Corporation (LSTC) [1-1]. To save computer time, they

often use a simplified inflation process rather than the more accurate Arbitrary Lagrangian Eulerian method [1-1]. Nevertheless, LSDyna, the computers to run it, the training to operate it, and the engineers to run it are all expensive.

Low pressure airbags would more likely reach their full potential benefit to society if they could be designed with only a few hours of engineering effort on personal computers rather than weeks of effort on supercomputers.

This dissertation explores some of the fundamental physics of airbag behavior that support the creation of just such airbag design and optimization tools applicable for most low pressure airbag applications. This dissertation will focus on one basic use of the airbag. The use is as an absorber of kinetic energy of a moving object. The airbag catches the moving object and reduces its kinetic energy, thereby slowing it down. The moving object hitting an absorber will be called a collidant. The rebound of the collidant is equivalent to an ejection. The conditions at the bottom of the impact cycle represent initial conditions for an ejector. The rebound stroke will be equal to an ejection stroke.

Traditional design uses equations for performance parameters or responses. Some widely sought responses for airbag systems acting as absorbers are:

- Collidant acceleration
- Collidant change in kinetic energy
- Membrane stress in airbag
- Peak airbag pressure

These various responses could be maximized, minimized, or constrained as desired by the engineer trying to optimize an airbag system. These response equations will use key airbag system design choices as inputs. These design choices will be called design

factors. They are simple system parameters measured before a device performs its function, such as:

- Airbag initial length, width, height, porosity, elastic modulus,
- Collidant mass, contact area & location

This dissertation proposes equations, so-called airbag response equations, for modeling the dynamic responses of a range of airbag and collidant sizes. A numerical routine was developed to solve the equations approximately. Experiments with collidants and airbags were run to verify the hypotheses through the numerical approximations.

Thesis Statement: Collidant accelerations and airbag pressure during a centered impact aligned with the longitudinal axis of a cylindrical, low-pressure airbag can be modeled accurately by means of the equations and approximations developed in Chapters 3 and 4.

This research results in the following contributions:

- Analytical equations for collidant acceleration as a function of airbag pressure, and for pressure as a function of time
- Kinematic equations for a single control volume model of a cylindrical airbag impacted by a parallelepiped collidant
- Development of an experimental apparatus for airbag pressure and acceleration testing
- Verification of the assumptions underlying the hypothetical equations and approximations by comparison of analytical results with experimental data

This dissertation is organized as follows:

1. Chapter 1 introduces the research.
2. Chapter 2 discusses prior work in airbags, particularly low pressure ones.
3. Chapter 3 develops the physics equations of the collision and airbag.
4. Chapter 4 develops the kinematics equations of the airbag engaging the collidant.
5. Chapter 5 develops the elasticity and permeability equations and details the airbag elasticity and permeability experiments and results.
6. Chapter 6 details the collision experiments and results.
7. Chapter 7 describes the numerical simulation of the collisions and details and compares the simulation results to the collision experimental results.
8. Chapter 8 makes conclusions and recommendations regarding this research.

Chapter II: Prior Work

The prior work has been divided into six sections. The first section is an historical overview of airbag or inflated membrane uses. The next section describes some prior work on airbags in the collidant impact absorber mode. The third section describes prior work on airbags in the projectile ejection mode. The fourth section describes work modeling membrane forces in inflatable buildings. The fifth section describes the state of the art in nonlinear airbag code validation attempts. The final section is a summary.

A. Early Airbag Uses

The airbag is one of the lightest weight structural tools and has had many applications. In 1783 in France, Joseph Montgolfier invented the balloon, a large airbag filled with enough hot air, to carry six men [2-1]. The rubber inflatable raft is an airbag with low permeability, used as a floatation device. In 1955, Goodyear invented an inflatable rubber airbag airplane large enough to carry two people and sold twelve [2-2].

In 1952, after an automobile crash with his wife, John Hetrick invented the car interior airbag to protect and decelerate occupants [2-3]. The Simplex Corporation invented a rubber-coated Kevlar airbag jack that can lift a 144,000 lb overturned railroad car or Abrams tank [2-4]. Eaton Corporation invented the air spring, a rubber cylindrical airbag for truck suspensions.

The US Air Force cluster bomb uses airbags to push bomblets away from each other and as ballutes to steer and aim the cluster bomb [2-5]. The US Army has experimented with airbags on Jeep airdrop pallets [2-6]. This program failed for lack of good airbag

design models. NASA and Martin-Baker Aircraft Company developed large airbags to cushion the impact of their Martian rovers [2-7].

In 1962, Aerospace Corporation invented an inflatable re-entry vehicle for a 1,000 lb payload [2-8]. In 1996, NASA launched a satellite with an inflatable antenna [2-9]. In 2000, Canadian Troy Hurtubise developed and demonstrated a bulletproof, airbag armor [2-10]. In 1996, Ohio engineer, Peter Dreher P.E. (the author), invented a bumper airbag for vehicles to reduce injury and damage from collisions [2-11]. This dissertation research emanated from that work. Some of the most salient work in airbag absorber and ejector applications is described below.

B. Absorber Characteristics

There are many applications for airbags used as absorbers. The car interior airbag is the most widely used absorber, with over 90 million manufactured each year and close to one billion on the road. These airbags range in size from 1 to 7 cubic feet and utilize porosity to control deflation rate. The truck air spring is probably the second most utilized with 120 million on the road. It is smaller, about a third of a cubic foot. Its fabric has zero porosity. Other impermeable membrane airbag applications such as bubble wrap packaging are quite popular, with billions sold.

The first Martian landing craft airbag, at 14 feet in diameter, is one of the largest absorber airbags ever made and used as such. Some inflatable antennas on spacecraft are over 100 feet in diameter and are impacted by micro-meteorites. New designs call for hardened skin that allows for meteorite perforation without collapse due to deflation. But new inflatable atmospheric re-entry vehicles use inflatable structures that will need to be

optimized for debris impacts. Some of the most appropriate literature in absorber airbag responses is discussed in the following sections.

1. Internal Vehicle Airbags.

a) Collision Physics and Human Injury.

Drs. Charles E. Strother and Richard M. Morgan of the National Highway Traffic Safety Administration (NHTSA) wrote a paper in 1974 [2-12] identifying the fundamental physics governing absorber airbag requirements in automobile collisions. Strother and Morgan identified occupant change in velocity (ΔV) and peak deceleration as proxies for the key responses of fatality, injury, and vehicle damage. They point out that most of the deaths and injuries come from frontal impacts. Regarding Figure 2-1 below, they say, "First, a significant percentage of the deaths (50-67%) and injuries (10-42%) fall above 30 mph. Secondly, if all injuries and fatalities resulting from frontal impacts at vehicle ΔV's of 50 mph or less could be eliminated, 98-100% of the all injuries and 92-98% of all deaths presently occurring in this mode would be prevented." Figure 2-1 shows cumulative percent injuries on the left and cumulative percent fatalities on the right from three different studies. The shaded area marks the range of the results and dashed lines represent a study result internal to this range and solid lines are study results on the edge of the range.

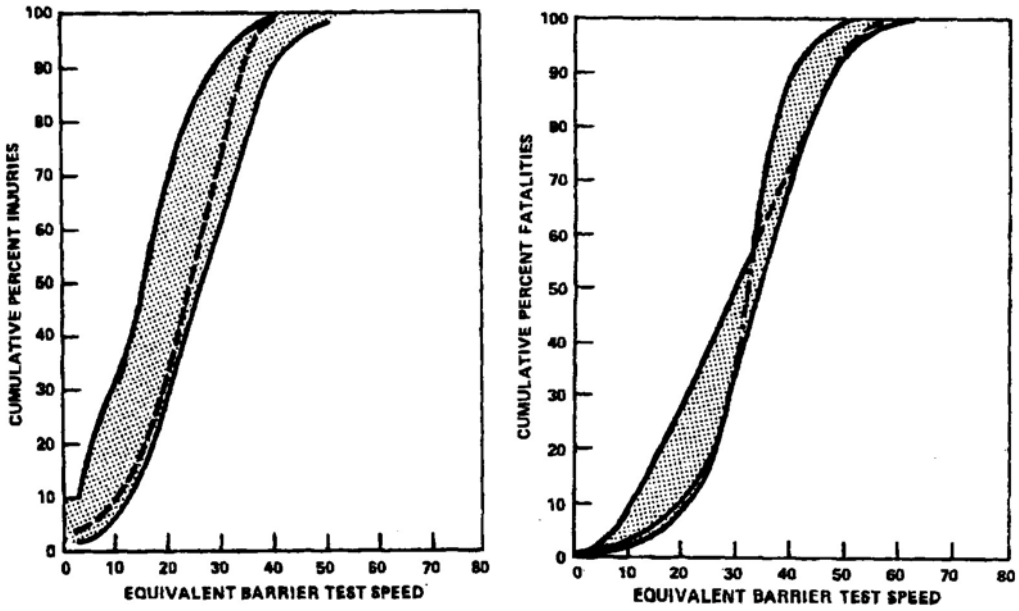

Figure 2-1: Injuries and Fatalities as a function of Speed (mph) into a Solid Barrier (with permission of authors) [2-12]

Strother and Morgan identified a key design factor affecting the responses collidant ΔV and peak acceleration. That design factor is stopping distance. "Protecting occupants in high-speed frontal impact simply involves making use of the available occupant stopping distance. This available occupant stopping distance exists in the form of interior distance, chest to dashboard separation, and in the form of exterior – bumper to firewall – displacement." They concluded that 80% of the bumper to firewall space could be crushed and 100% of the dashboard to chest space could be used for occupant deceleration and hence ΔV.

Strother and Morgan also concluded that this stopping distance had to be used efficiently. Efficiency meant that the occupant had to be at his upper end of deceleration tolerance for the whole stopping distance. Restraint systems had to be designed that

would achieve this high efficiency. They used hand calculations of Newton's Law to show the relationship of the responses to the design factors.

The Federal Motor Vehicle Safety Standard 208 (FMVSS 208) [2-13] specifies performance requirements for automobile interior airbags sold in the U.S. The airbag application is that of absorber of vehicle occupant kinetic energy. The Standard specifies which responses are important for this Absorber. These responses are vehicle occupant injury and fatality. Injury and fatality are measured by FMVSS 208 Head, Thoracic, Sternum, and Neck Injury Criteria.

The most restrictive Head Injury Criterion (HIC) is for the 1-year-old baby test. This test uses a baby test dummy with the acronym CRABI. The measurement is described in reference [2-13] as follows.

> "For any two points in time, t_1 and t_2, during the collision, which are separated by no more than a 15 millisecond interval and $t_1 < t_2$, the Head Injury Criterion HIC_{15}, shall be calculated using the resultant head acceleration, a, at the center of gravity of the dummy head expressed as a multiple of G, the acceleration due to gravity. HIC_{15} shall be calculated using the expression:
>
> $$\mathrm{HIC}_{15} = \left[\int_{t_1}^{t_2} a\,dt\right]^{2.5} \left(t_2 - t_1\right)^{-1.5} \qquad (2\text{-}1)$$
>
> HIC_{15} must not exceed 390 for a 1-year-old baby. For example, if the acceleration were constant at 50 Gs for the 15 milliseconds, HIC_{15} would be $50^{2.5} \times 0.015^{2.5} \times 0.015^{-1.5} = 265 < 390$."

The thoracic criterion for a 1-year-old dummy is that the thoracic instrumentation shall not exceed 50 Gs for more than 3 milliseconds. This is a tighter restriction than the HIC_{15}.

The Neck Injury Criterion, N_{ij}, is :

$$N_{ij} = (F_z / F_{zc}) + (M_{ocy} / M_{yc}) \leq 1 \qquad (2\text{-}2)$$

for any time during the crash. F_z is the axial force. It can be in tension or compression. F_{zc} is fixed at 328 lbf for a one-year-old whether tension or compression. In addition to the N_{ij} limit, $F_z \leq 175$ lbf for peak tension by law. And $F_z \leq 216$ lbf for peak compression, too. All these force limits place more than 50 Gs on the baby.

M_{ocy} is the Occipital Condyle Bending Moment. It can be either in flexion or extension whether the head is flipping forward or backward. It is detected by the upper neck load cell for the duration of the crash. M_{yc} is 32 lbf-ft for flexion and 13 lbf-ft for extension for a 1-year-old. The impact of a truck bumper is from the front and would generate a flexion moment.

The CRABI head is about 2 lbs and the moment arm from the shoulder to the occipital condyle is about 2 inches. The moment limit is 384 in-lbf. If the shoulders were rigidly secured to the seat, the force on the head would be 192 lbf or an acceleration of 96 Gs. This acceleration is above the 50 G limit set by the thorax.

Therefore, FMVSS 208 identifies the response of peak collidant deceleration as a good proxy for the responses of occupant injury and fatality. For the case of a bumper airbag hitting another vehicle, total collidant vehicle deceleration is the most appropriate response. If the whole vehicle is kept below the occupant allowable decelerations for all of the above criteria, the occupants will experience those decelerations or lower. Most

occupants are restrained by seatbelts and interior airbags, providing added flexibility and softening of the vehicle's deceleration. A reasonable response constraint is to keep the colliding vehicle deceleration below 50 Gs.

The FMVSS responses are based on cadaver tests with internal organ damage assessments. Translating those assessments into peak deceleration responses was done with hand calculations.

b) Car Interior Airbags.

Mr. Donald Nefske of the General Motors Research Laboratory developed a basic airbag physics model in 1971 and validated it with experiments [2-14]. His model used a permeable, elastic airbag of cylindrical shape, 3-feet long by 2-feet in diameter. He modeled the airbag inflating against a rectangular box. The airbag was laid on the floor with its major axis parallel to the floor. The box was mounted from two load cells above the airbag with its major axis also horizontal but perpendicular to the major axis of the airbag. The box was 18 inches wide by 42 inches long by 12 inches deep. It was mounted at various heights above the floor such that it would prevent the full inflation of the airbag, for instance, six, twelve, and 18 inches above the floor.

Nefske modeled and conducted static and dynamic inflation tests. The static tests used an impermeable liner. With a metering pump, he filled the airbag to various pressures against the box mounted at various heights Δ. He recorded the force on the box and the pressure and volume in the airbag at the various levels. He modeled the box force F as airbag pressure P times an experimentally derived effective area $A_{ef}(\Delta)$ at a given height Δ:

$$F = P \times A_{ef}\left(\Delta\right) \tag{2-3}$$

The force turned out to be a linear function of pressure, and the effective area turned out to be a linear function of box height. These experiments provided simple linear relationships for the model.

The airbag volume V varied with the box height and also with the airbag pressure as it stretched. The variation with box height was nonlinear, but the variation with pressure $b(\Delta)$ was approximately linear. Hence

$$V = V_0(\Delta) + Pb(\Delta) \tag{2-4}$$

These experiments provided simple relationships for the model.

The dynamic tests used the airbag without a liner. The airbag was nylon fabric coated with neoprene and fairly impermeable, having an experimentally estimated open area of 1.5 square inches at all pressure levels. One airbag had a 3-inch diameter vent hole on each end, the other airbag had none.

Nefske modeled the airbag thermodynamic system as a control volume containing only the air inside the airbag. He used the conservation of mass to calculate the gas mass in the airbag. He adjusted the effective orifice discharge coefficient until the simulation fit the experiments. He used the conservation of energy and the Ideal Gas Law to calculate the pressure in the airbag. He used a time step finite difference technique to integrate numerically the results of the inflating airbag against a stationary collidant.

Unlike Nefske, the present dissertation calculates airbag volume and surface area based on geometric shape assumptions. The air mass leak rate is calculated based on experimental fabric leak rates rather than using leak rate as an empirical factor to fit a simulation to an experiment as Nefske did. The present dissertation airbag pressure is dependent on more variables than the Nefske model. The collidant force is dependent on

more variables than the Nefske model and requires no static testing. The present dissertation models a moving collidant versus the static collidant of the Nefske model.

3. External Vehicle Airbags.

a) Car Bumper Airbags.

Dr. John Dreher PhD, P.E. and the author, Peter Dreher P.E., developed and patented an Absorber airbag called the Livvon Bumper Airbag. Figure 2-2 shows a drawing from the patent, [2-11].

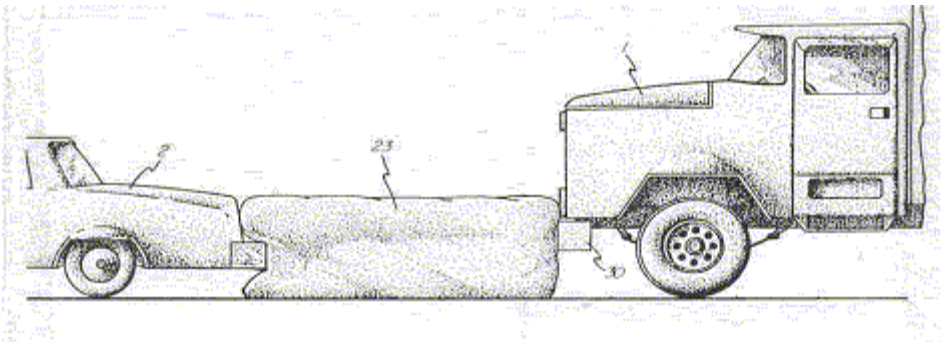

Figure 2–2: Bumper Airbag on a Truck hitting a Car (with permission of authors) [2-11]

They developed a 20-step mathematical model of a passenger vehicle colliding head-on into the front of a stationary truck of infinite mass, with an inflated bumper airbag. The 20-step math model runs in an Excel spreadsheet.

The main purpose of the 20-Step model was to determine what size airbag is necessary to achieve the change in collision velocity that Strother [2-12] described, i.e. 50 mph to 30 mph with an acceptable deceleration response level, vehicle mass, and airbag cost. The main responses of the 20-Step model are collidant peak deceleration and

change in collision velocity. Airbag pressure is also a response. It can be used to estimate the responses of airbag stress and burst potential.

Strother [2-12] identified stopping distance as the main design factor in any collision safety device. The bumper airbag adds stopping distance for the vehicle occupant beyond the existing bumper-to-firewall and chest-to-dashboard distance. The Drehers also identified this added stopping distance as one of the most important design factors of a bumper airbag.

The 20-Step model uses simple kinetics to do an inertial force balance on the colliding vehicles, and the Ideal Gas Law to determine the pressure in the airbag. The truck is treated as an infinitely rigid stationary barrier. The 20-Step model breaks the compression of the 5-foot long airbag into 20 three-inch compression steps rather than finite time steps. The time of each 3-inch step is approximated as the three inches divided by the collidant velocity at the beginning of each step. After each step of finite closing distance, several calculations are made. The force applied to the colliding vehicle during the step, decelerating it, was assumed to be the step starting pressure in the airbag times the face area of the collidant engaging the airbag. A new vehicle velocity was calculated based on this deceleration multiplied by the time of the step. A new airbag volume was calculated based on the three inches of collidant compression and the expanded diameter caused by the increased airbag pressure. The expanded diameter was based on a fabric elasticity provided by the fabric manufacturer's grab tensile tests. The volume of the ends of the airbag ballooning around the car face or under the truck bumper was neglected. A new airbag pressure was calculated based on the new reduced volume and some leaked air. The air leaked was based on the airbag exposed surface

area at the start of the step and the airbag pressure times a leak rate provided by the fabric manufacturer.

Based on the 20-Step model responses, the Drehers designed a bumper airbag with five key features:

1) The airbag is long enough to eliminate 90% of deaths, injuries, and vehicle damage.
2) It is designed as structurally efficient cylindrical pressure vessels that are easy to manufacture and conserve fabric.
3) The airbag major axis will buckle into a stable position against the road, because it is loaded off-center on the ends.
4) The airbag front face slant keeps it down when moving and pedestrians on top during a collision. The slanted-front airbag was tested up to 50 mph, and it stayed down.
5) The airbag has a controlled pressure release to keep collidant accelerations within allowable levels specified by the Federal Motor Vehicle Safety Standards.

The Drehers built prototypes and tested them. Figure 2-3 shows photographs of the experiments. The collision tests up to 20 mph showed approximately the predicted airbag compression and no damage to cars. The driver experienced no injuries.

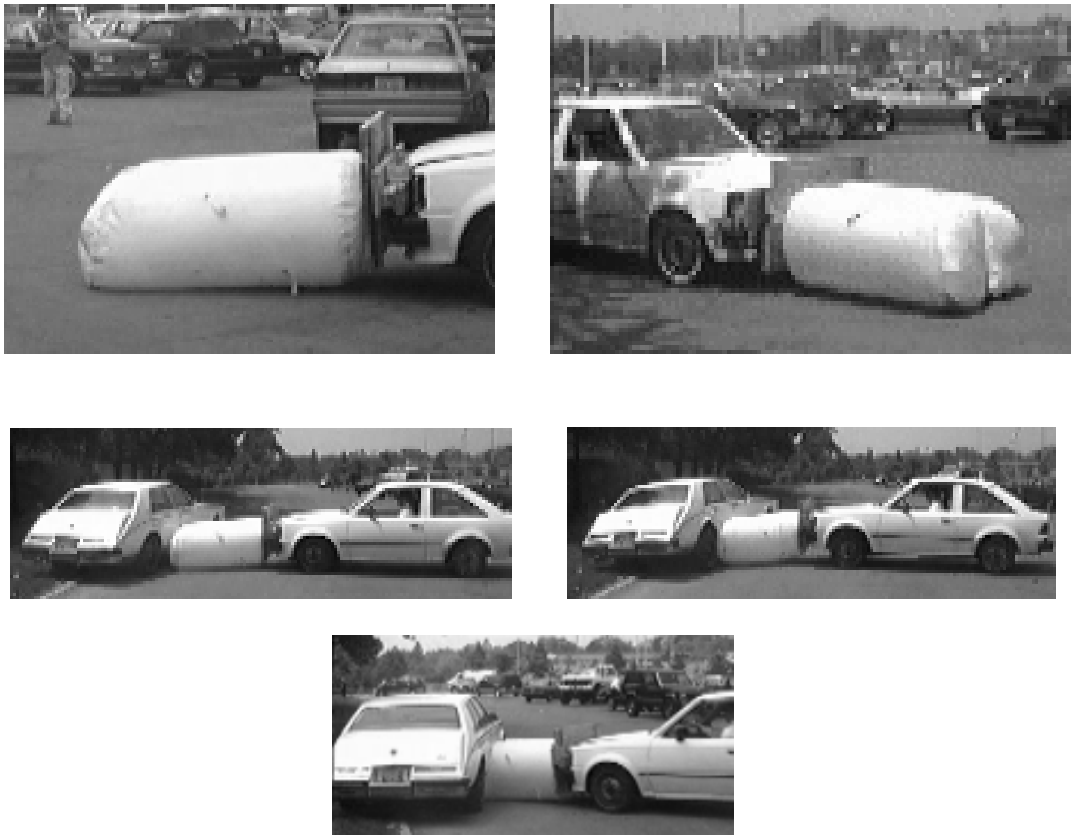

Figure 2-3: Photographs of Livvon Bumper Airbag Tests (with permission of authors) [2-11]

The Drehers identified the following responses as important to Absorber airbag performance:

- Collidant peak deceleration and change in velocity
- Airbag pressure, major axis buckling, bottoming out, aerodynamic lift
- Airbag system weight and cost

They identified the following design factors as significantly affecting those responses:

- Airbag initial length, width, and height
- Airbag porosity and elasticity
- Airbag initial pressure

- Collidant mass and initial velocity
- Collidant initial contact height and width

The present dissertation uses a time-accurate simulation rather than the Dreher's distance step model. It also accounts for the airbag end geometries in calculating leak surface area and volume.

b) Martian Spacecraft Landing Airbags.

Mr. C. S. Huxley-Reynard of the Martin-Baker Aircraft Company in Britain wrote a paper about optimizing airbags for the European Mars Lander spacecraft, Beagle, in 2000 [2-7]. See Figure 2-4 below for a three dimensional representation of this airbag system during a simulated Martian surface impact as rendered by LSDyna.

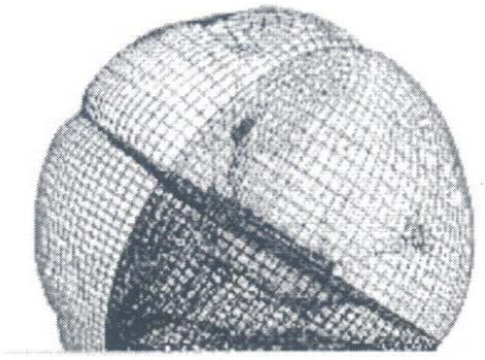

Figure 2-4: Martian Lander Airbag – LSDyna Simulation at Impact [2-7]

Huxley-Reynard optimized an airbag for a specific payload with specific dimensions. The optimization is only for segmented, spherical, impermeable, absorber airbags with spokes catching 60 kg collidants traveling at 20 meters per second. Figure 2-5 shows the airbag spokes.

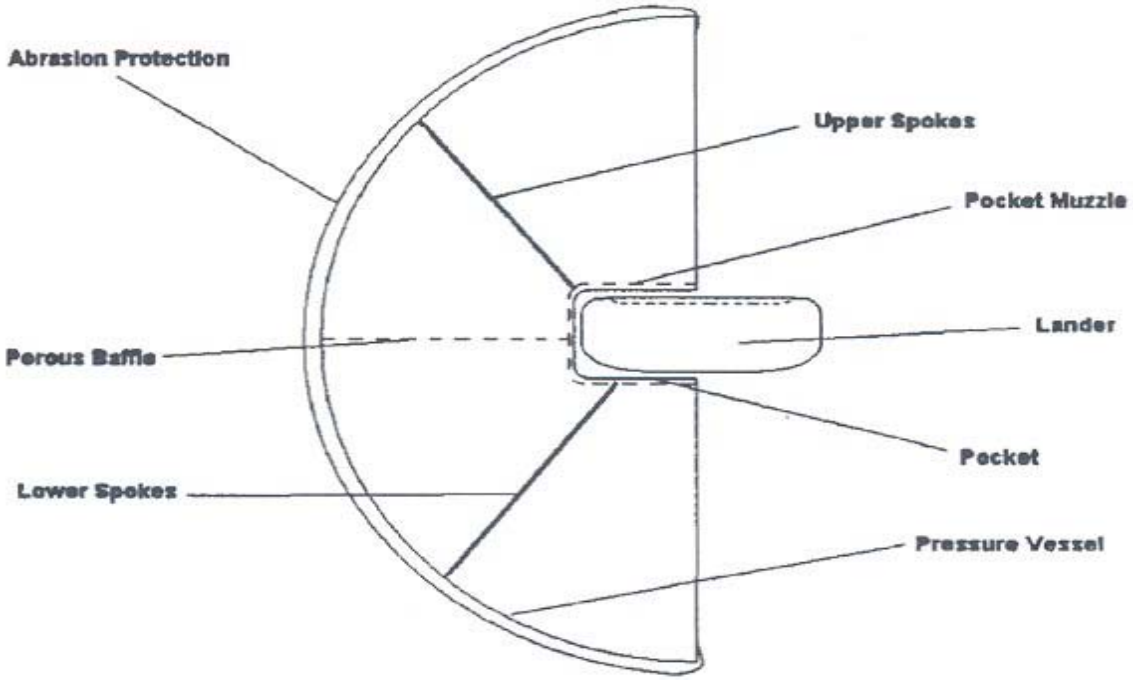

Figure 2-5: Airbag Segment Design with Upper and Lower Spokes (with permission of authors [2-7])

The collidants were disks, 0.6 meters in diameter and 0.2 meters thick. Figure 2-6 below depicts the disk shaped collidant.

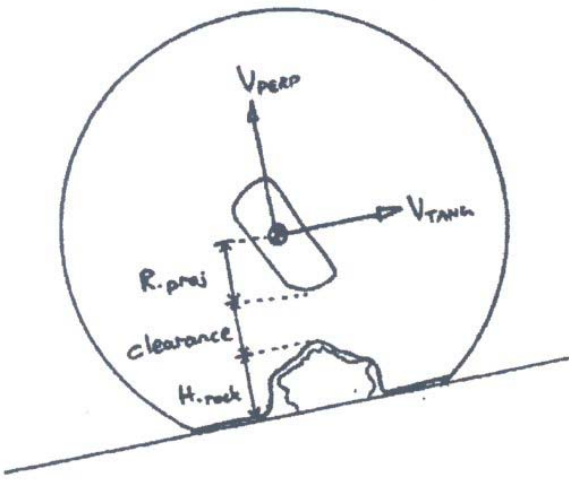

Figure 2-6: Disk shaped Collidant in an Airbag (with permission of authors [2-7])

The optimization constraint responses were:

- Prevent impact of the lander payload with the ground up until the moment of airbag jettison, i.e., limit airbag compression stroke
- Limit the collidant peak acceleration to < 200 Gs.

The only active design factors for this optimization were airbag diameter and airbag initial pressure. Airbag porosity was identified as a design factor. To maintain gas pressure in a porous airbag, make-up gas is required. The Martian Lander's inaccurate altimeters required early and sustained airbag inflation, and the weight of sufficient make-up gas for a porous airbag was too heavy. Hence only impermeable airbags were considered.

The optimization was done by graphing LSDyna output rather than developing airbag response equations. The author intuitively moved through the design space. Figure 2-7 below shows the constraint lines for the airbag compression stroke at impact and peak acceleration.

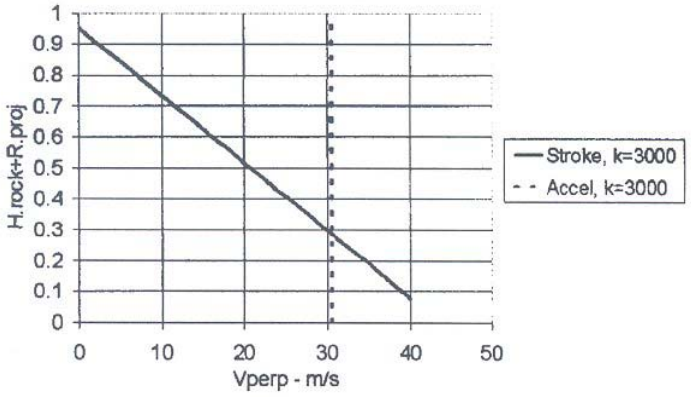

Figure 2-7: Constraint Response Graph (with permission of authors [2-7])

Several LSDyna simulations were run. Larger airbag diameter was better than smaller, but there was a limit to how high the payload could be off the ground when the airbags jettison. This constraint limited the airbag diameter to 1.95 meters.

Thus the only design factor optimized was airbag pressure. This optimization was done graphically on a 2-D graph populated by responses from LSDyna runs based on a Monte Carlo distribution of rock sizes on Mars. See Figure 2-8 below for this graph. The graph had lines for the stroke constraint and the acceleration constraint. The author concluded that a 1.95 meter diameter airbag inflated to 3.6 psia was optimal.

LSDyna is an explicit non-linear finite element code used for modeling airbags [1-1]. It uses thousands of tiny shell elements to model the airbag fabric. The volume inside the fabric surface is modeled as a thermodynamic open system control volume, using conservation of mass and energy and the Ideal Gas Law to solve for state variables. LSDyna requires the user to define the mass leak rate of air as a function of a state variable divided into linear segments. This approach makes a crucial variable a crude guess. Huxley-Reynard had no mass leaking of air from his impermeable airbag, avoiding this inaccuracy in LSDyna. The present dissertation strives to quantify the mass leak rate of air accurately based on fabric permeability properties.

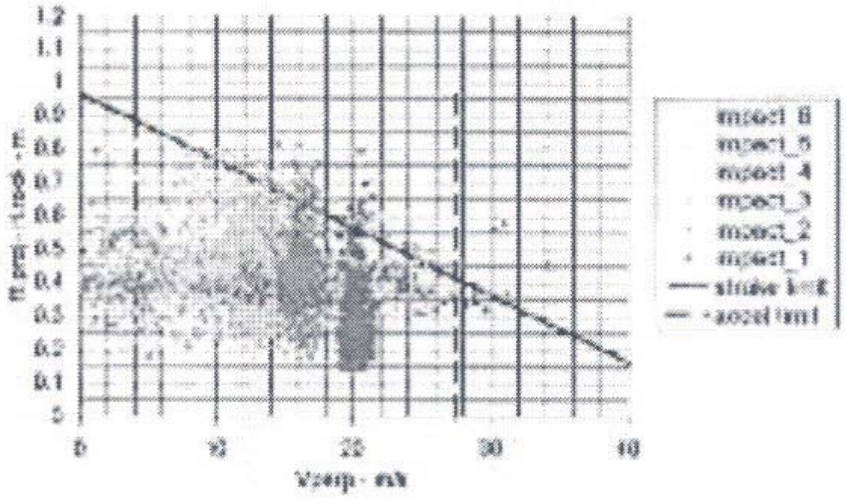

Figure 2-8: Responses based on Monte Carlo Distribution of Rock Sizes (with permission of authors; poor quality copy [2-7])

C. Bomb Bay Ejector Characteristics

Designers have built and tested airbag ejectors for bomb bays. In 1984, Howard King and Kilian Sneden of Northrop reported an experiment [2-15] with an airbag ejector for a CBU-20 Rockeye munition on a ground-test stand. Ejection velocities exceeded 13 ft/sec (set as an acceptable minimum for the test). Their airbag had 70 internal tethers per square inch to hold the outer surface in place after bomb ejection. Though they considered their experiments "highly successful", no further development was pursued.

In 2003, Vincent Vendetti of the US Naval Surface Warfare Center reported tests on a small bomb bay ejector airbag [2-16]. He concluded that more than 4,000 psig was necessary to eject a 90 lb submunition. He had airbag burst problems. Further work was canceled. See Figure 2-9 for a rendering of this system.

Figure 2-9: Naval Bomb Bay Ejector Airbag Test Apparatus (with permission of authors [2-16])

It is hypothesized that airbags can eject munitions successfully (>15 feet/second exit velocity) at far lower pressures – tens of psig, not thousands. This dissertation research strives to prove that low pressure airbags can eject munitions successfully. It is assumed that the rebound of a collidant from impact with an airbag is equivalent to an ejection. Hence an ejector with the same initial airbag volume, pressure, and air mass as an absorber airbag has when the collidant reaches a zero velocity, should produce the same ejection velocities.

D. Inflated Membrane Characteristics

The significant published work in inflated membranes concerns inflated fabric buildings.

1. Cylindrical Inflated Buildings

Civil Engineers Malcolm and Glockner [2-17] were called in by the Canadian government to study the collapses of air supported membrane buildings. It turned out

that snow and ice around the apex allowed for some ponding that ultimately caused collapse. The authors strove to define the relationship between shape, internal pressure, and critical loading of a pneumatic structure. They approached this challenge by examining the equilibrium of a central line load on a cylindrical inflatable in conjunction with ponding of rain or melt water. See Figure 2-10 below.

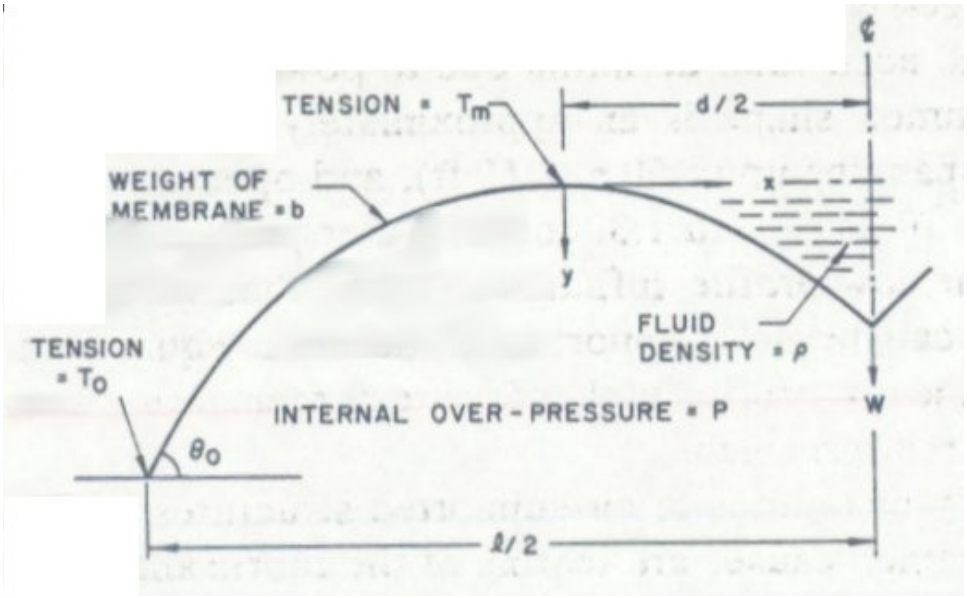

Figure 2-10: Deflected Shape with Central Load and Ponding (with permission of authors [2-17])

The equation they derived was not solvable analytically, so they solved it numerically using the Newton-Raphson technique. One of their intermediate relationships was an upper limit on the value of *W*, total ponding force, above which the membrane building collapsed

$$W \le 2\left(P - b\right)\sqrt{\frac{T_m}{\rho}} \tag{2-5}$$

where P is air pressure, b is fabric weight per unit area, T_m is membrane tension at the deformed apex, and ρ is density of material in the pond. Though this equation is not our hypothesis, it has some of the elements of our hypothesis. It has a static force (W), similar to our collidant dynamic force; fabric tension T_m, similar to our trampoline force; and airbag pressure P. The results of the numerical solution are presented in Figure 2-11 below.

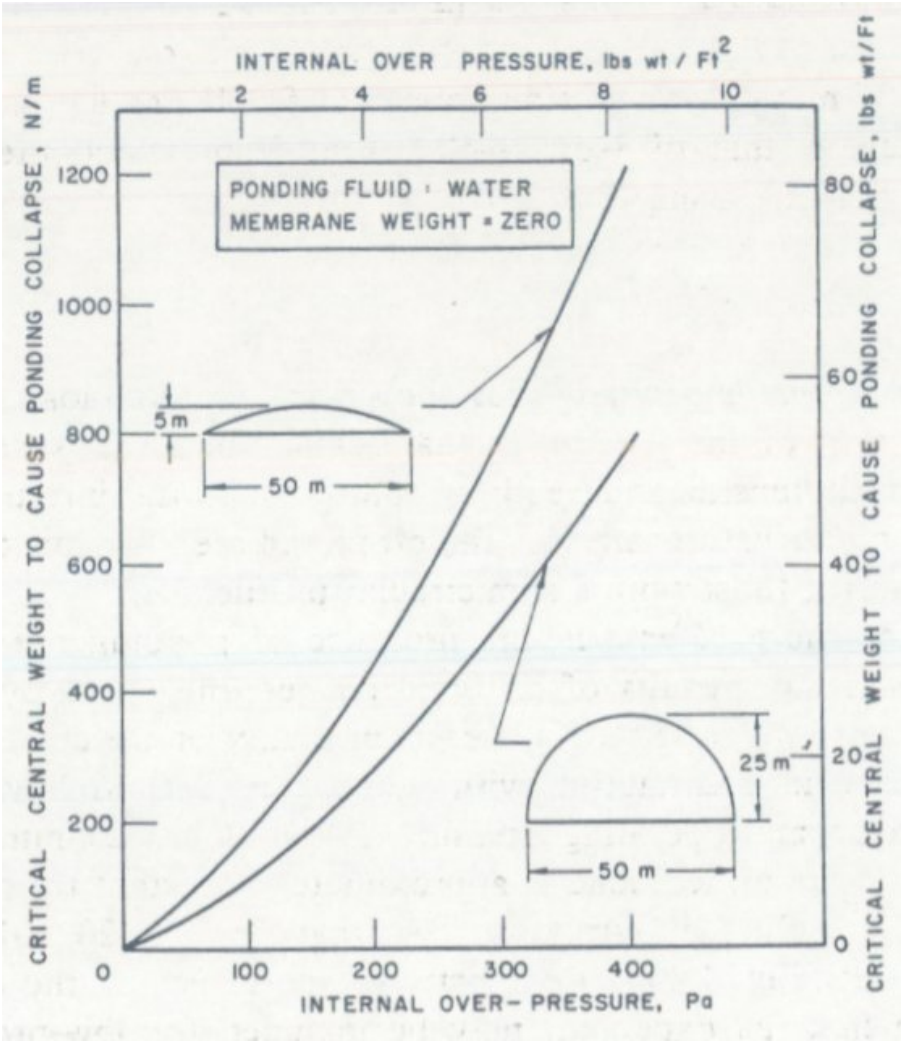

Figure 2-11: Effect of Internal Pressure and Shape on Critical Load (with permission of authors [2-17])

2. Hemispherical Inflated Buildings

Szyszkowski and Glockner [2-18] analyzed the behavior of hemispherical inflatable buildings under axi-symmetric concentrated loads. They found that the inflatable structures became unstable and exhibited snap-through buckling at certain aspect ratios. See Figure 2-12 below.

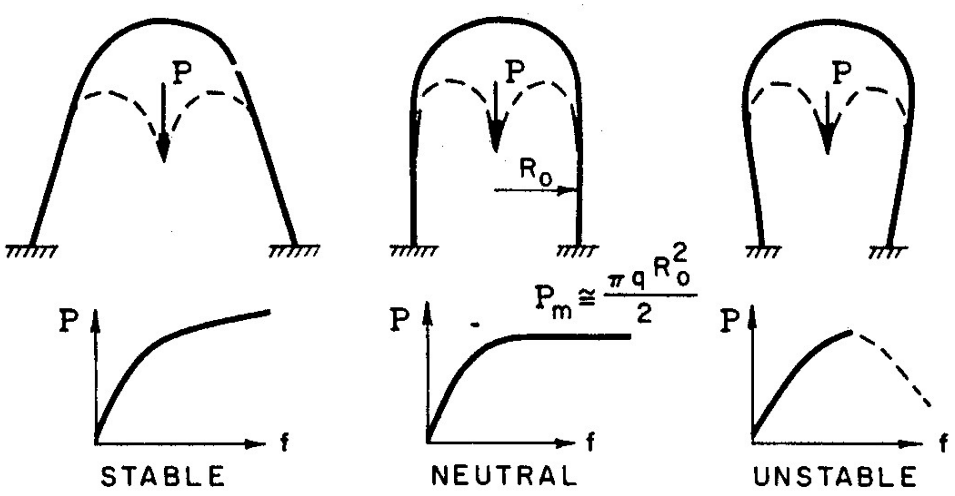

Figure 2-12: Qualitative load-deflection diagrams for spherical/cylindrical and spherical/conical membranes (with permission of authors [2-18])

The research of the present dissertation is limited to the central shape, which exhibits neutral stability. The equilibrium equation of Szyszkowski [2-18] is different from the dissertation's free body model for a center load. The authors conclude from their analysis that the maximum equilibrium concentrated load $P_{\max}$ is

$$P_{\max} = 0.968 \frac{\pi R_0^2 q_0}{2} \tag{2-6}$$

where R_0 is the initial radius of the inflated structure, and q_0 is the building air pressure. This maximum load occurs when the fabric adjacent to the concentrated load is 20^o from the vertical.

The authors' analysis goes on to show that the equilibrium concentrated load is zero when the adjacent fabric is 0^o from the vertical. The authors define the geometry and forces according to Figure 2-13 below. The concentrated downward central load on the spherical membrane is P. Internal pressure is q_0. The central downward deflection of the membrane is f.

The meridional normal angle φ, is the angle between the vertical and a line normal to the tangent of any point on the membrane surface. The meridional normal angle at the center point of the membrane is φ_0. It is defined as positive. It starts at zero in the unloaded case and increases to 90^o as the center point is deflected. The meridional normal angle at the outer point on the membrane where the membrane begins deflecting from its original shape, i.e., where the wrinkled region begins, is φ_1.

The horizontal radius from the central vertical axis to the point of interest on the membrane is r. The meridional radius of curvature of the undeformed spherical membrane is R_0. The deformed membrane meridional radius of curvature is R_φ. It varies from point to point on the membrane in the wrinkled region.

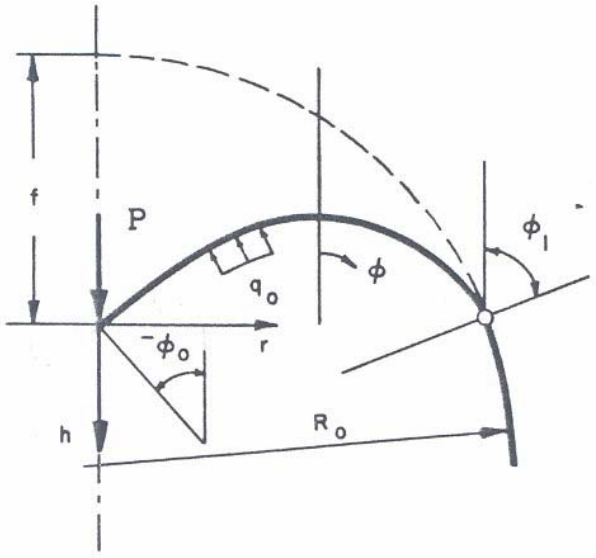

Figure 2-13: Deformed configuration of axisymmetric membrane (with permission of authors [2-18])

Using the boundary conditions, one obtains:

$$\sin\varphi_0 = \frac{P\sin\varphi_1}{\pi R_0^2 q_0 \sin^2\varphi_1 - P} \tag{2-7}$$

After transformations, the meridional normal angle φ_1 satisfies the equation:

$$\varphi_1 = \sqrt{\frac{P}{4\pi R_0^2 q_0 \sin\varphi_0}} \int_{-\varphi_0}^{\varphi_1} \frac{d\varphi}{\sqrt{\sin\varphi_0 + \sin\varphi}} \tag{2-8}$$

With numerical techniques, Equations (2-7) and (2-8) can be solved approximately. The results are shown in Figure 2-14. Note that, when the angles are zero, the force is zero, i.e., the undeformed case. As the force rises, the angles increase. These results allow for side ballooning of the membrane as φ_1 goes above 90^o.

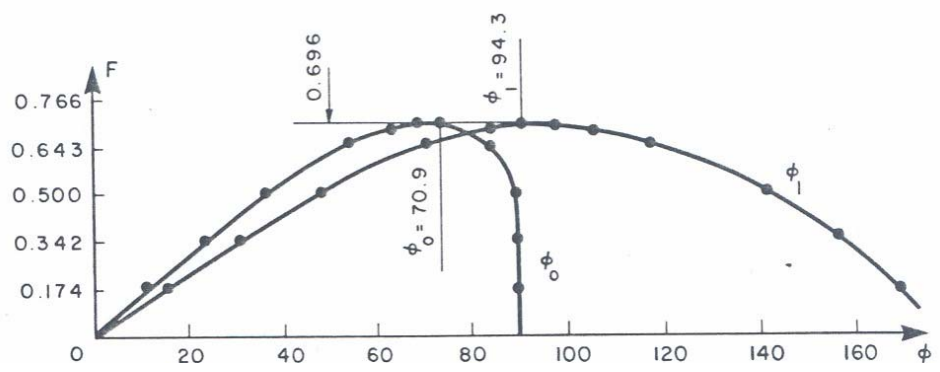

Figure 2-14: Plot of non-dimensional load F vs. fabric normal angle φ (with permission of authors [2-18])

Though the majority of the deceleration work done on our collidant occurs when the fabric next to the collidant is vertical, i.e. $\varphi_0 = 90^o$, an approximation is provided for the forces during the initial deflection of our airbag end cap.

The present dissertation assumes a constant radius for the airbag end cap dome arc forming in effect a partial torus versus the variable radius arc of Szyszkowski and Glockner [2-18]. The present dissertation assumes a simple free body model for the distributed force on the non-axisymmetric collidant versus the axisymmetric point load model of Szyszkowski and Glockner. Szyszkowski and Glockner model a static load versus the dynamic load of the present dissertation.

E. Nonlinear Airbag Code Validation Attempts

The state of the art in nonlinear airbag code validation is covered in references [2-19] through [2-31]. All these researchers used explicit nonlinear finite element code to numerically approximate airbag behavior. How these codes model airbag permeability or vent holes can affect the correlation of the simulations to experiments. For example,

LSDyna requires the user to specify a mass flow rate-pressure relationship for permeability modeling. These codes use conditions and trends from the previous time steps to predict the next time step conditions. Any inaccurate physics modeling or slight numerical drift from reality in early time steps often is magnified into large errors later in the simulation. As a result, when the simulations are compared to experimental results, the errors can be quite large, often hundreds of percent.

Nieboer [2-19] conducted nine impact tests on a single airbag, a standard 60 liter driver's side impermeable airbag with four 35 mm diameter vent holes. The airbags were fully inflated before impact. Each test had a single impactor traveling at a unique velocity ranging from 2.2 m/s to 5.9 m/s. The impactors were a 165 mm sphere and three circular plates of unique diameter. A typical collidant displacement error was the simulation showing a −50 mm displacement but the experiment showing a +12 mm displacement in an experiment where the peak displacement was 150 mm, resulting in a 48% error. The maximum collidant acceleration error was 174% in an experiment where the peak acceleration was −230 m/s^2. The airbag pressure error was 90 mbar in an experiment where the peak airbag pressure was only 180 mbar. These errors are on the order of 50% to 174%. The model used in [2-19] had only 3,456 elements and consumed only 300 CPU minutes, whereas the typical models used by Delphi have more than 200,000 elements and take more than a million cpu minutes to solve [2-33].

Lakshminarayan [2-29] conducted three impact tests on a single driver's side impermeable airbag with a single hemispherical impactor. The timing of impact was varied from uninflated, to partially inflated, to fully inflated. For the case of the uninflated airbag, the impactor was resting on the airbag when it was inflated, creating an

ejection response. For the other two cases, the impactor was moving toward the airbag when it was in the process of inflating and had reached a state of partial or full inflation. The simulation used PAM-CRASH, a leading airbag nonlinear dynamic software program. There were 600 quadrilateral elements. CPU time was not revealed, but the simulation was performed on the Ford Motor Company supercomputer, and the simulation results were closer to the experiment and less noisy than other references. The simulation over-predicted the peak collidant acceleration by 16%. The worst collidant velocity errors were 27% of the peak velocity. The worst airbag pressure errors were 14% of the airbag peak pressure. The lack of airbag permeability and venting removes a leading source of error in simulations and could explain why this simulation was the most accurate of all the references.

Matsumoto [2-30] conducted only a single experiment, a full scale vehicle crash with a 50 percentile male crash dummy and a driver's side airbag. The simulation software was MADYMO 2D. The number of model elements and CPU time were not revealed, but the simulation was performed on the Mazda Motor Corporation supercomputer. The worst simulation error was 38% of the peak collidant acceleration.

Hoffmann [2-31] used a production driver's side airbag, fully inflated on a rigid steering wheel, during a sled impact test with a Hybrid III crash dummy. The test was repeated three times. The simulation used PAM-CRASH. The number of model elements was 576 and CPU time on a Cray XMP was 1.5 minutes. The worst simulation error was 53% of the peak collidant acceleration.

Lu [2-32] tested two different driver's side vented airbags with slightly different diameters and vent hole sizes. A total of five tests were done against a swinging cylinder

impactor at various standoff distances. The number of model elements or CPU time was not revealed, but LS-Dyna was code used. LSDyna requires the user to define mass flow rate from vents and airbag permeability, generally as a function of a single state variable, such as pressure. The simulation over-predicted the peak collidant acceleration by 33%. The worst collidant velocity errors were 42% of the peak velocity.

F. Summary

The airbag is one of the lightest weight structural tools available to man, but one of the most difficult to model. The prior work on modeling and validating airbags is less extensive than the present dissertation. The Nefske model covered only a stationary collidant, required significant pre-testing to obtain geometry and state variable relationships, and used airbag leak rate as a factor to fit its simulation for limited experimental results. The Dreher model uses a distance step simulation model rather than the time step model of the present dissertation. The Dreher model did not account for the leak areas and volumes of the airbag end caps as the present dissertation does. The Szyszkowski and Glockner membrane model covers only stationary collidants, as well. The present dissertation assumes a constant radius for the airbag dome arc at a given azimuth, forming a partial torus, versus the variable radius arc of Szyszkowski and Glockner. The present dissertation assumes a distributed force on the simple free body model for the non-axisymmetric collidant versus the axisymmetric point load model of Szyszkowski and Glockner. Szyszkowski and Glockner model a static load versus the dynamic load of the present dissertation.

Prior work to validate nonlinear dynamic codes for airbags has shown simulation errors versus experiments ranging from 14% to 174%. Computation times last from several minutes to many hours for models with thousands of degrees of freedom and more. The most accurate model was of an unvented, impermeable airbag. Since permeability or venting are a major source of physics errors in the models, caution is advised in comparing it to the other references or the present dissertation which do model these features.

Chapter III: Airbag Collision Physics

A. Overview

The goal of this chapter is to develop differential equations that can be solved numerically for collidant acceleration $\ddot{z}$ and airbag pressure P. The model is specifically designed to analyze the experimental setup – a one-dimensional collision. The model assumes a one-dimensional collision and rebound of the collidant. Airbag geometry is assumed to depend explicitly upon only collidant position, z, and fabric strains ε_H and ε_L as described in Chapter 4.

Three systems were modeled: 1) a collidant dynamic system, 2) an airbag fabric dynamic system, and 3) a thermodynamic system consisting of a control volume inside the airbag. The collidant and fabric dynamic systems are divided into three free bodies for force equilibrium as shown in Figure 3-1.

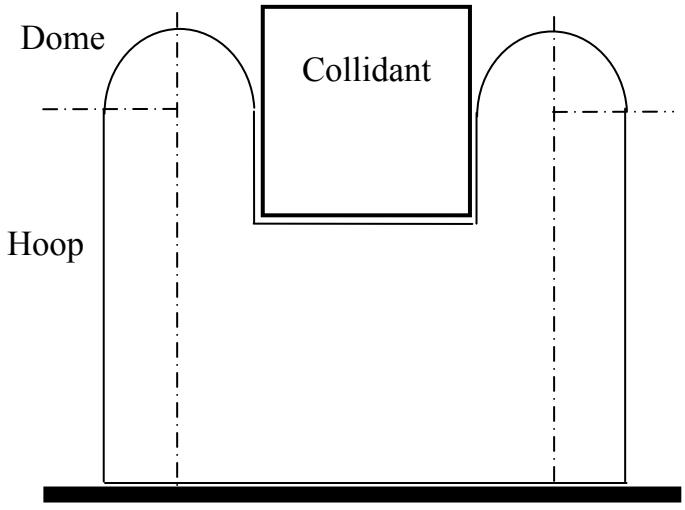

Figure 3-1: Hoop, Dome, and Collidant Free Body Segmentation

The control volume inside the airbag system is modeled as an open thermodynamic system as shown in Figure 3-2.

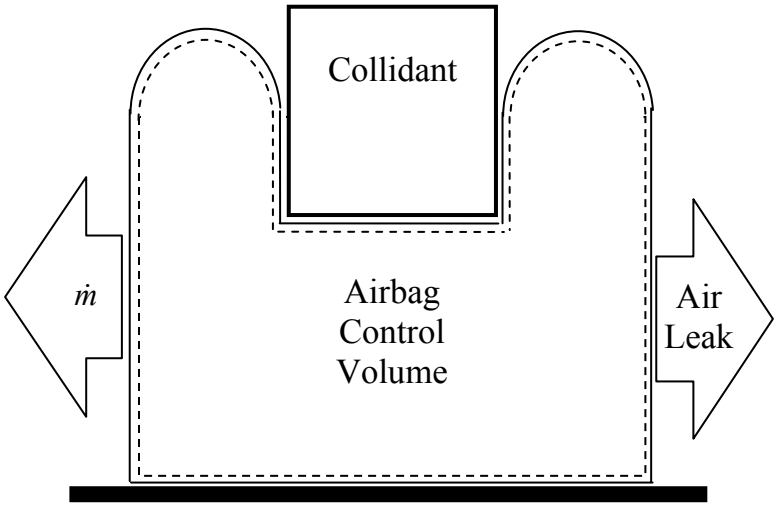

Figure 3-2: Open Thermodynamic System of Air inside Airbag

B. Governing Equations Applied to the Systems

Three physical relationships of thermodynamic systems provide some equations to solve for these unknowns: 1) Conservation of Mass, 2) Conservation of Momentum or Newton's second law, and 3) Conservation of Energy. These equations are

$$\frac{Dm}{Dt} = 0 \tag{3-1}$$

$$\frac{D\left(m\dot{z}\right)}{Dt} = \Sigma F \tag{3-2}$$

$$\frac{DE}{Dt} = \delta\dot{Q} - \delta\dot{W} \tag{3-3}$$

1. Conservation of Mass Equations.

The conservation of mass equation (3-1) applies to all three systems. The dynamic systems have no change in mass; hence, the trivial solution applies. The control volume system does have air mass crossing its boundary. The conservation of air mass says that the change in control volume mass is equal to the inflow minus the outflow, where $\dot{m}$ is flow into the airbag. Hence positive $\dot{m}$ raises control volume air mass m, and negative $\dot{m}$ decreases the control volume air mass.

$$\frac{\partial}{\partial t}\iiint_{CV} \rho dV = \dot{m} = -\iint_{pores} \rho \vec{u}_p \cdot d\vec{A}_p \tag{3-4}$$

where $m = \rho V$ and A_p is the area of the pores. The air in the airbag leaks out through the pores in the fabric at velocity u_p relative to the control surface when the airbag is pressurized. Mass continuity can be used to solve for pore entrance velocity.

$$u_p = \frac{\dot{m}}{\rho A_p} \tag{3-5}$$

The air density at the pore ρ_p is assumed to be the same as the bulk air density in the control volume ρ.

2. Conservation of Momentum Equations.

The conservation of momentum equation (3-2) applies to all three systems.

a. Collidant Dynamic System: The collidant dynamic system has significant change in momentum in the vertical axis but insignificant change in the other axes. Hence the model assumes a one-dimensional system. The free body diagram in Figure 3-3 shows the force equilibrium for the collidant.

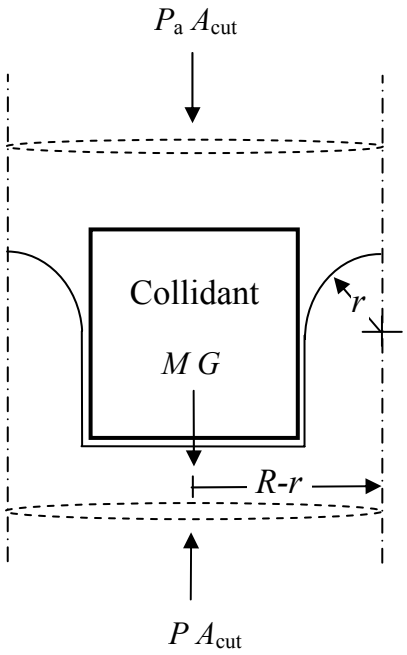

Figure 3-3: Free Body Diagram Collidant Dynamic System

The vertical cut was made to avoid fabric forces contributing to vertical accelerations in this free body diagram. The weight of the collidant and atmospheric pressure act downward, while the airbag pressure acts upward. The pressure forces net to the gage pressure (P_g) in the airbag, acting on the horizontal cut area of the airbag, A_{cut}. This area consists of the collidant face area plus the projection of the inner hemispherical dome onto the horizontal plane.

$$A_{cut} = \frac{1}{2}\int_0^{2\pi} \left(R - r\right)^2 d\phi \tag{3-6}$$

where hemispherical dome radius $r(\phi)$ varies with azimuth angle ϕ as described in Chapter 4.

The collidant moves in a straight vertical line perfectly centered on the top center of the airbag. Gravity (G) drives it from various drop heights to impact the airbag at various speeds. Therefore, the motion of the collidant momentum acts in only one direction – straight up and down – designated as the z direction with its origin on the ground and positive in the upward direction. The force balance of Newton's Second Law

$$M(\ddot{z} + G) = P_g A_{cut} \tag{3-7}$$

is rearranged to isolate the acceleration.

$$\ddot{z} = \frac{P_g A_{cut}}{M} - G \tag{3-8}$$

b. Airbag Fabric Dynamic System: The airbag fabric dynamic system sustains significant force through its hoop stress and longitudinal stress, but insignificant change in momentum in terms of its light fabric mass. The airbag fabric has a mass of less than 1/16 of a slug and accelerates on average less than 5 feet/second^2, based on empirical results in Chapter 6, hence causing a change in momentum of less than a third of a pound. The airbag fabric dynamic system is modeled by force equilibrium as shown by the two free body diagrams in Figure 3-4.

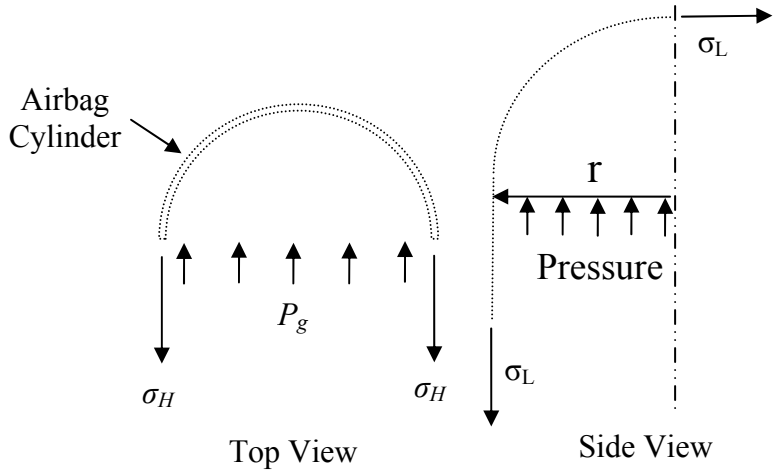

Figure 3-4: Free Body Diagrams of Airbag Fabric in Hoop and Longitudinal Tension

Hoop stress is obtained from quasi-static force equilibrium in the lateral direction. The hoop radius R is a function of hoop strain. Most of the airbag hoop strain energy comes from the strain in the airbag cylinder and little from strain in the airbag dome. If the airbag were impermeable, the airbag gage pressure would act over the entire fabric surface. Based on the free body diagram force balance, the hoop stress in the cylinder would be

$$\sigma_H t = P_g R \tag{3-9}$$

$$\sigma_H = \frac{P_g R}{t} = P_g A_H = \frac{P_g R_0 \left(1+\varepsilon_H\right)}{t} \tag{3-10}$$

where hoop area factor $A_{\mathrm{H}} = R/t$.

Because the airbag fabric is permeable, the gage pressure acts on the fabric fibers and a Fanno force acts on the fabric pores as shown in Figure 3-5. The cylinder hoop stress contains the gage pressure times fiber area, which is assumed constant with varying hoop stress. All the hoop strain is assumed to open up

pores, hence the Fanno flow resistance force R_x grows with strain and hence stress. The equation for R_x is shown in Appendix A. The difference between incorporating Fanno flow or not is shown to be negligible in the simulation in Chapter 7. Figure 3-4 shows the gauge pressure acting on the fibers and on the pores, which is the assumption made for both hoop stress and longitudinal stress, discussed next.

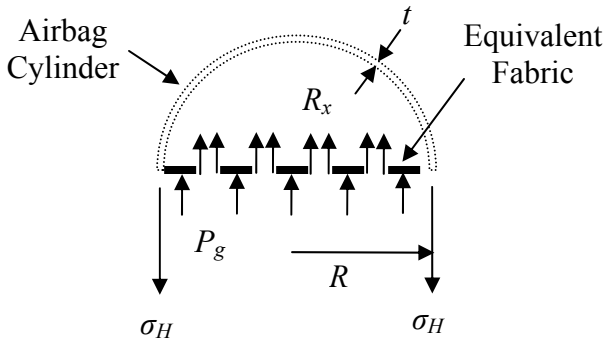

Figure 3-5: Pressure and Fanno Force on Equivalent Fabric

The longitudinal stress in the airbag cylinder can be calculated from the airbag pressure acting on the dome radius, per the free body diagram in Figure 3-4. The longitudinal stress is derived from a force balance of the free body diagram.

$$\sigma_L t R\phi = P_g r\left(R - \frac{r}{2}\right)\phi \tag{3-11}$$

$$\sigma_L = \frac{P_g}{t}\left(r - \frac{r^2}{2R}\right) = P_g A_{Long} \tag{3-12}$$

where A_{Long} is a geometry factor delineated in Chapter 4. The dome radius r varies with azimuth angle φ, collidant height z, hoop stress σ_{H}, and longitudinal stress σ_{L} itself.

Although different kinematic equations govern dome radius in different impact phases, Equation (3-12) applies in every phase. Thus Figure 3-4 is generic to all phases. Uniform stress is assumed for the model with the option of it varying with azimuth angle ϕ through dome radius $r(\phi)$ in the future.

c. Control Volume Thermodynamic System: The air in the airbag thermodynamic system has a small conservation of momentum. Most of the air in the airbag is assumed quiescent, except for the isentropic streamlines leading to the pores. Because the radial flows are equal and opposite to each other, their momentum changes cancel each other out. Only the flows out the top of the airbag have a net change in momentum. The amount of air mass in these top flows is approximately 1/1500 slug with a peak velocity change of approximately 100 feet/second (based on simulation results from Chapter 7) which would require a force of approximately 1/15 of a pound. Thus, the momentum of the air leaving the control volume was negligible in the analysis of the airbag pressure and collidant acceleration. Appendix A shows how to incorporate it using a second control volume for the air flowing through the pores. Ignoring elevation differences, the Bernoulli equation for this streamline flow becomes

$$P_p = P - \rho \frac{u_p^2}{2} \tag{3-13}$$

1) Conservation of Energy Equations: The conservation of energy equation (3-3) applies to all three systems. All systems are assumed adiabatic, $\delta \dot{Q} = 0$. The control volume has a ~65 ^{o}F peak temperature rise during the impact, but insufficient time for significant heat transfer as explained in Section D. The collidant and fabric dynamic systems have no temperature rise other than negligible heat transfer from the air

in the airbag. The energy equations for the dynamic systems of the collidant and fabric are analyzed in Appendix A. Those equations proved superfluous once the fabric-mass system of Figure 3-1 was divided into three free-body diagrams and quasi-static equilibrium was assumed for the fabric system.

The components of the conservation of energy equation for an open system are described next. The major energy of the system is the internal energy of the air inside the airbag, kinetic and potential energies being negligible. The event is so fast as to be adiabatic to heat conduction or radiation. The thermodynamic system has significant change in energy. The E on the left hand side of Equation (3-3) includes total energy in the control volume, as well as energy transported across the boundary. The rate of work on the boundary $\delta\dot{W}$ is the absolute pressure inside the control volume acting on the moving fiber area and the absolute pore pressure P_{p} times the gas velocity through the pore, multiplied by the appropriate cross sectional pore area. Because the control surface is inboard of the fabric and fabric pores, only two types of work are done on the boundary of the system:

1) the absolute pressure P of the system acting on the moving boundary;
2) the absolute pressure P_p pushing the volume of air through the pores.

These work pressures are absolute pressures, because they are opposed by equal and opposite pressures from the fabric and pore openings, respectively. Therefore the external work uses these absolute pressures. The friction work of the air moving through the pores is outside the control surface but accounted for by the absolute pressure pushing the air through the pores. Positive pressure and positive outward flow and area vectors mean that the boundary work takes energy from the system; therefore, it is negative on

the left hand side of Equation (3-14). Likewise for the flow work through the pores, positive outward normal vectors take energy from the system. The major energy crossing the boundary of the system is the specific energy e_p of the air leaking through the pores of the airbag. Hence the conservation of energy equation for this open system is

$$-\iint_{fibers} P\vec{u}_b \cdot d\vec{A}_m - \iint_{pores} P_p\vec{u}_p \cdot d\vec{A}_p = \frac{\partial}{\partial t}\iiint_{CV} e\rho dV + \iint_{pores} e_p\rho\vec{u}_p \cdot d\vec{A}_p \qquad (3\text{-}14)$$

The conservation equations have introduced eight equations to solve for the following fifteen unknown variables:

m = mass of air inside airbag

P = absolute pressure inside airbag

u_b = velocity of boundary of control volume

ρ = density of air in airbag = m/V

e = specific energy of air in control volume

V = volume of air inside airbag control volume

z = elevation of the collidant bottom

ε_H = horizontal hoop strain of airbag

σ_H = horizontal hoop stress of airbag

ε_L = longitudinal strain of airbag

σ_L = longitudinal stress of airbag

u_p = velocity of air into the airbag pore

P_p = pore entrance air pressure

A_m = moving outward normal area of airbag excluding leaking pore area $= A_{Lf} + A_{face}$

A_p = cross sectional area of pores in the leak area

e_p = specific energy of air entering the pores in the control surface

The following geometric quantities needed in this chapter can be calculated from the kinematic equations derived in Chapter 4.

A_{cut} = cross sectional area of a horizontal cut of airbag for free body analysis

A_{Lf} = airbag fiber outward surface area where air can leak through the pores

A_{p0} = outward normal area density of pores in unstrained airbag fabric

C. Closure Equations

The following constitutive equations are needed to close the system of equations derived from the conservation laws in the previous Section B.

1. Constitutive Equations.

Air pressure P, temperature T, and density ρ inside the airbag are considered uniform except approaching the pores. Approaching the pores, air density remains constant, but pressure and temperature drop due to the higher velocity. The relevant constitutive equation is the Ideal Gas Law.

$$P = \rho RT \tag{3-15}$$

Where the airbag contacts the ground or the collidant, the pressure is assumed to seal the fabric against these surfaces, preventing air from leaking out of the pores of the airbag. Therefore, the mass flow below is based on a non-linear function of gage pressure, depending on three parameters, $\dot{m}_{A0}$ (or $\dot{m}_0$), α, and R_L. The three parameters were found by non-linear least squares regression of Equation (5-10) to the permeability

experimental data as a function of gage pressure. This mass flow was empirically determined in Chapter 5, and is

$$-\dot{m} = A_{Lf}\left[R_L P_g + \dot{m}_{A0}\left(1 - e^{-\alpha P_g}\right)\right] \tag{3-16}$$

where $\dot{m}_{A0} = \dot{m}_0 / A_{Lf}$, $\dot{m}$, the air mass flow rate into the airbag, $P_g = P - P_{atm}$ is gage pressure, and R_L, the leak rate through the airbag. Equation (3-4) expresses mass flow rate as a non-linear function of gage pressure, depending on three parameters, $\dot{m}_{A0}$ (or $\dot{m}_0$), α, and R_L. Equation (3-4) constitutes a constitutive equation for mass flow rate, relating it to pressure.

The hoop stress and strain are assumed to be uniform throughout the airbag. In reality, the hoop stress is lower in the dome than the cylinder, but this variation is neglected. The longitudinal stress and strain are also assumed to be longitudinally uniform even though the stress in the dome is higher. Longitudinal stress and strain do vary with azimuth angle. The relevant constitutive equations for plane stress are

$$\begin{Bmatrix} \varepsilon_H \\ \varepsilon_L \\ \gamma_{HL} \end{Bmatrix} = \begin{bmatrix} [C] & & 0 \\ & & 0 \\ 0 & 0 & \dfrac{1}{G} \end{bmatrix} \begin{Bmatrix} \sigma_H \\ \sigma_L \\ \tau_{HL} \end{Bmatrix}, \quad \text{where } [C] = \begin{bmatrix} \dfrac{1}{E_H} & \dfrac{-\nu_L}{E_L} \\ \dfrac{-\nu_H}{E_H} & \dfrac{1}{E_L} \end{bmatrix} \tag{3-17}$$

2. Microscopic Examination and Strain of Pore Area.

Microscopic investigation found the unstrained pore area density A_{p0} to be ~0.1% of the unstrained fabric outward surface area. Under strain, the pores grow disproportionately to the fibers. In effect, all the additional bulk fabric area created by the strain goes to the pores. Hence, the leaking pore area is

$$A_p = A_L(A_{p0} + \varepsilon_H + \varepsilon_L) \tag{3-18}$$

This pore area is used to calculate pore velocity, the work of gas blowing through the pores, and the pore shear force and work as well in Appendix A. Therefore, the pore area must be unobstructed.

3. Air State at Pore.

The state at the pore entrance is determined by five equations 1) air mass continuity Equation (3-5), 2) Bernoulli free stream flow Equation (3-13), 3) the Ideal Gas Law, 4) the definition of Mach number, and 5) the definition of specific energy. Since the air flow rates inside the control volume are fairly low, incompressible flow along a streamline is a reasonable assumption. Hence the density at the pore entrance is assumed equal to the bulk air density of the control volume. The Ideal Gas Law determines the pore entrance temperature.

$$T_p = \frac{P_p}{\rho R} \tag{3-19}$$

Pore entrance Mach number is a function of the Ideal Gas constant, pore entrance velocity and temperature.

$$M_p = \frac{u_p}{\sqrt{\gamma R T_p}} = \frac{u_p}{\sqrt{\gamma \frac{P_p}{\rho}}} \tag{3-20}$$

Since these gas flows have negligible change in elevation and hence potential energy, the specific energy e_p of the air at the pore entrance is the air specific enthalpy plus specific kinetic energy. Hence

$$e_p = c_p T_p + \frac{u_p^2}{2} \tag{3-21}$$

The specific heat at constant volume c_v is a measured property in a constitutive relationship and is the specific heat minus the Ideal gas Constant.

$$c_v = c_p - R \tag{3-22}$$

4. Closure of the Open Thermodynamic System of the Air in the Airbag.

An open thermodynamic system of the air inside the airbag was chosen for the physical model. The system includes only the air inside the airbag and is open, because it allows air mass transport across its boundary. Figure 3-2 shows this thermodynamic system with the dashed lines as its boundary. The system contains the thermal or internal energy $U = c_v T$ of the air inside the airbag. Because the specific energy of the control volume is quiescent, it is merely internal energy. Its derivative with time is shown as the first two terms on the right hand side of Equation (3-23). Since the airbag air weighs less than 2 lbs, its gravitational potential and kinetic energies are ignored.

Only air mass and its associated energy cross the boundary of the open thermodynamic system. The impact is so quick that there is essentially no time for heat transfer. Air does leak out through the pores of the airbag, causing a significant mass transport $\dot{m}$ across the boundary of the system with attendant energy transport. The friction work of the viscous air moving through the pores of the airbag limits the air flow through the pores. This friction was accounted for by the mass flow constitutive relationship Equation (3-12). The work of airbag gage pressure on the moving airbag causes boundary work.

The moving boundary work is the pressure force on the boundary acting through the distance the boundary moved. This boundary area times the distance it moves is a

volume, in fact, the volume displaced by the boundary moving. Since pressure inside the control volume is assumed to be uniform, pressure multiplied by this change in volume is the moving boundary work; hence Equation (3-14) simplifies to

$$-P\dot{V}\frac{A_m}{A_m+A_p}+P_p v\dot{m}=\dot{m}c_vT+mc_v\dot{T}-\dot{m}\left(c_vT_p+\frac{u_p^2}{2}\right) \tag{3-23}$$

where $v = 1/\rho$ is specific volume and T is absolute temperature of air in airbag. Rearranging terms in Equation (3-23) allows putting the pore work Pv together with its internal energy, making an enthalpy on the right hand side.

$$-P\dot{V}\frac{A_m}{A_m+A_p}=\dot{m}c_vT+mc_v\dot{T}-\dot{m}\left(c_pT_p+\frac{u_p^2}{2}\right) \tag{3-24}$$

Rearranging variables allows a solution for $\dot{T}$

$$\dot{T}=\frac{-\dot{m}c_vT+\dot{m}\left(c_pT_p+\frac{u_p^2}{2}\right)-P\dot{V}\frac{A_f}{A}}{mc_v} \tag{3-25}$$

a. Ideal Gas Law for Airbag Temperature *T* and its Time Derivative.

The Ideal Gas Law determines the control volume bulk temperature. Rearranging Equation (3-11) and substituting the definition of density yields an equation for temperature

$$T=\frac{PV}{mR} \tag{3-26}$$

The time derivative is simply

$$\dot{T}=\frac{\dot{P}V+P\dot{V}}{mR}-\frac{\dot{m}RPV}{(mR)^2} \tag{3-27}$$

Substituting into Equation (3-25) eliminates $\dot{T}$.

$$\frac{\dot{P}V + P\dot{V}}{mR} - \frac{\dot{m}RPV}{(mR)^2} = \frac{-\dot{m}c_v T + \dot{m}\left(c_p T_p + \frac{u_p^2}{2}\right) - P\dot{V}\frac{A_m}{A_m + A_p}}{mc_v} \tag{3-28}$$

Both sides of Equation (3-28) are multiplied by the air mass *m* to remove its redundancy. The rate of change in volume $\dot{V}$ is a function of collidant velocity, hoop strain rate, and longitudinal strain rate. Hoop strain rate is a function of pressure change $\dot{P}$. To bring all the $\dot{P}$ terms to the left side, the $\dot{V}$ terms are regrouped.

$$\frac{\dot{P}V}{R} + P\dot{V}\left(\frac{1}{R} + \frac{1}{c_v}\frac{A_m}{A_m + A_p}\right) = -\dot{m}T + \frac{\dot{m}\left(c_p T_p + \frac{u_p^2}{2}\right)}{c_v} + \frac{\dot{m}PV}{mR} \tag{3-29}$$

Substituting the Ideal Gas Law for *T*, multiplying by gas constant *R*, and substituting the definitions of $c_p = R + c_v$ and $\gamma = c_p / c_v$ yields

$$\dot{P}V + P\dot{V}\left(1 + (\gamma - 1)\frac{A_m}{A_m + A_p}\right) = \dot{m}(\gamma - 1)\left(c_p T_p + \frac{u_p^2}{2}\right) \tag{3-30}$$

Substituting γ_f for the expression in parenthesis on the left hand side of the equality and using the Ideal Gas Law to eliminate the temperatures yields

$$\dot{P}V + P\gamma_f \dot{V} = \dot{m}\left(\gamma\frac{P_p}{\rho} + (\gamma - 1)\frac{u_p^2}{2}\right) \tag{3-31}$$

where

$$\gamma_f = \left(1 + (\gamma - 1)\frac{A_m}{A_m + A_p}\right) \tag{3-32}$$

Substituting in the Bernoulli Equation (3-13) allows the elimination of additional terms.

$$\dot{P}V + P\gamma_f \dot{V} = \dot{m}\left(\gamma \frac{P}{\rho} - \frac{u_p^2}{2}\right) \tag{3-33}$$

As shown in Chapter 4, volume depends on the kinematic state variables z, ε_H, and ε_L. Hence, the equation for $\dot{V}$ depends on the partial derivatives of V with respect to z, ε_H, and ε_L and their time rates of change, respectively, as shown in Equation (3-33).

b. Combined with Equilibrium Form of Longitudinal Stress

For the case where σ_L is derived from force equilibrium in the fabric, $\dot{V}$ is derived as

$$\dot{V} = V_{,z}\,\dot{z} + V_{,\varepsilon_H}\,\dot{\varepsilon}_H + V_{,\varepsilon_L}\,\dot{\varepsilon}_L = V_{,z}\,\dot{z} + \left\{V_{,\varepsilon}\right\}^T \begin{Bmatrix} \dot{\varepsilon}_H \\ \dot{\varepsilon}_L \end{Bmatrix} \tag{3-34}$$

The volume derivative can be found from the strain derivatives, which, in turn, depend on the stress derivatives. The stresses found in Equations (3-19) and (3-20) can expressed more broadly as a function of gage pressure P_g and so-called geometry factors, A_H and A_{Long}.

$$\begin{aligned} \sigma_H &= P_g A_H\left(z, \varepsilon_H, \varepsilon_L\right) \\ \sigma_L &= P_g A_{Long}\left(z, \varepsilon_H, \varepsilon_L\right) \end{aligned} \tag{3-35}$$

Simultaneous Equations (3-35) are coupled to the strains, through constitutive Equation (3-3), which determine the geometry factors. In keeping with the simplifying assumption of uniform stress and strain, Equations (3-35) can be solved in conjunction with an equivalent circular collidant (i.e., cylindrical collidant with radius that gives same face area as the rectangular collidant). The resulting uniform strains are used to determine the geometry factors in Chapter 4 whose partial derivatives appear in the following differentiation with respect to time. In vector form, Equation (3-35) may be written as

$$\begin{Bmatrix} \sigma_H \\ \sigma_L \end{Bmatrix} = P_g \begin{Bmatrix} A_H \\ A_{Long} \end{Bmatrix} \tag{3-36}$$

The strains can be found using the constitutive matrix.

$$\begin{Bmatrix} \varepsilon_H \\ \varepsilon_L \end{Bmatrix} = [C] \begin{Bmatrix} \sigma_H \\ \sigma_L \end{Bmatrix} = [C] P_g \begin{Bmatrix} A_H \\ A_{Long} \end{Bmatrix} \tag{3-37}$$

Time differentiation yields

$$\begin{Bmatrix} \dot{\varepsilon}_H \\ \dot{\varepsilon}_L \end{Bmatrix} = [C] \begin{Bmatrix} A_H \\ A_{Long} \end{Bmatrix} \dot{P} + [C] P_g \begin{Bmatrix} \dot{A}_H \\ \dot{A}_{Long} \end{Bmatrix} \tag{3-38}$$

$\dot{P}$ emerges, but the geometry derivatives depend on the strain derivatives.

$$\begin{Bmatrix} \dot{A}_H \\ \dot{A}_{Long} \end{Bmatrix} = \begin{Bmatrix} A_{H,z} \\ A_{Long,z} \end{Bmatrix} \dot{z} + \begin{bmatrix} A_{H,\varepsilon_H} & A_{H,\varepsilon_L} \\ A_{Long,\varepsilon_H} & A_{Long,\varepsilon_L} \end{bmatrix} \begin{Bmatrix} \dot{\varepsilon}_H \\ \dot{\varepsilon}_L \end{Bmatrix} \tag{3-39}$$

Substituting and separating yields

$$\begin{Bmatrix} \dot{\varepsilon}_H \\ \dot{\varepsilon}_L \end{Bmatrix} = \left[[I] - P_g [C][\partial A] \right]^{-1} [C] \left(\begin{Bmatrix} A_H \\ A_{Long} \end{Bmatrix} \dot{P} + P_g \dot{z} \begin{Bmatrix} A_{H,z} \\ A_{Long,z} \end{Bmatrix} \right) \tag{3-40}$$

where

$$[\partial A] = \begin{bmatrix} A_{H,\varepsilon_H} & A_{H,\varepsilon_L} \\ A_{Long,\varepsilon_H} & A_{Long,\varepsilon_L} \end{bmatrix} \tag{3-41}$$

Substituting back into Equation (3-34) yields

$$\dot{V} = V_{,z} \dot{z} + \{V_{,\varepsilon}\}^T \left[[I] - P_g [C][\partial A] \right]^{-1} [C] \left(\begin{Bmatrix} A_H \\ A_{Long} \end{Bmatrix} \dot{P} + P_g \dot{z} \begin{Bmatrix} A_{H,z} \\ A_{Long,z} \end{Bmatrix} \right) \tag{3-42}$$

If $\dot{V}$ is broken into coefficients of $\dot{z}$ and $\dot{P}$, the result is described as

$$\begin{aligned} V_{,Z} &= V_{,z} + \{V_{,\varepsilon}\}^T \{\varepsilon_{,z}\} \\ V_{,P} &= \{V_{,\varepsilon}\}^T \{\varepsilon_{,P}\} \end{aligned} \tag{3-43}$$

where

$$\{\varepsilon_{,z}\} = \left[[I] - P_g[C][\partial A]\right]^{-1}[C]P_g \begin{Bmatrix} A_{H,z} \\ A_{Long,z} \end{Bmatrix}$$
$$\{\varepsilon_{,P}\} = \left[[I] - P_g[C][\partial A]\right]^{-1}[C] \begin{Bmatrix} A_H \\ A_{Long} \end{Bmatrix} \quad (3\text{-}44)$$

Equations (3-42) through (3-44) can be substituted back into Equation (3-32) to express $\dot{P}$ for the case of longitudinal stress derived from equilibrium. What remains to be solved are the partial derivatives of A_{H} and A_{Long} with respect to z, ε_{H}, and ε_{L}. These derivatives are calculated in Chapter 4 Section D. 2.

D. Assumptions and Justifications

Several important assumptions were made to simplify the problem.

1. The dynamic motion of the collidant was assumed to be one-dimensional in the vertical, z axis.
2. The momentum of the air inside the airbag and airbag fabric were considered negligible compared to the collidant's momentum.
3. A prescribed geometry was assumed to govern the shape of the airbag (see Chapter 4). As a result, volume and surface areas of the airbag were considered functions of collidant position and airbag strain, only.
4. A state of uniform stress was assumed throughout the airbag fabric.
5. A uniform (mean) state was assumed for the air inside the airbag, except for quasi-steady, isentropic streamlines leading to air mass flow through the pores in the airbag fabric.

6. The collidant impact was assumed to be of such short duration that the system was adiabatic.
7. The fabric area under the collidant is assumed strained because of the relatively frictionless contact with the collidant.

The first assumption is justified in that the collidant gondola is restrained by ¾ inch steel guide cables tensioned to approximately 1,000 lbs each. Video records of motion of the gondola in a typical experiment show lateral displacements of 0.3 % of the gondola vertical displacements, lateral velocities of less than 0.3% of the vertical velocities, and lateral kinetic energies of less than 0.1% of the vertical kinetic energies. Ignoring lateral motion is justified on its relatively small size compared to the 15 to 34 foot vertical drop. It would account for some small kinetic energy transfer.

The second assumption is justified in that the air mass and fabric mass are less than 1% of the collidant mass. Though most of the air and fabric mass is relatively stationary, at least part of it moves at close to the speed of the gondola. Hence the air and fabric momentum is less than 1% of the momentum of the typical gondola. Ignoring the air and fabric momentum is justified on its small size relative to the 350 to 600 lb gondolas. It would absorb some small kinetic energy, however. The neglected air is inside the airbag. The air blowing out the pores is outside the system as later defined, and therefore its potentially high momentum would not be considered in the second assumption.

Assumption three is justified in that the prescribed geometry closely resembles the actual airbag volume and surface area – the two key factors in determining dynamic response of collidants. The major differences in the geometry assumptions are a hemispherical dome instead of a more realistic flattened dome and a straight cylinder

airbag bottom instead of a domed bottom. The first difference adds volume and surface area; the second, subtracts volume and surface area.

Assumption four is justified in that the most important factors determining dynamic response, airbag volume and surface area, are integrated values based on integrated strains. These integrated strains can be based on integrated stresses, hence average stresses can capture nearly as accurately as variegated stresses the global effect on collidant kinematics. Moreover, equations derived in this chapter will show that hoop stress depends uniformly on the integrated effect of strain, whereas longitudinal stress varies with azimuth position. Hence uniform hoop strain is better justified than longitudinal strain. However, Chapter 7 will show that longitudinal strain is an order of magnitude less than hoop strain, leading to small errors due to assuming uniform strain.

Assumption five is justified in that the secondary air flows inside the airbag caused by fill jets, for example, that would justify varying the state variable values, are small enough to be ignored. These fill jets are turned off before impact. Any residual swirl is substantially dissipated by the air transport toward and through the pores. As shown in Chapter 7, the air transport through the pores is a small fraction of the total air in the airbag, and hence its non-uniformity is ignored as well.

Assumption six is justified in that the impact duration is less than 0.2 seconds and the amount of energy lost through heat transfer is less than 1% of the collision energy. Heat transfer is based on the temperature difference between the air inside the airbag and the air outside the airbag. The air temperature outside the airbag is typically $T_1 = 70^oF$ or 530^oR. During adiabatic compression, the absolute temperature ratio in degrees Rankine

is proportional to the absolute pressure ratio as explained in Saad [3-1:16]. A typical airbag pressure ratio to atmosphere in the experiments is 1.5 to 1. Hence:

$$T_2 / T_1 = (P_2/P_1)^{(\gamma-1)/\gamma} = 1.5^{0.286} = 1.12$$

The resulting temperature in the airbag at peak compression is $T_2 = 1.12 \times 530^{o}R = 595^{o}R = 135^{o}F$. The heat transferred to the air outside the airbag, Q, is based on the temperature difference, $T_2 - T_1 = 65^{o}F$, a heat transfer coefficient h, and an airbag surface area A, as explained in Rohsenow [3-2:92]. For the case of a typical single-walled bumper airbag, the heat transfer is about 0.5 Btu/hr-sqft-F, and the airbag surface area is about 41 square feet. The equation is:

$$Q = hA\ \Delta T = 0.5 * 41 * 65 = 1{,}336 \text{ Btu/hour} = 0.37 \text{ Btu/sec}$$

Typical collision compression only lasts about 1/5 second, so the heat transferred is only about 0.07 Btu. The temperature change of the air inside the airbag is proportional to this heat addition and the mass of the air m =3.4 lbm, and the heat capacity of the air $c_p = 0.24$ Btu/lbm, [3-5: 522]. Therefore:

$$\Delta T = Q / (m\ c_p) = 0.07 / (3.4 * 0.24) = 0.09^{o}F$$

This temperature difference is only 0.1% of the adiabatic temperature rise of the air in the airbag. Therefore, the heat transfer effect on overall energy is negligible. The adiabatic assumption is quite good. The compression happens in less than a second; the temperature changes are low, and the heat transfer coefficients are low. Therefore, little heat is transferred, justifying the adiabatic assumption.

The fabric area under the collidant is assumed strained because of the relatively frictionless contact with the collidant. The friction coefficient of fabric on gondola is only 0.26 as measured empirically with the angled slide test.

E. Conclusion

In summary, the unknowns are solved by conservation laws, kinematic equations, state equations, and differential equations. The kinematic equations determine airbag volume, leak area, pore area, and area of the cut. These equations can be quite complicated and hence addressed in their own chapter (4). The state equations determine the airbag hoop strains, the airbag pore conditions, and the control volume density and temperature. The differential equations determine the control volume air mass and pressure, the collidant elevation and velocity, and optionally, airbag longitudinal strains.

The equation that solves for collidant elevation z is the force equilibrium for the collidant. The equation that solves for airbag air mass m is the conservation of mass. The equation that solves for the airbag pressure P is the conservation of energy.

m = mass of air inside airbag by integration of Equation (3-2);

z = elevation of the collidant bottom by integration of Equation (3-22);

P = absolute pressure inside airbag by integration of Equation (3-62);

The Ideal Gas Law solves for the airbag air temperature T, and the definition of density, $\rho = m/V$, solves for density. The equilibrium for lateral forces solves for the hoop stress, σ_H. The equilibrium for longitudinal forces solves for the longitudinal stress, σ_L. The constitutive stress-strain relation determines the strains from the stresses. The permeability equation solves for pore entrance air velocity u_p. The pore area A_p is defined by microscopic examination and strain. The specific energy of the air at the pore entrance e_p is defined by thermal and kinetic energy.

In order to predict the behavior of airbags, a mathematical model was developed. A system of three differential equations in time were derived by applying Newton's second Law to the collidant, conservation of mass and energy to the airbag control volume, and static equilibrium to the fabric. Hence a system of three differential equations of state was employed to solve for the mass, position, and pressure variables. The following quantities of interest are calculated as a post processing step.

T = absolute temperature of air in airbag by Equation (3-50);

e = specific energy of air in the control volume;

u_p = velocity of air into the airbag pore by Equation (3-5);

P_p = pore entrance air pressure by Equation (3-6);

e_p = specific energy of air entering pore by Equation (3-9);

T_p = pore entrance air temperature by Equation (3-7);

M_p = pore entrance air Mach number by Equation (3-8);

Chapter IV: Kinematics of Collidant Impact

A. Overview

The primary assumption of the collidant-airbag impact is one-dimensional kinematics governed by the collidant (gondola) elevation coordinate, z. Assumed geometries throughout the impact reduce the system to one spatial degree of freedom. The airbag geometry is assumed to start as a cylinder with a hemisphere on top before gondola impact as seen in Figure 4-1 with the attendant actual airbag photograph. A second kinematic assumption is a state of uniform strain in the hoop and longitudinal directions, ε_L and ε_H, respectively.

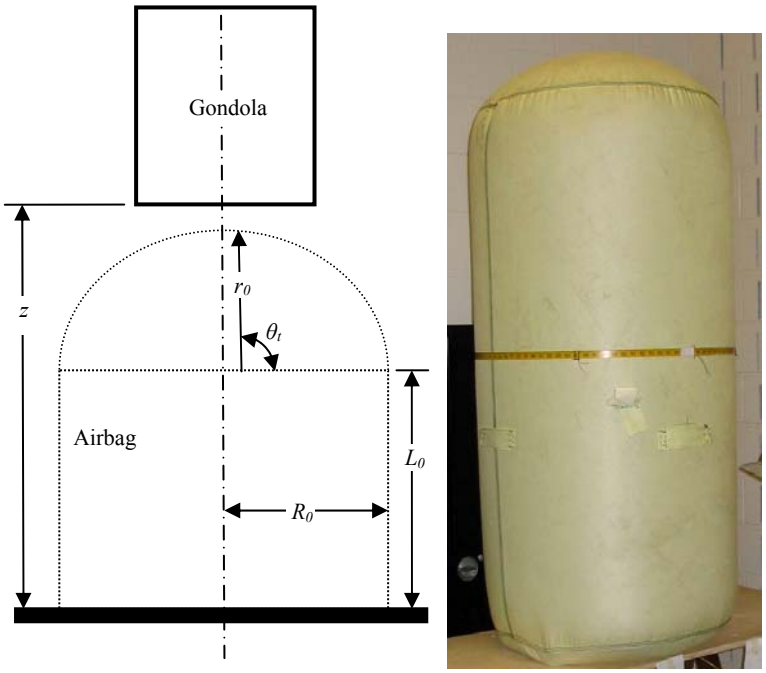

Figure 4-1: Gondola and Airbag Pre-Impact

The gondola hits the top of the airbag and plunges it inward on itself. The gondola forces the top of the airbag to progress through several shapes – first, a flattened dome, second, a partial bubble, third, a full bubble. These shapes are shown in cross section in Figure 4-2 and designated as Phases 1, 2, and 3.

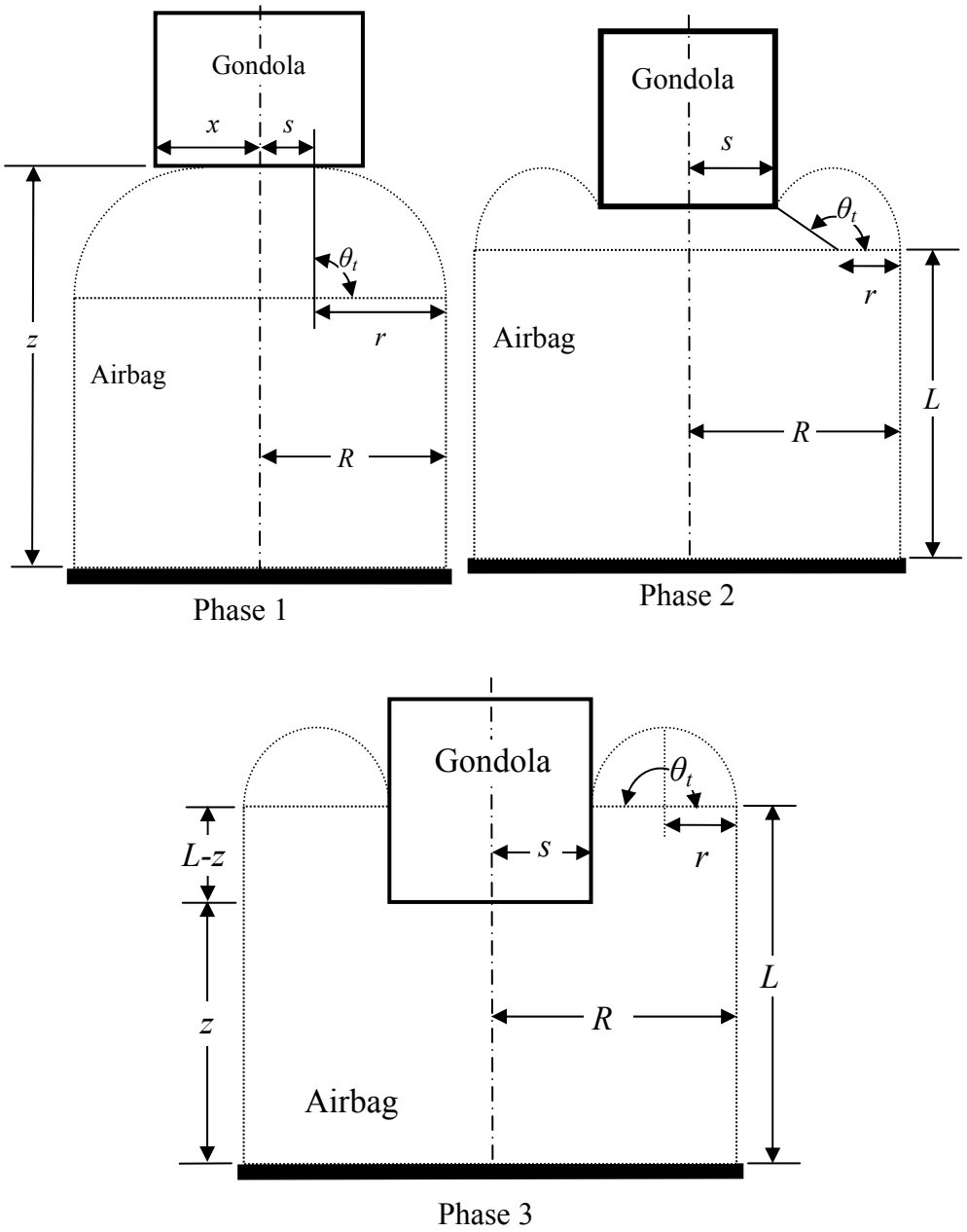

Figure 4-2: Gondola Airbag Impact Phases 1, 2, and 3

These phases can change at a given gondola elevation z as the cross sectional view is rotated in azimuth (about the z axis.) Because the gondola face impacting the airbag is either square or rectangular, the cross section length, $2s$, in Phases 2 and 3 shortens or lengthens as the cross-sectional view is rotated in azimuth. For each time step in a numerical approximation of the impact, a gondola elevation z is calculated. At each z, integration through the azimuth angle φ with its attendant dome angle θ_t that delineates one phase from another, as shown next, provides a good approximation of the airbag surface area and volume.

As the gondola contacts the hemisphere in Phase 1, it flattens the top of the dome. As the gondola moves downward entering Phase 2, the airbag shape changes as seen in Figure 4-2. In the third and final phase, the gondola is fully immersed into the airbag. Because an impact can involve different phases along the edge of the gondola impact face at any time step, a phase may exist for only a segment along the edge of the gondola covered by azimuth angle $\Delta\varphi$. Figure 4-3 shows a top view of the gondola impacting the airbag over time and the progression of the phases. The first frame has pure Phase 1 contact. Frame 2 shows the onset of Phase 2 splitting the top with Phase 1. Frame 3 shows Phase 2 closing in on Phase 1 from both sides. Frame 4 shows the onset of Phase 3 while Phase 2 is still active. Frame 5 shows pure Phase 3.

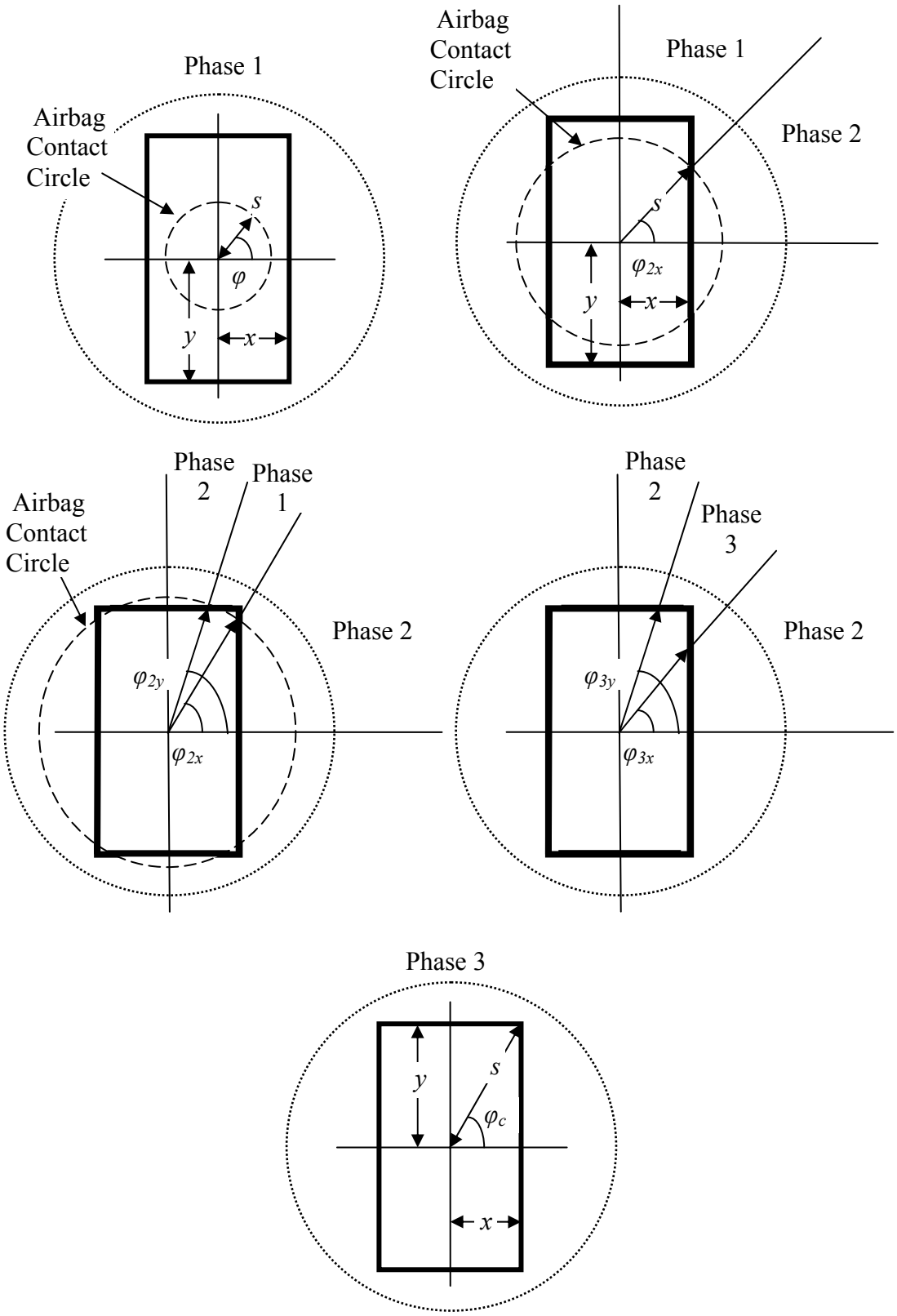

Figure 4-3: Top View of Airbag and Gondola Showing Contact

Each phase has different kinematic equations. The kinematic equations depend on the state variables z, ε_L, and ε_H, and the geometric initial conditions of airbag cylinder length L_0 and radius R_0 and gondola face width $2x$ and length $2y$ to calculate the changing airbag dimensions R, r, L, s, and θ_t. All phases of impact have the same equations for R and r. The airbag cylinder radius R is determined by cylinder hoop strain ε_H, hence:

$$R = R_0(1+\varepsilon_H) \tag{4-1}$$

The airbag dome meridional arc radius length r is calculated based on the geometrical constraint of horizontal compatibility:

$$r(1-\cos\theta_t) = R - s \;\rightarrow\; r = \frac{R-s}{1-\cos\theta_t} \tag{4-2}$$

Therefore, the unknown variables unique to each Phase are L, s, and θ_t. Subscripted indices are used for these variables when distinguishing among expressions appropriate to particular phases.

The selection of kinematic model is based on the phase of the impact. Before gondola impact, $z > L + R$, and the no-impact model for gondola free fall is used. When impact occurs, $z = L + R$, and the model switches to the Phase 1 impact equations. Subsequently, $z < L + R$. The model remains in Phase 1 as long as the radius of flattening s_1 is:

$$s_1 < \begin{cases} x\sec\phi, \text{ if } \phi \le \phi_C \\ y\csc\phi, \text{ if } \phi > \phi_C \end{cases} \tag{4-3}$$

otherwise the mode switches to the Phase 2 equations. The system stays in Phase 2 as long as $\theta_t < 180^o$, or equivalently $z > L$, otherwise it switches to Phase 3. Because the transitions in and out of Phase 2 are more complicated, pure Phase 1 and 3 are described

first and then pure Phase 2. Transitions from one Phase to the next are described afterwards. Finally, equations for airbag surface area and volume are derived for all combinations of Phases.

B. Phases of Impact

1. Phase 1: Initial Impact.

a. Geometry Definitions: See Figure 4-1 for definitions of the vertical cylindrical airbag and gondola in two dimensions. The airbag cylinder radius is R and unstrained is R_0. Upon impact, the hemispherical dome radius, $r = R$. Subsequently, Equation (4-2) determines r, designated as r_1 during Phase 1. The height of the airbag cylinder up to the edge of the dome arc is L, with L_0 being the initial length. The vertical dotted line is the centerline of the airbag and gondola. Two additional equations are needed for the two unknowns L_1 and s_1.

Figure 4-4 shows the gondola hitting the airbag's hemispherical domed top and flattening it. The radius of flattening is s_1; the half width of the gondola is x. The radius of the dome arc is now r_1.

b. Assumptions: Airbag dome meridional arc terminal angle θ_t remains at 90^o.

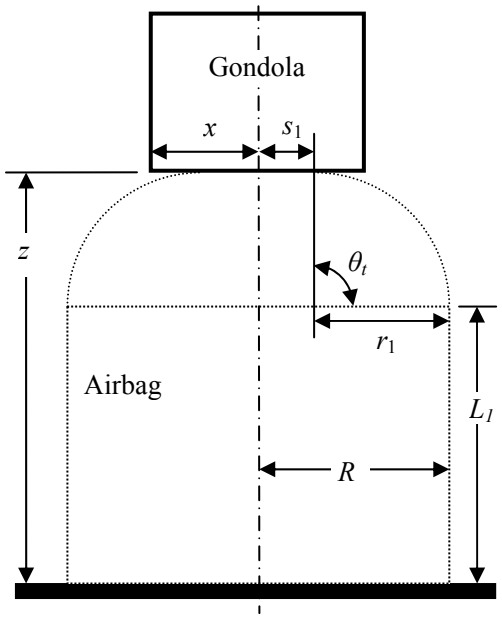

Figure 4-4: Gondola Initial Airbag Impact

Figure 4-5 shows the top view of the transparent gondola, airbag, and layout of dimensions s_1, x, y, and φ needed in the surface area and volume calculations for the case of Phase 1. The contact radius s_1 and cylinder side length L_1 are calculated from vertical compatibility and an assumption of fabric continuity.

$$\text{Vertical Compatibility:} \quad L_1 = z - r_1 \sin\theta_t = z - r_1 \tag{4-4}$$

$$\text{Fabric Continuity:} \quad s_1 + L_1 + r_1\theta_t = \left(L_0 + R_0\right)\left(1 + \varepsilon_L\right) = C \tag{4-5}$$

where ε_L is the longitudinal strain, vertical along the cylinder and meridional along the dome. In reality, the meridional strain grows larger along the dome arc. The fabric area under the collidant is assumed strained because of the relatively frictionless contact with the collidant. The friction coefficient of fabric on gondola is only 0.26 as measured empirically with the angled slide test.

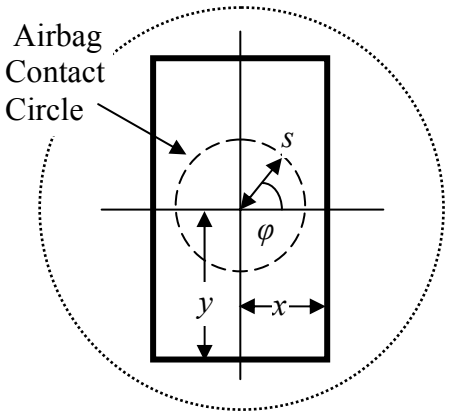

Figure 4-5: Top View of Airbag and Gondola Showing Contact

c. Derivation of Phase 1 Kinematic Equations: The gondola contact length on the airbag s_1, is calculated from the fabric continuity Equation (4-5). Substituting Equations (4-2) and (4-4), and assuming $\theta_t = \pi/2$, Equation (4-5) is solved for s in terms of constants and state variables for gondola height and airbag strain.

$$s_1 = C - L_1 - r_1\frac{\pi}{2} = C - z + r_1\left(1-\frac{\pi}{2}\right) = \frac{C - z + R\left(1-\frac{\pi}{2}\right)}{2-\frac{\pi}{2}} \tag{4-6}$$

Substituting Equation (4-6) for s_1 into equation (4-2) yields:

$$r_1 = R - s_1 = \frac{R - C + z}{2-\frac{\pi}{2}} \tag{4-7}$$

Equation (4-7) is easily determined in conjunction with Equation (4-5) for fabric continuity, given ε_L, which is assumed uniform throughout the fabric. In order to lift the restriction of uniform longitudinal stress and strain in the future, it will be convenient to express r_1 in terms of pressure rather than longitudinal strain. Substituting for strain from

Equation (3-17) and for stress from Equation (3-12) yields a quadratic equation for r_1 in terms of gauge pressure:

$$r_1 = \frac{R - (L_0 + R_0)\left(1 + \frac{P_g\left(r_1 - \frac{r_1^2}{2R} - \nu_L R\right)}{tE_L}\right) + z}{2 - \frac{\pi}{2}} \tag{4-8}$$

Solving for r_1 will express a positive real r_1 in terms of state variables from the following quadratic equation.

$$r_1 = \frac{-\left(2 - \frac{\pi}{2} + (L_0 + R_0)\frac{P_g}{tE_L}\right)}{(L_0 + R_0)\frac{P_g}{RtE_L}} \pm \frac{\sqrt{\left(2 - \frac{\pi}{2} + (L_0 + R_0)\frac{P_g}{tE_L}\right)^2 - 4(L_0 + R_0)\frac{P_g}{RtE_L}\left(-R + (L_0 + R_0)\left(1 - \frac{P_g \nu_L R}{tE_L}\right) - z\right)}}{(L_0 + R_0)\frac{P_g}{RtE_L}} \tag{4-9}$$

Finally, substituting Equation (4-7) into Equation (4-4) also expresses L_1 in terms of state variables.

$$L_1 = z - r_1 = \frac{C - R + z\left(1 - \frac{\pi}{2}\right)}{2 - \frac{\pi}{2}} \tag{4-10}$$

2. Phase 3: Full Impact.

a. Geometry Definitions: See Figure 4-6 for definitions of the geometry for the vertical cylindrical airbag and gondola in two dimensions. See Figure 4-7 for the top

view of the gondola, airbag, and layout of dimensions *s, x, y*, and φ_c, the azimuth angle to the gondola corner.

b. Assumptions: The airbag height to the dome edge L_3 shortens substantially because of the penetrating collidant. The airbag dome meridional arc θ_t is 180° all the way around the azimuth.

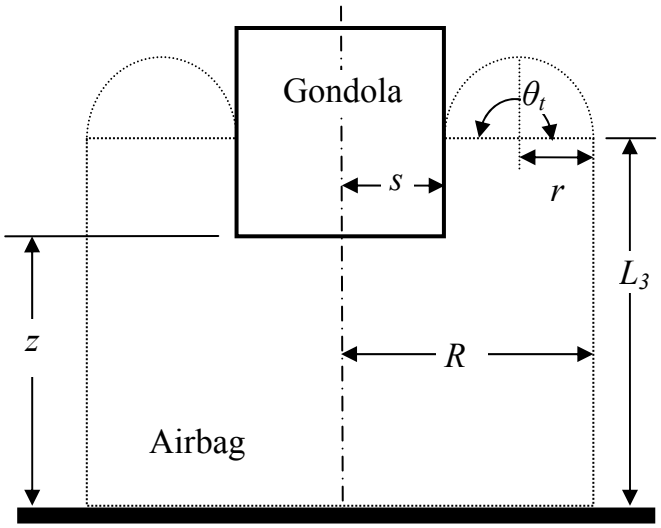

Figure 4-6: Gondola Fully Impacting Airbag

The gondola has impacted the airbag dome such that its bottom face is fully covered by the fabric. The remaining dome shape is governed by the dome meridional arc radius r, gondola face azimuth length s, and airbag cylinder edge height L_3.

c. Derivation of Phase 3 Kinematic Equations: With r_3 given by Equation (4-2), two equations for the two unknowns L_3 and s_3 are needed. Fabric continuity for Phase 3 is:

$$L_3 + \theta_t\, r + s_3 + L_3 - z = \left(L_0 + R_0\right)(1+\varepsilon_L) = C \tag{4-11}$$

Solving for L_3 from Equation (4-11) yields:

$$L_3 = \frac{1}{2}\left[C - \pi r_3 - s_3 + z\right] \tag{4-12}$$

The final equation needed is for fabric contact distance.

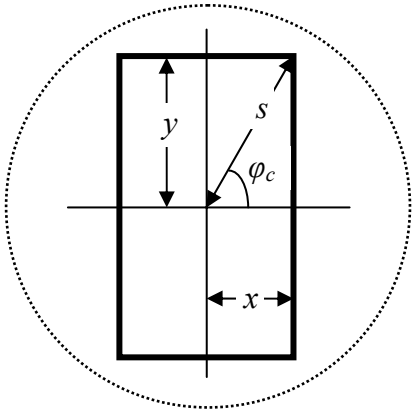

Figure 4-7: Top View of Airbag and Gondola

In pure Phase 3, the airbag contacts the gondola face all the way to its corner. The expression for the length of s_3 to the gondola edge in Figure 4-7 is discontinuous as the azimuth angle φ approaches the corner azimuth angle φ_C.

$$s_3 = s_2 = \begin{cases} x\sec\phi, & \text{if } \phi \le \phi_C \\ y\csc\phi, & \text{if } \phi > \phi_C \end{cases} \tag{4-13}$$

With s_3 given by Equation (4-13), r_3 and L_3 are determined in terms of state variables and constants, via Equations (4-2) and (4-12).

$$r_3 = \frac{R - s_3}{2} = \begin{cases} \dfrac{R - x\sec\phi}{2}, & \text{if } \phi \le \phi_C \\ \dfrac{R - y\csc\phi}{2}, & \text{if } \phi > \phi_C \end{cases} \tag{4-14}$$

$$L_3 = \begin{cases} \frac{1}{2}\left[C - \frac{\pi R}{2} + \left(\frac{\pi}{2} - 1 \right) x \sec\phi + z \right], & \text{if } \phi \le \phi_C \\ \frac{1}{2}\left[C - \frac{\pi R}{2} + \left(\frac{\pi}{2} - 1 \right) y \csc\phi + z \right], & \text{if } \phi > \phi_C \end{cases} \tag{4-15}$$

3. Phase 2: Intermediate Impact.

a. Geometry Definitions: See Figure 4-8 for definitions of the geometry for the vertical cylindrical airbag and gondola in two dimensions. For pure Phase 2 contact, the gondola has impacted the airbag dome such that its bottom face is fully covered by the fabric, similar to full Phase 3. The dome shape is governed by the airbag dome meridional radius r and airbag terminal meridional arc angle θ_t.

b. Assumptions: Airbag terminal dome arc angle θ_t varies during this phase expanding from 90° to 180°. The fabric contact length on the gondola face, s_2, is known from Equation (4-13).

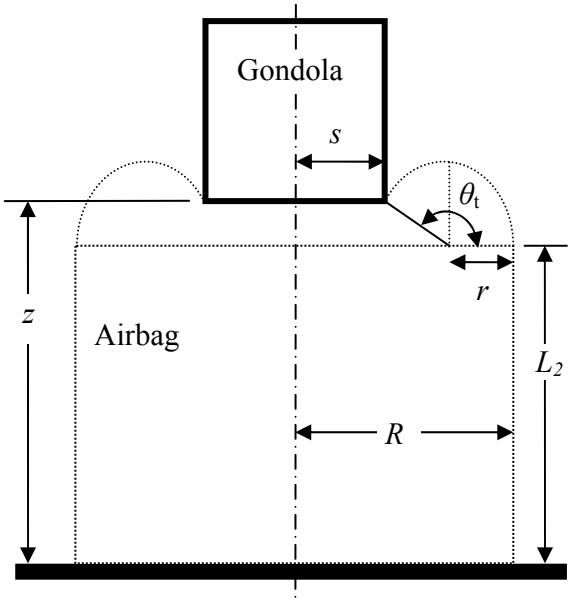

Figure 4-8: Gondola Intermediate Airbag Impact

c. Derivation of Phase 3 Kinematic Equations: The remaining dimensions (L_3, r_3, and θ_t) must be solved simultaneously from geometric compatibility and fabric continuity:

$$\text{Vertical Compatibility:} \quad z = L_2 + r_2 \sin\theta_t \quad \rightarrow \quad L_2 = z - r_2 \sin\theta_t \tag{4-16}$$

$$\text{Fabric Continuity:} \quad s_2 + L_2 + r_2\theta_t = \left(L_0 + R_0\right)(1+\varepsilon_L) = C \tag{4-17}$$

Solving Fabric Continuity equation (4-17) for θ_t, and substituting Equation (4-16) for L_2 gives

$$\theta_t = \frac{C - s_2 - z + r_2 \sin\theta_t}{r_2} \tag{4-18}$$

Substituting Equation (4-2) for r into Equation (4-18), delivers θ_t in terms of state variables in conjunction with Equation (4-13) for s_2.

$$\theta_t = \frac{\left[C - s_2 - z\right](1-\cos\theta_t)}{R - s_2} + \sin\theta_t \tag{4-19}$$

Angle θ_t is non-linear and transcendental in θ_t. Hence a non-linear equation solver is used to determine it.

Contact length s_2 is determined by the gondola face dimensions x and y and the azimuth angle φ according to Equation (4-13). Figure 4-7 from Phase 3 contact shows a top view of the gondola and airbag and defines the dimensions that apply to pure Phase 2 contact as well. In pure Phase 2, the airbag contacts the gondola contact face all the way around, such that Equation (4-17) applies. Therefore, there are two solutions to angle θ_t, one for each edge.

$$\theta_{tx} = \frac{\left[C - x\sec\phi - z\right](1-\cos\theta_{tx})}{R - x\sec\phi} + \sin\theta_{tx}, \text{ if } \phi \le \phi_C \tag{4-20}$$

$$\theta_{ty} = \frac{\left[C - y\csc\phi - z\right](1-\cos\theta_{ty})}{R - y\csc\phi} + \sin\theta_{ty}\text{, if } \phi > \phi_C \tag{4-21}$$

Likewise, there are two solutions for r_2 and L_2 from Equations (4-2) and (4-16).

$$r_2 = \frac{R - s_2}{1-\cos\theta_t} = \begin{cases} \dfrac{R - x\sec\phi}{1-\cos\theta_{tx}}, & if\ \phi \le \phi_C \\ \dfrac{R - y\csc\phi}{1-\cos\theta_{ty}}, & if\ \phi > \phi_C \end{cases} \tag{4-22}$$

$$L_2 = z - r_2\sin\theta_t = \begin{cases} z - \dfrac{R - x\sec\phi}{1-\cos\theta_{tx}}\sin\theta_{tx}, & \text{if } \phi \le \phi_C \\ z - \dfrac{R - y\csc\phi}{1-\cos\theta_{ty}}\sin\theta_{ty}, & \text{if } \phi > \phi_C \end{cases} \tag{4-23}$$

C. Transitions between Phases

1. Transition from Pre-Impact, Phase 0, to Phase 1.

Impact occurs when $s_1 = 0$ at an elevation found by solving Equation (4-6) for z when $s_1 = 0$.

$$z_0 = C + R\left(1 - \frac{\pi}{2}\right) \tag{4-24}$$

2. Transition from Phase 1 to 2.

The transition from Phase 1 dome contact to Phase 2 contact occurs when $\theta_t > \pi/2$, as shown in Figure 4-2 from a side view. From a top view, it is shown in Figure 4-9. Phase 2 contact exists along the gondola x-normal edge from $\varphi = 0$ to φ_{2x}, and Phase 2 equations apply. From $\varphi = \varphi_{2x}$ to 90°, the airbag dome is in Phase 1 contact, and Phase 1 equations apply. The elevation at which the transition occurs for a given azimuth angle is

found by setting $s_1 = s_2$ according to Equation (4-13), and solving Equation (4-6) for z. The resulting elevation at which Phase 1 ends is

$$z_1 = C + \left(1 - \frac{\pi}{2}\right) R + \left(\frac{\pi}{2} - 2\right) s_2 \tag{4-25}$$

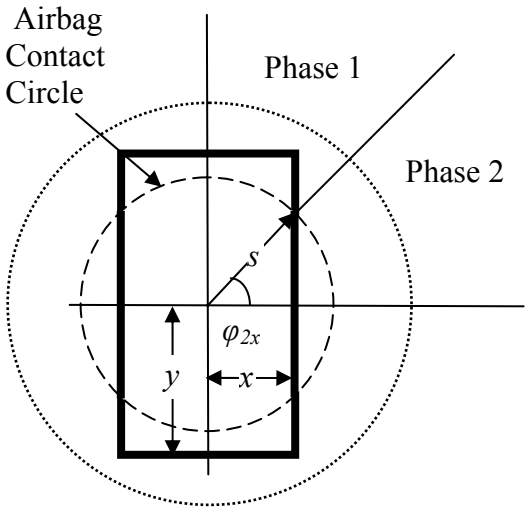

Figure 4-9: Top View of Airbag and Gondola Showing Contact

Phase 2 first begins when $\phi_{2x} = 0$ and $s_2 = x$. Full Phase 2 occurs when $\phi_{2x} = \phi_{2y} = \phi_C$ and $s_2 = \sqrt{x^2 + y^2}$. The corresponding elevation limits are found from Equation (4-24). In between these elevations, when Phase 1 begins and is completed, the transition azimuth angle must be determined.

Several conditions determine the value of φ_{2x}. If θ_t is π/2, then Phase 1 equations apply. If θ_t is between π/2 and π, then Phase 2 equations apply. If θ_t is π, then Phase 3 equations apply. The φ where the θ_t transitions from Phase 1 to 2 is φ_{2x}. Since Equation

(4-19) for θ_t is transcendental, a more tractable condition to indicate transition from Phase 1 to Phase 2 is the condition that Inequality (4-3) becomes an equality.

It is possible to need two φ_2 angles, one for the x-normal edge contact φ_{2x} and one for the y-normal edge contact φ_{2y}. Figure 4-10 shows this scenario and the two azimuth angles.

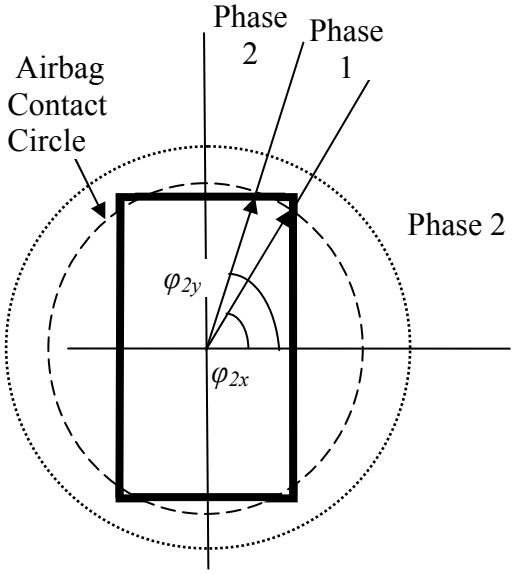

Figure 4-10: Top View of Airbag and Gondola Showing Contact

Solving Equation (4-17) for s_2 and using Equation (4-16) for L_2 and Equation (4-22) for r_2, leads to

$$s_2 = C - L_2 - r_2\theta_t = C - z + r_2\left(\sin\theta_t - \theta_t\right) = C - z + \frac{R - s_2}{1 - \cos\theta_t}\left(\sin\theta_t - \theta_t\right) \qquad (4\text{-}26)$$

At the transition from Phase 1 to 2, θ_t is $\pi/2$. Hence

$$s_2 = C - z + \left(R - s_2\right)\left(1 - \frac{\pi}{2}\right) \qquad (4\text{-}27)$$

Substituting Equation (4-13) as the definition for s_2 yields

$$\left(2-\frac{\pi}{2}\right)x\sec\phi_{2x}=C+\left(1-\frac{\pi}{2}\right)R-z \tag{4-28}$$

Recall that C depends on ε_L and R depends on ε_H.

When uniform strain is assumed, Equation (4-28) may be solved directly for the transition angle ϕ_{2x}. When ε_L and ε_L are allowed to vary with azimuth, it is more convenient to solve for the transition angle in terms of the pressure. Substituting fabric continuity constant C from Equation (4-17) together with the constitutive Equation (3-17) for ε_L along with the Tsai substitution [3-3: pg 17] yields

$$\left(2-\frac{\pi}{2}\right)x\sec\phi_{2x}=\left(L_0+R_0\right)\left(1+\frac{\sigma_L-\nu_L\sigma_H}{E_L}\right)+\left(1-\frac{\pi}{2}\right)R-z \tag{4-29}$$

Substituting longitudinal and hoop stress Equations (3-10) and (3-12) for the stresses results in

$$\left(2-\frac{\pi}{2}\right)x\sec\phi_{2x}=\left(L_0+R_0\right)\left(1+\frac{P_g\left(r_2-\frac{r_2^2}{2R}-\nu_L R\right)}{tE_L}\right)+\left(1-\frac{\pi}{2}\right)R-z \tag{4-30}$$

Substituting Equation (4-20) for r_2 and $\theta_t = \pi/2$ yields

$$\left(2-\frac{\pi}{2}\right)x\sec\phi_{2x}=\left(L_0+R_0\right)\left(1+\frac{P_g\left(R-x\sec\phi_{2x}-\frac{\left(R-x\sec\phi_{2x}\right)^2}{2R}-\nu_L R\right)}{tE_L}\right)+\left(1-\frac{\pi}{2}\right)R-z \tag{4-31}$$

Expanding terms, consolidating, and separating variables into a quadratic equation that can be solved for the transition angle in terms of gauge pressure

$$\phi_{2x} = arc\sec\left\{\frac{\left(\frac{\pi}{2}-2\right)\pm\sqrt{\left(2-\frac{\pi}{2}\right)^2-\left(L_0+R_0\right)\frac{P_g}{tE_L}\left[\left(L_0+R_0\right)\left(2+\frac{P_gR\left(1-2\nu_L\right)}{tE_L}\right)+\left(2-\pi\right)R-2z\right]}}{x\left(L_0+R_0\right)\frac{P_g}{tE_L}}\right\}$$

(4-32)

Equivalently, for φ_{2y}

$$\phi_{2y} = arc\csc\left\{\frac{\left(\frac{\pi}{2}-2\right)\pm\sqrt{\left(2-\frac{\pi}{2}\right)^2-\left(L_0+R_0\right)\frac{P_g}{tE_L}\left[\left(L_0+R_0\right)\left(2+\frac{P_gR\left(1-2\nu_L\right)}{tE_L}\right)+\left(2-\pi\right)R-2z\right]}}{y\left(L_0+R_0\right)\frac{P_g}{tE_L}}\right\}$$

(4-33)

This scenario changes the limits of integration for Phase 1 and 2 surface and volume integrals introduced in Sections 7 and 8. For Phase 1 calculations, φ_{2x} and φ_{2y} are used as the limits of integration rather than 0 and π/2. For the Phase 2 calculations, instead of corner azimuth angle φ_C as a limit, φ_{2x} and φ_{2y} are used.

3. Transition from Phase 2 to 3.

The transition from Phase 2 dome contact to Phase 3 contact, shown in Figures 4-2 and 4-11, occurs when $\theta_t = \pi$ and at the same time when $z = L$. This situation occurs first at the corner.

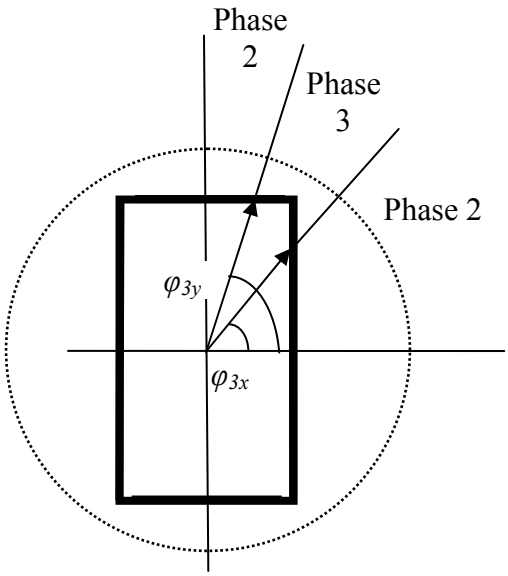

Figure 4-11: Top View of Airbag and Gondola Showing Contact

Phase 3 contact exists along the gondola edges from φ_{3y} to φ_{3x}, and Phase 3 equations apply. From $\varphi = \varphi_{3y}$ to 90^o and from 0^o to φ_{3x}, the airbag dome is in Phase 2 contact, and Phase 2 equations apply. The elevation at which the transition occurs for a given azimuth angle is found by setting $L_3 = z$ and solving Equation (4-15) for z. The resulting elevation at which Phase 2 ends is

$$z_2 = C - \frac{\pi}{2}R + \left(\frac{\pi}{2} - 1\right)s_3 \tag{4-34}$$

Phase 3 first begins when $\phi_{3x} = \phi_{3y} = \phi_C$ and $s_3 = \sqrt{x^2 + y^2}$. Full Phase 3 occurs when $\phi_{3x} = 0, \text{and } s_3 = x$. The corresponding elevation limits are found from Equation (4-28). Between these elevations, when Phase 2 begins and is completed, the transition azimuth angles must be determined. The phase-transition azimuth angles φ_{3x} and φ_{3y} are determined by solving Equation (4-15) under condition that $z = L_3$. At the transition from Phase 2 to 3, θ_t is π and the following is true.

$$s_3 = s_2 = C - z - \frac{R - s_3}{2}\pi \tag{4-35}$$

Separating s_3 and substituting Equation (4-13) as the definition for s_3 and Equation (4-17) for the definition of C yields

$$\left(1 - \frac{\pi}{2}\right) x \sec \phi_{3x} = C - \frac{\pi}{2} R - z \tag{4-36}$$

Once again, given uniform strain, Equation (4-36) may be solved directly for the transition angle ϕ_{3x}.

When ε_L and ε_L are allowed to vary with azimuth, it is more convenient to solve for the transition angle in terms of the pressure. Substituting the fabric continuity constant from Equation (4-11), together with the constitutive Equation (3-3) for ε_L along with the Tsai substitution [3-3: pg 17] yields

$$\left(1 - \frac{\pi}{2}\right) x \sec \phi_{3x} = \left(L_0 + R_0\right)\left(1 + \frac{\sigma_L - \nu_L \sigma_H}{E_L}\right) - \frac{\pi}{2} R - z \tag{4-37}$$

Substituting longitudinal and hoop stress Equations (3-10) and (3-12) for the stresses results in

$$\left(1 - \frac{\pi}{2}\right) x \sec \phi_{3x} = \left(L_0 + R_0\right)\left(1 + \frac{P_g\left(r_3 - \frac{r_3^2}{2R} - \nu_L R\right)}{tE_L}\right) - \frac{\pi}{2} R - z \tag{4-38}$$

Substituting Equation (4-14) for r_3 and $\theta_t = \pi$ yields

$$\left(1-\frac{\pi}{2}\right)x\sec\phi_{3x}=\left(L_0+R_0\right)\left(1+\frac{P_g\left(R-x\sec\phi_{3x}-\frac{\left(R-x\sec\phi_{3x}\right)^2}{4R}-\nu_L R\right)}{2tE_L}\right)-\frac{\pi}{2}R-z$$

(4-39)

Expanding terms, consolidating, and separating variables yields a quadratic equation that can be solved for the transition angle in terms of pressure

$$\phi_{3x}=arc\sec\left\{\frac{\left\{-\left(1-\frac{\pi}{2}+\left(L_0+R_0\right)\frac{P_g}{4tE_L}\right)\pm\sqrt{\left(1-\frac{\pi}{2}+\left(L_0+R_0\right)\frac{P_g}{4tE_L}\right)^2-\frac{\left(L_0+R_0\right)P_g}{tE_LR}\left\{\left(L_0+R_0\right)\left(1+\frac{P_gR\left(3-4\nu_L\right)}{8tE_L}\right)-\frac{\pi}{2}R-z\right\}}\right\}}{\frac{x\left(L_0+R_0\right)P_g}{4tE_LR}}\right\}$$

(4-40)

Equivalently, for φ_{3y}

$$\phi_{3y}=arc\csc\left\{\frac{\left\{-\left(1-\frac{\pi}{2}+\left(L_0+R_0\right)\frac{P_g}{4tE_L}\right)\pm\sqrt{\left(1-\frac{\pi}{2}+\left(L_0+R_0\right)\frac{P_g}{4tE_L}\right)^2-\frac{\left(L_0+R_0\right)P_g}{tE_LR}\left\{\left(L_0+R_0\right)\left(1+\frac{P_gR\left(3-4\nu_L\right)}{8tE_L}\right)-\frac{\pi}{2}R-z\right\}}\right\}}{\frac{y\left(L_0+R_0\right)P_g}{4tE_LR}}\right\}$$

(4-41)

D. Airbag Surface Area and Volume

1. Airbag Exposed Surface Area.

The exposed airbag surface area A_L that might leak gas through the pores of the fabric is the area of the airbag cylinder walls and the exposed area of the airbag dome. The differential surface area dA_L in the dome, generic to all phases, is calculated by multiplying a differential meridional arc $rd\theta$ times a differential circumference as seen in Figure 4-12. The differential circumference is calculated by multiplying the horizontal radius from the airbag centerline to the dome skin $s + r(\cos\theta - \cos\theta_t)$ by the differential azimuth angle $d\varphi$.

$$dA_L = rd\theta[s + r(\cos\theta - \cos\theta_t)]d\phi \tag{4-42}$$

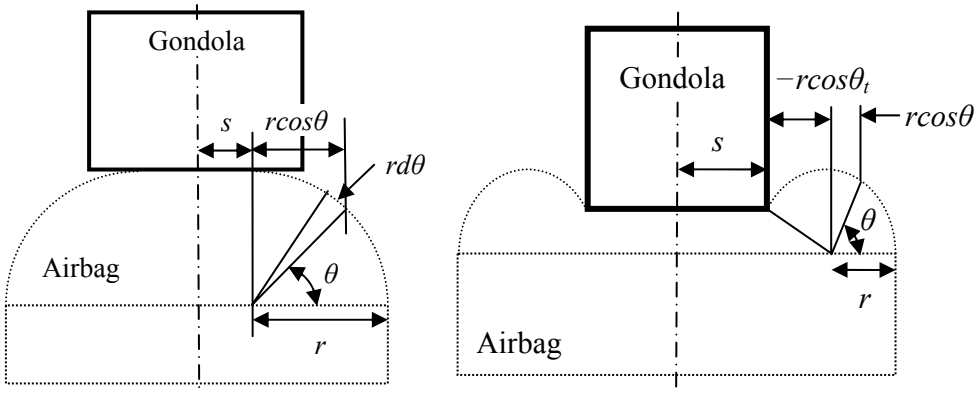

Figure 4-12: Dome Differential Surface Area

The resulting exposed dome and cylinder wall surface area integral, generic to all phases, with a symmetrical gondola and airbag is

$$\begin{aligned}\Delta A_L &= 4\int_{\phi_1}^{\phi_2}\left[\int_0^{\theta_t} r\left(s + r(\cos\theta - \cos\theta_t)\right)d\theta + LR\right]d\phi \\ &= 4\int_{\phi_1}^{\phi_2}\left[r\left(s\theta_t + r(\sin\theta_t - \theta_t\cos\theta_t)\right) + LR\right]d\phi\end{aligned} \tag{4-43}$$

a. Phase 1 Surface Area: For the case of pure Phase 1 initial contact, airbag meridional arc terminal angle is $\theta_t = \pi/2$; hence the exposed area of the dome and cylinder wall surface area A_{L1} for Phase 1 can be calculated where the variables, r and s_1 are known from Equations (4-2) and (4-3).

$$\Delta A_{L1} = 4\int_{\phi_1}^{\phi_2}\left(rs_1\frac{\pi}{2} + r^2 + L_1R\right)d\phi = 4\left(rs_1\frac{\pi}{2} + r^2 + L_1R\right)\left(\phi_2 - \phi_1\right) \tag{4-44}$$

For the case of pure Phase 1, i.e. all around the azimuth, $\Delta\varphi = \varphi_2 - \varphi_1 = \pi/2$; hence the dome and cylinder surface area is

$$A_{L1} = 2\pi\left(rs_1\frac{\pi}{2} + r^2 + L_1R\right) = \pi^2 rs_1 + 2\pi r^2 + 2\pi L_1R \tag{4-45}$$

b. Phase 3 Surface Area: The generic integral for the dome and cylinder exposed surface Equation (4-43) is used with $\Delta\varphi = \pi/2$, but, for pure Phase 3, θ_t is π and r is a function of s from Equation (4-2).

$$A_{L3} = 4\int_{\phi_{3x}}^{\phi_{3y}}\left(\frac{R^2 - {s_3}^2}{4}\pi + L_3R\right)d\phi \tag{4-46}$$

However, due to the discontinuity of Equation (4-13), the integral is broken into two parts, as shown in Figure 4-11. Substituting Equation (4-13) in for s_3,

$$A_{L3} = \int_{\phi_{3x}}^{\phi_C}\left(\pi R^2 - \pi x^2\sec^2\phi + 4L_3R\right)d\phi \; + \int_{\phi_C}^{\phi_{3y}}\left(\pi R^2 - \pi y^2\csc^2\phi + 4L_3R\right)d\phi \tag{4-47}$$

Substituting Equation (4-15) in for L_3,

$$A_{L3} = \int_{\phi_{3x}}^{\phi_C} \left(-\pi x^2 \sec^2\phi + (\pi - 2) Rx \sec\phi + 2R(C+z)\right) d\phi + \int_{\phi_C}^{\phi_{3y}} \left(-\pi y^2 \csc^2\phi + (\pi - 2) Ry \csc\phi + 2R(C+z)\right) d\phi \tag{4-48}$$

In the case of pure Phase 3 contact, $\varphi_{3x} = 0$ and $\varphi_{3y} = \pi / 2$.

c. Phase 2 Surface Area: The generic integral for the dome and cylinder surface area (4-43) applies; however, for Phase 2, not only is r a function of s and θ_t from Equation (4-2), but also θ_t is a transcendental function that depends on φ. Therefore, the surface area integral, which includes θ_t integrated with respect to $d\varphi$, must be solved numerically.

$$A_{L2} = 4\int_{\phi_1}^{\phi_2} \left(\frac{R - s_2}{1 - \cos\theta_t} s_2 \theta_t + \left(\frac{R - s_2}{1 - \cos\theta_t} \right)^2 (\sin\theta_t - \theta_t \cos\theta_t) + L_2 R \right) d\phi \tag{4-49}$$

Pure Phase 2 dome contact is discontinuous at the gondola impact face corner; therefore, substituting Equation (4-13) into Equation (4-49) yields

$$A_{L2} = 4\int_{0}^{\phi_C} \left(\frac{R - x\sec\phi}{1 - \cos\theta_{tx}} \theta_{tx} x \sec\phi + \left(\frac{R - x\sec\phi}{1 - \cos\theta_t} \right)^2 (\sin\theta_{tx} - \theta_{tx}\cos\theta_{tx}) + Rz \right) d\phi + 4\int_{\phi_C}^{\pi/2} \left(\frac{R - y\csc\phi}{1 - \cos\theta_{ty}} \theta_{ty} y \csc\phi + \left(\frac{R - y\csc\phi}{1 - \cos\theta_t} \right)^2 (\sin\theta_{ty} - \theta_{ty}\cos\theta_{ty}) + Rz \right) d\phi \tag{4-50}$$

Since θ_t is transcendental and a function of φ, Equation (4-50) must be solved numerically.

d. Phases 1 and 2 Active Surface Area: The generic surface integral for the dome and cylinder (4-43) applies, however, for Phases 1 and 2 active, different integration limits apply as the surface integrals are added.

$$A_L = 4\int_{\phi_{2x}}^{\phi_{2y}} \left((R-s_1)s_1\frac{\pi}{2} + (R-s_1)^2 + L_1 R \right) d\phi$$
$$+ 4\int_{0}^{\phi_{2x}} \left(\frac{R - x\sec\phi}{1-\cos\theta_{tx}}\theta_{tx} x\sec\phi + \left(\frac{R - x\sec\phi}{1-\cos\theta_t}\right)^2 \left(\sin\theta_{tx} - \theta_{tx}\cos\theta_{tx}\right) + Rz \right) d\phi \qquad (4\text{-}51)$$
$$+ 4\int_{\phi_{2y}}^{\pi/2} \left(\frac{R - y\csc\phi}{1-\cos\theta_{ty}}\theta_{ty} y\csc\phi + \left(\frac{R - y\csc\phi}{1-\cos\theta_t}\right)^2 \left(\sin\theta_{ty} - \theta_{ty}\cos\theta_{ty}\right) + Rz \right) d\phi$$

In Equation (4-51), R, known from Equation (4-1), r from (4-2), s_1 from (4-6), and L_1 from (4-10), are all explicit functions of state variables and parameters. On the other hand, angle θ_{tx} angle θ_{ty} depend on φ from Equations (4-18) and (4-19). The first integral of Equation (4-51) is evaluated explicitly in Equation (4-43) leaving the second and third integrals to be evaluated numerically.

Either Phase can be eliminated by collapsing the integration limits. If Phase 1 is over, φ_{2x} and φ_{2y} become φ_C. If Phase 2 is absent, φ_{2x} becomes 0 and φ_{2y} becomes $\pi/2$.

The typical impact progression is for s_1 to start at zero and then bloom out on impact until it equals x or y. Then φ_{2x} and φ_{2y} start growing from zero. In Phase 1, s_1 keeps growing until it equals x sec φ_C or y csc φ_C, then Phase 1 ends. Phase 2 remains active until $\varphi_{3x} = 0$.

The rebound is the reverse order. First, z rises above L at the side, $\varphi = 0$, initiating Phase 2. Then φ_{3x} and φ_{3y} tend toward φ_C, at the corner. When s_1 drops below x sec φ_C or y csc φ_C, then Phase 1 becomes active at the corner and spreads outward until engulfing the whole circumference. Then s_1 shrinks to zero and the impact is over.

e. Phases 2 and 3 Active Surface Area: The generic surface integral for the dome and cylinder (4-43) applies, however, for Phases 2 and 3 active, different integration limits apply as all the surface integrals are added.

$$
\begin{aligned}
A_L = {} & 4\int_0^{\phi_{3x}} \left(\frac{R - x\sec\phi}{1-\cos\theta_{tx}}\theta_{tx} x\sec\phi + \left(\frac{R - x\sec\phi}{1-\cos\theta_t}\right)^2 \left(\sin\theta_{tx} - \theta_{tx}\cos\theta_{tx}\right) + Rz \right) d\phi \\
& + 4\int_{\phi_{3y}}^{\pi/2} \left(\frac{R - y\csc\phi}{1-\cos\theta_{ty}}\theta_{ty} y\csc\phi + \left(\frac{R - y\csc\phi}{1-\cos\theta_t}\right)^2 \left(\sin\theta_{ty} - \theta_{ty}\cos\theta_{ty}\right) + Rz \right) d\phi \\
& + \int_{\phi_{3x}}^{\phi_C} \left(-\pi x^2 \sec^2\phi + (\pi - 2) Rx\sec\phi + 2R(C+z) \right) d\phi \\
& + \int_{\phi_C}^{\phi_{3y}} \left(-\pi y^2 \csc^2\phi + (\pi - 2) Ry\csc\phi + 2R(C+z) \right) d\phi
\end{aligned}
\tag{4-52}
$$

In Equation (4-52), R, known from Equation (4-1), r from (4-2), are all explicit functions of state variables and parameters. On the other hand, angle θ_{tx} angle θ_{ty} depend on φ from Equations (4-20) and (4-21) and C depends on φ from Equation (3-12). Hence Equation (4-52) must be evaluated numerically.

Either Phase can be eliminated by collapsing the integration limits. If Phase 3 is absent, φ_{3x} and φ_{3y} become φ_C. If Phase 2 is absent, φ_{3x} becomes 0 and φ_{3y} becomes $\pi/2$.

The typical impact progression is for z to drop to L at $\varphi = \varphi_C$ and Phase 3 begins with φ_{3x} and φ_{3y} growing from φ_C. Phase 2 remains active until φ_{3x} becomes 0 and φ_{3y} becomes $\pi/2$.

The rebound is the reverse order. First, z rises above L at the center of the faces, and φ_{3x} rises above 0 and φ_{3y} drops below $\pi/2$ initiating Phase 2 at the center of the faces.

2. Partial Derivatives of Geometry Factors.

Equation (3-35) calls for partial derivatives of geometric factors arising from static equilibrium. From Equation (3-10),

$$
A_H = \frac{R_0}{t}\left(1 + \varepsilon_H\right) \tag{4-53}
$$

The resulting partial derivatives using the comma notation are

$$A_{H,z} = 0, \quad A_{H,\varepsilon_H} = \frac{R_0}{t}, \quad A_{H,\varepsilon_L} = 0 \tag{4-54}$$

Likewise, from Equation (3-12),

$$A_{Long} = \frac{1}{t}\left(r - \frac{r^2}{2R} \right) \tag{4-55}$$

The resulting partial derivatives depend on the Phase of impact. For Phase 1, they are

$$A_{L1,z} = \frac{1}{t}\left(R_{,z} - s_{1,z} - \frac{1}{2}\frac{2R\left(R - s_1\right)\left(R_{,z} - s_{1,z}\right) - R_{,z}\left(R - s_1\right)^2}{R^2} \right) \tag{4-56}$$

$$A_{L1,\varepsilon_H} = \frac{1}{t}\left(R_0 - s_{,\varepsilon_H} - \frac{1}{2}\frac{2R\left(R - s\right)\left(R_0 - s_{,\varepsilon_H}\right) - R_0\left(R - s\right)^2}{R^2} \right) \tag{4-57}$$

$$A_{L1,\varepsilon_L} = \frac{1}{t}\left(R_{,\varepsilon_L} - s_{,\varepsilon_L} - \frac{1}{2}\frac{2R\left(R - s\right)\left(R_{,\varepsilon_L} - s_{,\varepsilon_L}\right) - R_{,\varepsilon_L}\left(R - s\right)^2}{R^2} \right) \tag{4-58}$$

For Phase 2, they are

$$A_{L2,z} = \frac{1}{t\left(1-\cos\theta_t\right)^2}\left\{ \left[\left(1-\cos\theta_t\right)\left(R_{,z} - s_{2,z}\right) - \left(R - s_2\right)\theta_{t,z}\sin\theta_t \right]\left(1 - \frac{R - s_2}{R\left(1-\cos\theta_t\right)} \right) + \frac{R_{,z}\left(R - s_2\right)^2}{2R^2} \right\} \tag{4-59}$$

$$A_{L2,\varepsilon_H} = \frac{1}{t\left(1-\cos\theta_t\right)^2}\left\{ \left[\left(1-\cos\theta_t\right)\left(R_{,\varepsilon_H} - s_{2,\varepsilon_H}\right) - \left(R - s_2\right)\theta_{t,\varepsilon_H}\sin\theta_t \right]\left(1 - \frac{R - s_2}{R\left(1-\cos\theta_t\right)} \right) + \frac{R_{,\varepsilon_H}\left(R - s_2\right)^2}{2R^2} \right\} \tag{4-60}$$

$$A_{L2,\varepsilon_L} = \frac{1}{t\left(1-\cos\theta_t\right)^2}\left\{\left[\left(1-\cos\theta_t\right)\left(R_{,z}-s_{2,\varepsilon_L}\right)-\left(R-s_2\right)\theta_{t,\varepsilon_L}\sin\theta_t\right]\left(1-\frac{R-s_2}{R\left(1-\cos\theta_t\right)}\right)+\frac{R_{,\varepsilon_L}\left(R-s_2\right)^2}{2R^2}\right\} \tag{4-61}$$

For Phase 3, they are

$$A_{L3,z} = \frac{1}{2t}\left(R_{,z}-s_{3,z}-\frac{1}{4}\frac{2R\left(R-s_3\right)\left(R_{,z}-s_{3,z}\right)-R_{,z}\left(R-s_3\right)^2}{R^2}\right) \tag{4-62}$$

$$A_{L3,\varepsilon_H} = \frac{1}{2t}\left(R_0-s_{3,\varepsilon_H}-\frac{1}{4}\frac{2R\left(R-s_3\right)\left(R_0-s_{3,\varepsilon_H}\right)-R_0\left(R-s_3\right)^2}{R^2}\right) \tag{4-63}$$

$$A_{L3,\varepsilon_L} = \frac{1}{2t}\left(R_{,\varepsilon_L}-s_{3,\varepsilon_L}-\frac{1}{4}\frac{2R\left(R-s_3\right)\left(R_{,\varepsilon_L}-s_{3,\varepsilon_L}\right)-R_{,\varepsilon_L}\left(R-s_3\right)^2}{R^2}\right) \tag{4-64}$$

3. Airbag Volume.

The airbag volume is divided into three mathematically practical components shown in Figure 4-13: 1) airbag main cylinder, 2) partial dome on airbag top, and 3) frustum under gondola. These volume components are integrated from differential azimuth slices $d\varphi$.

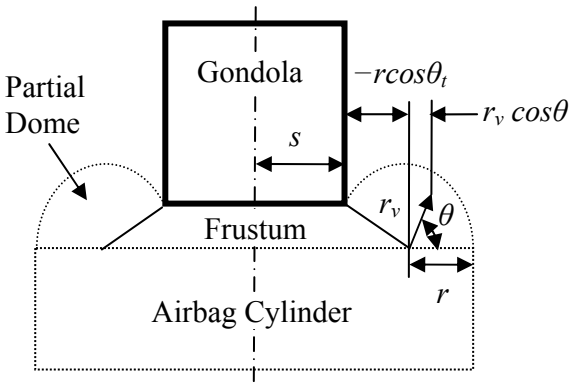

Figure 4-13: Differential Volume Components

The differential air volume in the cylinder is its differential surface element, $LRd\varphi$, times its differential thickness dR.

$$dV_{cylinder} = LRd\phi dR \tag{4-65}$$

The differential air volume in the partial dome is its differential meridional length, $r_v d\theta$, times its differential azimuth, $\left(s - r\cos\theta_t + r_v\cos\theta\right)d\phi$ times its differential thickness dr_v.

$$dV_{dome} = (s - r\cos\theta_t + r_v\cos\theta)\,d\theta\; r_v dr_v\, d\phi \tag{4-66}$$

The differential air volume in the frustum is its differential radius, dR_f, times differential arc length, $R_f\, d\varphi$, times its differential height dh.

$$dV_{frustum} = R_f d\phi dR_f dh \tag{4-67}$$

All the differential air volumes contain the differential azimuth angle $d\varphi$, but the rest of the differentials are unique to each volume. For clarity of explanation, the unique differentials are integrated separately first. The generic frustum volume requires the most explanation and thus is first. The height of the frustum, h, in Figure 4-14, varies from 0 to $r \sin \theta_t$, hence these are the integration limits for dh. The radius of the frustum R_f

varies from 0 to $s + h \cot \theta_t$, hence these are the integration limits. Though these limits invert the frustum, the volume is equivalent.

$$\begin{aligned} V_{frustum} &= \int_{\phi_1}^{\phi_2} \left[\int_0^{r\sin\theta_t} \left(\int_0^{s+h\cot\theta_t} R_f \, dR_f \right) dh \right] d\phi \\ &= \frac{1}{2} \int_{\phi_1}^{\phi_2} \left[\int_0^{r\sin\theta_t} \left(s^2 + 2sh\cot\theta_t + h^2 \cot^2\theta_t \right) dh \right] d\phi \\ &= \frac{1}{2} \int_{\phi_1}^{\phi_2} \left(s^2 r \sin\theta_t + sr^2 \sin\theta_t \cos\theta_t + \frac{r^3}{3} \sin\theta_t \cos^2\theta_t \right) d\phi \\ &= \frac{1}{2} \int_{\phi_1}^{\phi_2} \left(s^2 r + sr^2 \cos\theta_t + \frac{r^3}{3} \cos^2\theta_t \right) \sin\theta_t \, d\phi \end{aligned} \tag{4-68}$$

The generic dome volume is treated next.

$$\begin{aligned} V_{dome} &= \int_{\phi_1}^{\phi_2} \int_0^{\theta_t} \int_0^{r} (s - r\cos\theta_t + r_v \cos\theta) \, r_v \, dr_v \; d\theta d\phi \\ &= \int_{\phi_1}^{\phi_2} \int_0^{\theta_t} \left[\frac{r^2}{2} \left(s - r\cos\theta_t \right) + \frac{r^3}{3} \cos\theta \right] d\theta d\phi \\ &= \int_{\phi_1}^{\phi_2} \left[\frac{r^2}{2} \left(s - r\cos\theta_t \right) \theta_t + \frac{r^3}{3} \sin\theta_t \right] d\phi \end{aligned} \tag{4-69}$$

The generic cylinder volume is the least complicated.

$$V_{cylinder} = \int_{\phi_1}^{\phi_2} \int_0^{R} LR \, dR d\phi = \frac{1}{2} \int_{\phi_1}^{\phi_2} LR^2 \, d\phi \tag{4-70}$$

By combining the three generic volumes, the resulting generic airbag volume integral is

$$V = \frac{1}{2} \int_{\phi_1}^{\phi_2} \left(\left(s^2 r + sr^2 \cos\theta_t + \frac{r^3}{3} \cos^2\theta_t \right) \sin\theta_t + r^2 \left(s - r\cos\theta_t \right) \theta_t + \frac{2r^3}{3} \sin\theta_t + LR^2 \right) d\phi \tag{4-71}$$

where L, r, and s are functions of φ in Phases 2 and 3 but not Phase 1.

a. Phase 1 Volume: For the case of Phase 1 dome contact, meridional arc angle $\theta_t = \pi/2$, $L = L_1$, $r = r_1$, and $s = s_1$ none of which are functions of φ; hence the airbag volume is

$$\begin{aligned} V_1 &= \int_{\phi_{2x}}^{\phi_{2y}} \left(\frac{1}{2}\left(s_1^2 r_1\right) + \left[\frac{\pi r_1^2 s_1}{4} + \frac{r_1^3}{3} \right] + \frac{1}{2} L_1 R^2 \right) d\phi \\ &= \frac{1}{2}\left(s_1^2 r_1 + s_1 r_1^2 \frac{\pi}{2} + \frac{2}{3} r_1^3 + L_1 R^2 \right)\left(\phi_{2y} - \phi_{2x}\right) \end{aligned} \tag{4-72}$$

For the case of Phase 1 all around the azimuth, $\Delta\varphi$ is 2π; hence dome volume is

$$V_1 = \pi\left(s_1^2 r_1 + s_1 r_1^2 \frac{\pi}{2} + \frac{2}{3} r_1^3 + L_1 R^2 \right) \tag{4-73}$$

L_1, r_1, and s_1 are complicated functions of constants and state variables from Equations (4-6, 7, and 10).

b. Phase 3 Dome Volume: For the case of Phase 3 dome contact, $L = L_3$, $r = r_3$, and $s = s_3$, all of which are functions of φ. Also, meridional arc angle $\theta_t = \pi$; hence the frustum volume is zero. However, the generic volume Equation (4-71) does not account for the penetrating gondola; hence, a slice of the gondola must be subtracted. It is a slice of radius s_3 and height $L_3 - z$.

$$V_{gondola} = \int_{\phi_{3x}}^{\phi_{3y}} \int_0^{s_3} (L_3 - z)\, s\, ds d\phi = \frac{1}{2} \int_{\phi_{3x}}^{\phi_{3y}} (L_3 - z)\, s_3^2\, d\phi \tag{4-74}$$

The resulting Phase 3 airbag volume integral is

$$V_3 = \frac{1}{2} \int_{\phi_{3x}}^{\phi_{3y}} \left(\pi r_3^2 \left(s_3 + r_3\right) + L_3 R^2 - \left(L_3 - z\right) s_3^2 \right) d\phi \tag{4-75}$$

where L_3 and r_3 are functions of constants and state variables from Equations (4-14) and (4-15). Substituting Equation (4-13) in for s_3, provides clarity about the discontinuity at the corner.

$$\begin{aligned} V_3 &= \frac{1}{2}\int_{\phi_{3x}}^{\phi_C}\left(\pi r_3^2\left(x\sec\phi + r_3\right) + L_3R^2 - (L_3 - z)x^2\sec^2\phi\right)d\phi \\ &\quad + \frac{1}{2}\int_{\phi_C}^{\phi_{3y}}\left(\pi r_3^2\left(y\csc\phi + r_3\right) + L_3R^2 - (L_3 - z)y^2\csc^2\phi\right)d\phi \\ &= \int_{\phi_{3x}}^{\phi_C} V_{3x}\,d\phi + \int_{\phi_C}^{\phi_{3y}} V_{3y}\,d\phi \end{aligned} \tag{4-76}$$

c. Phase 2 Dome Volume: For the case of Phase 2 dome contact, $L = L_2$, $r = r_2$, and $s = s_2$, all of which are functions of φ. Also, meridional arc angle $\theta_t < \pi$, hence the frustum volume is greater than zero. The resulting generic integral Equation (4-71) becomes.

$$V_2 = \frac{1}{2}\int_{\phi_1}^{\phi_2}\left(\left(s_2^2 r_2 + s_2 r_2^2\cos\theta_t + \frac{r_2^3}{3}\cos^2\theta_t\right)\sin\theta_t + r_2^2\left(s_2 - r_2\cos\theta_t\right)\theta_t + \frac{2r_2^3}{3}\sin\theta_t + L_2R^2\right)d\phi \tag{4-77}$$

Since, for the case of Phase 2 contact, angle θ_t is a transcendental function of φ, the volume integral must be solved numerically. Phase 2 dome contact is discontinuous at the gondola face corner or at the Phase 3 transition. Therefore, substituting Equation (4-13) into Equation (4-77) yields

$$
\begin{aligned}
V_2 = \frac{1}{2}\int_0^{\phi_{2x}} \Bigg(\Bigg(& \left((x\sec\phi)^2 r_2 + x\sec\phi r_2^2 \cos\theta_{tx} + \frac{r_2^3}{3}\cos^2\theta_{tx} \right)\sin\theta_{tx} \\
& + r_2^2\left(x\sec\phi - r_2\cos\theta_{tx}\right)\theta_{tx} + \frac{2r_2^3}{3}\sin\theta_{tx} + L_2R^2 \Bigg) d\phi \\
+ \frac{1}{2}\int_{\phi_{2y}}^{\pi/2} \Bigg(\Bigg(& \left((y\csc\phi)^2 r_2 + y\csc\phi r_2^2 \cos\theta_{ty} + \frac{r_2^3}{3}\cos^2\theta_{ty} \right)\sin\theta_{ty} \\
& + r_2^2\left(y\csc\phi - r_2\cos\theta_{ty}\right)\theta_{ty} + \frac{2r_2^3}{3}\sin\theta_{ty} + L_2R^2 \Bigg) d\phi \\
= \int_0^{\phi_{2x}} V_{2x}\, d\phi + & \int_{\phi_{2y}}^{\pi/2} V_{2y} d\phi
\end{aligned}
\tag{4-78}
$$

d. Phases 1 and 2 Active Volume: The two volume integrals apply, however, for Phases 1 and 2 active, different integration limits apply as the volume integrals are added.

$$
\begin{aligned}
V_{12} = & \frac{1}{2}\int_{\phi_{2x}}^{\phi_{2y}} \left(s_1{}^2 r_1 + s_1 r_1{}^2 \frac{\pi}{2} + \frac{2}{3} r_1{}^3 + L_1R^2 \right) d\phi \\
& + \frac{1}{2}\int_0^{\phi_{2x}} \Bigg(\Bigg(\left((x\sec\phi)^2 r_2 + x\sec\phi r_2^2 \cos\theta_{tx} + \frac{r_2^3}{3}\cos^2\theta_{tx} \right)\sin\theta_{tx} \\
& \qquad + r_2^2\left(x\sec\phi - r_2\cos\theta_{tx}\right)\theta_{tx} + \frac{2r_2^3}{3}\sin\theta_{tx} + L_2R^2 \Bigg) d\phi \\
& + \frac{1}{2}\int_{\phi_{2y}}^{\pi/2} \Bigg(\Bigg(\left((y\csc\phi)^2 r_2 + y\csc\phi r_2^2 \cos\theta_{ty} + \frac{r_2^3}{3}\cos^2\theta_{ty} \right)\sin\theta_{ty} \\
& \qquad + r_2^2\left(y\csc\phi - r_2\cos\theta_{ty}\right)\theta_{ty} + \frac{2r_2^3}{3}\sin\theta_{ty} + L_2R^2 \Bigg) d\phi
\end{aligned}
\tag{4-79}
$$

In Equation (4-65), R substituted from Equation (4-1), r_1 from (4-7), s_1 from (4-6), and L_1 from (4-10), are all explicit functions of state variables and parameters determined independently of the variable of integration φ. Hence, the first integral of Equation (4-79) is evaluated explicitly by Equation (4-72). In contrast, r_2, L_2, angle θ_{tx} and angle

θ_{ty} depend on φ from Equations (4-20, 21, 22, and 23), but all are transcendental in θ_t and require numerical solution before integration.

e. Phases 2 and 3 Active Volume: The two volume integrals apply, however, for Phases 2 and 3 active, different integration limits apply as the volume integrals are added.

$$
\begin{aligned}
V_{23} = \frac{1}{2}\int_0^{\phi_{3x}} \Bigg(\Bigg(\Bigg((x\sec\phi)^2 r_2 + x\sec\phi r_2^2 \cos\theta_{tx} + \frac{r_2^3}{3}\cos^2\theta_{tx} \Bigg) \sin\theta_{tx} \\
+ r_2^2 \left(x\sec\phi - r_2\cos\theta_{tx} \right)\theta_{tx} + \frac{2r_2^3}{3}\sin\theta_{tx} + L_2R^2 \Bigg) d\phi \\
+ \frac{1}{2}\int_{\phi_{3y}}^{\pi/2} \Bigg(\Bigg(\Bigg((y\csc\phi)^2 r_2 + y\csc\phi r_2^2 \cos\theta_{ty} + \frac{r_2^3}{3}\cos^2\theta_{ty} \Bigg) \sin\theta_{ty} \\
+ r_2^2 \left(y\csc\phi - r_2\cos\theta_{ty} \right)\theta_{ty} + \frac{2r_2^3}{3}\sin\theta_{ty} + L_2R^2 \Bigg) d\phi \\
+ \frac{1}{2}\int_{\phi_{3x}}^{\phi_C} \left(\pi r_3^2 \left(x\sec\phi + r_3 \right) + L_3R^2 + (z - L_3)x^2\sec^2\phi \right) d\phi \\
+ \frac{1}{2}\int_{\phi_C}^{\phi_{3y}} \left(\pi r_3^2 \left(y\csc\phi + r_3 \right) + L_3R^2 + (z - L_3)y^2\csc^2\phi \right) d\phi
\end{aligned}
\tag{4-80}
$$

In Equation (4-80), R substituted from Equation (4-1), is an explicit function of state variables and parameters determined independently of the variable of integration φ. On the other hand, r_3 and L_3 depend on φ from Equations (4-14) and (4-15) which must be substituted before integration. Hence, the last two integrals are evaluated numerically by Equation (4-76). Likewise, r_2, L_2, angle θ_{tx} and angle θ_{ty} depend on φ from Equations (4-20, 21, 22, and 23), and all are transcendental in θ_t; hence they require numerical solution before integration.

E. Change in Volume and Partial Derivatives of Volume

The change in airbag volume with time, $\dot{V}$, required by Equation (3-57), can be calculated by summing the partial derivatives of V with respect to z, ε_H, and ε_L, and multiplying by $\dot{z}$, $\dot{\varepsilon}_H$, and $\dot{\varepsilon}_L$ respectively. The partial derivative of the total airbag volume is the sum of the partial derivatives for each phase of contact. Hence

$$\begin{aligned}\dot{V} = \dot{V}_1 + \dot{V}_2 + \dot{V}_3 = &\frac{\partial V_1}{\partial z}\dot{z} + \frac{\partial V_1}{\partial \varepsilon_H}\dot{\varepsilon}_H + \frac{\partial V_1}{\partial \varepsilon_L}\dot{\varepsilon}_L \\ &+ \frac{\partial V_2}{\partial z}\dot{z} + \frac{\partial V_2}{\partial \varepsilon_H}\dot{\varepsilon}_H + \frac{\partial V_2}{\partial \varepsilon_L}\dot{\varepsilon}_L \\ &+ \frac{\partial V_3}{\partial z}\dot{z} + \frac{\partial V_3}{\partial \varepsilon_H}\dot{\varepsilon}_H + \frac{\partial V_3}{\partial \varepsilon_L}\dot{\varepsilon}_L\end{aligned} \tag{4-81}$$

1. Phase 1 Airbag Volume Partial Derivatives.

The Phase 1 airbag volume was integrable, thus a partial derivative can be taken on this solution. These partial derivatives require substantial calculus when expressed in analytic form, which can be found in Appendix A for Phase 1 impact. Numeric differentiation is a more practical approach that is implemented in code. All the partial derivatives appearing in the following equations will be calculated numerically by complex step finite difference [Ref. 4-1 Martins]. Differentiating Equation (4-72) yields

$$V_1' = \left[\frac{1}{2}\left(s_1^2 r_1 + s_1 r_1^2 \frac{\pi}{2} + r_1^3 + L_1 R^2\right)\left(\phi_{2y} - \phi_{2x}\right)\right]' \tag{4-82}$$

where $(\cdot)'$ indicates partial differentiation with respect to z, ε_H, and ε_L, in turn.

2. Phase 3 Airbag Volume Partial Derivatives.

The Phase 3 airbag volume was integrated by numeric quadrature. Semi-analytic differentiation can be taken using Leibniz' rule on this solution. Differentiating Equation (4-76) yields

$$V_3' = \int_{\phi_{3x}}^{\phi_C} V_{3x}'\, d\phi + \int_{\phi_C}^{\phi_{3y}} V_{3y}'\, d\phi - \phi_{3x}' V_{3x}\big|_{\phi=\phi_{3x}} + \phi_{3y}' V_{3y}\big|_{\phi=\phi_{3y}} \tag{4-83}$$

Numeric differentiation is performed on each partial derivative of Equation (4-83) by complex step.

3. Phase 2 Airbag Volume Partial Derivatives.

The Phase 2 airbag volume contains a transcendental equation requiring numerical integration. The geometric partial derivative will be handled numerically by complex step finite difference. Leibniz' Rule is applied to the V_2 integrals in Equation (4-78) to express its derivative as the numeric integration of the integrand's derivative plus the integrand times the derivative of the limits of integration. The volume derivative is split into two parts because of the discontinuity of the volume equations between phases. Thus, after applying the Leibniz rule, Equation (4-78) becomes a continuous, semi-analytic expression for which each of the derivatives of the parenthetical expressions are found by complex step finite difference.

$$V_2' = \int_{0}^{\phi_x} V_{2x}'\, d\phi + \int_{\phi_y}^{\pi/2} V_{2y}'\, d\phi + \phi_x' V_{2x}\big|_{\phi=\phi_x} - \phi_y' V_{2y}\big|_{\phi=\phi_y} \tag{4-84}$$

The limits of integration can be ϕ_{2x} and ϕ_{2y} or ϕ_{3x} and ϕ_{3y} depending whether Phase 1 or 3 co-exists with Phase 2.

Unfortunately, the non-linear equation solver that numerically calculates the root of Equation (4-19) for θ_t does not handle complex variables. Therefore, all partial derivatives of θ_t appearing in Equation (4-84) must be found semi-analytically by differentiating Equation (4-19) explicitly.

$$\theta_t' = \frac{\left[C' - z'\right](1-\cos\theta_t) + \left(\sin\theta_t - \theta_t\right)R'}{\left(R - s_2\right)(1-\cos\theta_t) + \left[s_2 + z - C\right]\sin\theta_t} \tag{4-85}$$

The partial derivatives on the right hand side of Equation (4-85) are found by complex step.

F. Summary

Kinematic equations for airbag surface area and volume were derived in this chapter in terms of a limited number of geometric variables. Identifying distinct phases of impact and appropriate assumptions about their geometry was critical to creating a tractable problem. Discovering the conditions that delineated the phases and recognizing how phases may coexist were important steps in the formulation.

As a result of identifying explicitly the discontinuities in the kinematic equations, numerical simulations were implemented that accounted for the piecewise smooth nature of the solution. Because the area and volume integrations are imbedded within the numeric time integration of differential equations derived in Chapter 3, derivatives of these spatial integrals with respect to the state variables were required. Tedious but straight-forward calculus with the aid of Leibniz' Rule provided the partial derivatives needed for complex-step derivatives used in the computational solution. The end result is a single, sophisticated, uniform-strain finite element, governed by six degrees of freedom

(L, R, r, s, z, θ), which has the potential to rival finite element models comprised of hundreds or thousands of simple elements.

Chapter V: Airbag Elasticity and Permeability Experiments

After an overview of the airbag properties that were measured, the experimental apparatus is described. The experimental design and procedure are explained. The analyses and experimental results are separated into two sections: one for elasticity and the other for permeability.

A. Overview

Our mathematical models use airbag permeability in the form of airbag leak rate R_L and airbag elasticity in the hoop direction E_H and in the longitudinal direction E_L. Airbag leak rate and hoop elasticity were experimentally measured for eight of the nine airbags. Longitudinal elasticity was not measured and was assumed equal to the hoop elasticity, as is typical of the fabric manufacturer's grab tensile data. These experiments were dangerous; more than a 3 psig over-pressure from an airbag burst could kill an experimenter. Precautions were taken to shield the experimenters from the test.

B. Experimental Apparatus

The experimental apparatus consisted of three main elements: 1) the airbag with flange, 2) the hose, pipe, fittings, and pressure regulator connected to the 3-inch diameter air compressor pipe, 3) the measuring tape and sleeves around the airbag and the pitot tube, pressure sensors, temperature sensor, and data-logger.

1. Airbag and Flange.

The airbag and flange consisted of the airbag attached to its 2-foot by 4-foot by ¾ inch plywood flange used in the drop experiments. The flange was mounted on two saw horses with the airbag facing upwards. See Figure 5-1 for this configuration. Figure 5-2 shows a photograph of the configuration.

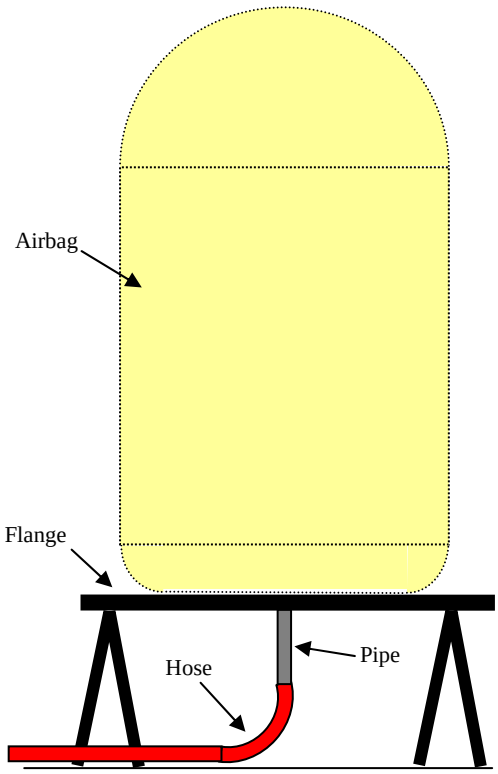

Figure 5-1: Airbag and Flange

There was an eighth-inch thick aluminum door that covered 4-inch by 6-inch holes in the flange that connect the airbag to an air jet fill source during collision experiments. This door was closed for the permeability and elasticity test and held shut by a 30 lb weight seen hanging in Figure 5-2. This door was sealed against the flange by 3/8 by ½ inch foam seals (typical weather-stripping). These seals often blew out at higher test

Figure 5-2: Photograph of Airbag and Flange

pressures, allowing air to escape through the seals. The white paper strips on the edge of the flange would blow and flap when a seal burst, indicating bad permeability data. Given the high ambient noise level during the tests and subtlety in the pressure readings, the paper flags were the best seal break indicators.

2. Hose, Pipe, Fittings, and Pressure Regulator.

The 1-inch diameter hose, pipe, fittings, and pressure regulator, all rated for 200 psig and above, connected the airbag and flange to a 3-inch diameter compressed air pipe pressurized at 157 psig. The flange pipe was approximately 1-foot long and attached to the 20-foot long red hose with a threaded union as shown in Figures 5-1 and 5-2. The fittings included a 1-inch diameter ball valve just downstream of the pressure regulator to control the start and stop of experiments. The pressure regulator was adjusted for each experiment to give a downstream pressure high enough to give sufficient flow rate in the hose and pipe to achieve a given pressure in the airbag. Figure 5-3 shows a photograph including the ball valve, hose, and fittings.

Figure 5-3: Hose, Valve, and Fittings

3. Measuring Tape, Pitot Tube, Pressure Sensors, Temperature Sensor, and Data-Logger.

The hoop elasticity of the airbag was calculated from changes in diameter with pressure as indicated by electronic pressure sensors and changes in airbag circumference

measured by the tape measure shown in the photograph in Figure 5-2. One end of the tape measure was sewn to the airbag as a reference point. The rest of the tape was supported at the proper height by black thread "belt-loops". A sleeve at the secured end of the tape supported the loose end of the tape and provided a reading line. This line was read by a small telescope from a safe distance.

A pitot tube was installed in the pipe attached to the flange door about 2 inches from the discharge end. Wooden blocks with foam seals supported the Pitot tube to keep its tip in the center of the pipe and oriented to catch a good stagnation pressure reading. One pressure sensor read the stagnation pressure from the tip of the Pitot tube, and the other read the static pressure from the side port on the Pitot tube. The air stream velocity was calculated from these two pressure readings. Two additional pressure sensors at low air velocity spots inside the airbag measured the airbag static pressure. All these pressures were fed into the data-logger, a laptop computer running LabView 7 [5-1] software shown in Figure 5-3. The pressure data was noise filtered by averaging the 4,000 data points.

Temperature inside the airbag was measured by a thermocouple in a low air velocity location. The thermocouple had a digital readout with a large LED display. The black readout box is shown near the experimenter's foot in Figure 5-2.

C. Experimental Design and Procedure

The experiments consisted of first barely inflating an airbag to get a baseline circumference and permeability, then raising the regulator pressure slightly to get a higher flow rate and airbag pressure. It took 5 to 10 minutes for the airbag temperature

and circumference to come to equilibrium, before pressure, flow rate, and temperature measurements were taken. The pressure and flow rate sensors took 4 seconds of data at one millisecond intervals. Each reading was averaged over the 4 second interval. The experimenters recorded the digital thermometer reading manually. Eight to ten readings were taken per airbag, up to approximately 3 psig. of fill pressure.

After each airbag experiment, the fill pipe was disconnected from the airbag flange door, the tape measure unthreaded, sensors detached, and the airbag with flange removed from the saw horses. The next airbag was then mounted on the saw horses and rigged for testing. Eight of the nine original airbags were tested for permeability and elasticity after completion of the drop testing. The ninth airbag exploded during one of the higher and heavier drop tests, and therefore was not available for permeability and elasticity testing.

D. Elasticity Analysis and Experimental Results

1. Analysis.

The elasticity results show the airbag circumference varying with pressure. The linearization of this variation is indicated by an x, y relationship with an initial offset in Figures 5-4 to 5-12. The hoop strain was calculated from the measured change in airbag circumference divided by the unstrained circumference c_0. Elastic modulus is a function of the applied hoop and longitudinal stresses and resulting strains. A constitutive stress-strain equation shows the relationship to elastic modulus.

$$\frac{c - c_0}{c_0} = \varepsilon_H = \frac{\sigma_H}{E_H} - \frac{\nu_L}{E_L}\sigma_L \qquad (5\text{-}1)$$

where c_0 is the initial airbag circumference, $c - c_0$ is the strained circumferential displacement, and ν_L is the longitudinal Poisson ratio. The hoop stress was calculated from the airbag pressure, strained radius, and nominal fabric thickness. The longitudinal stress in a cylinder is half the hoop stress [5-2]. Thus

$$\sigma_L = \frac{\sigma_H}{2} = \frac{P_g R}{2t} = \frac{P_g R_0}{2t}\left(1+\varepsilon_H\right) \tag{5-2}$$

where t is airbag fabric thickness. From Ref [3-3: p17], $\nu_H / E_H = \nu_L / E_L$. Therefore, substituting (5-2) into (5-1) yields

$$\varepsilon_H = \frac{P_g R_0}{E_H t}\left(1-\frac{\nu_H}{2}\right)\left(1+\varepsilon_H\right) \tag{5-3}$$

$E_H t$ was calculated from the measurements. Let the effective modulus be

$$Et \equiv \frac{E_H t}{1-\frac{\nu_H}{2}} \tag{5-4}$$

Hence, substituting (5-4) into (5-3) and solving for hoop strain yields

$$\varepsilon_H = \frac{\frac{P_g R_0}{Et}}{1-\frac{P_g R_0}{Et}} = \frac{P_g R_0}{Et - P_g R_0} \tag{5-5}$$

Recalling the definition of hoop strain given by Equation (5-1) in terms of the measured circumference, where $c_0 = 2\pi R_0$, these equations lead to

$$c = c_0 + c_0\left(\frac{P_g R_0}{Et - P_g R_0}\right) = 2\pi R_0\left[1+\frac{P_g R_0}{Et - P_g R_0}\right] \tag{5-6}$$

Equation (5-6) shows that the measured circumference is a nonlinear function of gauge pressure. However, it is a weakly nonlinear function, because the pressure term in the denominator of (5-6) is small compared to the effective modulus, *Et.* Hence, the

statistical proportion of explained variation (R^2) above 0.9 is quite high for the linear curve fit shown in Figures 5-5 through 5-12. Regression of a least squares fit of the nonlinear model of Equation (5-6) to the data provides estimates of the two parameters R_0 and Et. Table 5-1 shows the resulting R_0 and Et for each airbag found by the nonlinear least squares regression of Equation (5-6).

Table 5-1: *Et* Values for Each Airbag

Airbag	c_0	R_0	Et
3060	95.91	15.26	944
3072	95.52	15.20	1007
3084	95.94	15.27	1098
3660	113.29	18.03	1055
3672	112.89	17.97	1071
3684	112.79	17.95	1064
4072	128.96	20.52	1181
4084	129.04	20.54	1108

The measured nominal fabric thickness for all airbags was t = 0.012 inch. A sample nonlinear curve fit for airbag 4084, found from regression of Equation (5-6) and shown in Figure 5-4, does not differ significantly from Figure 5-18. The variation in effective modulus of elasticity could be explained by seams.

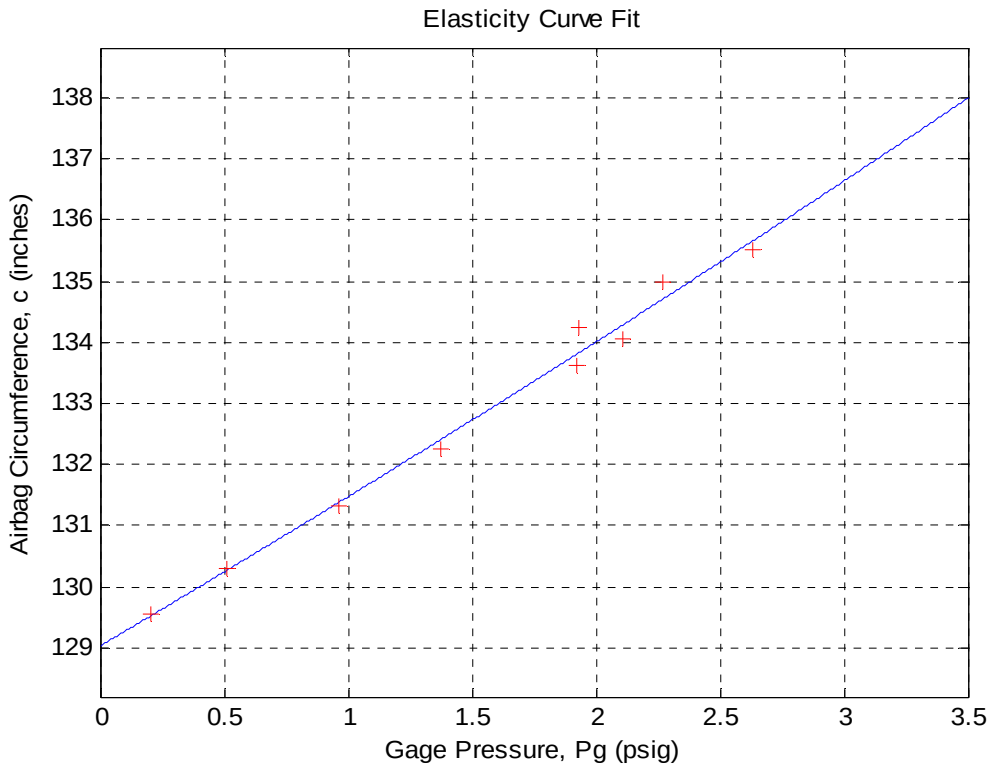

Figure 5-4: Elasticity Curve Fit for Airbag 4084

2. Experimental Results.

The elasticity experimental results are shown in Figures 5-5 to 5-12 with labels to indicate each airbag. The elasticity results show the airbag circumference variation with airbag pressure. The linearity of the results was remarkable. A straight line fit each result with a regression R-squared of better than 0.9. The airbags are named according to their nominal inch dimensions with two-digit diameter first followed by two-digit height.

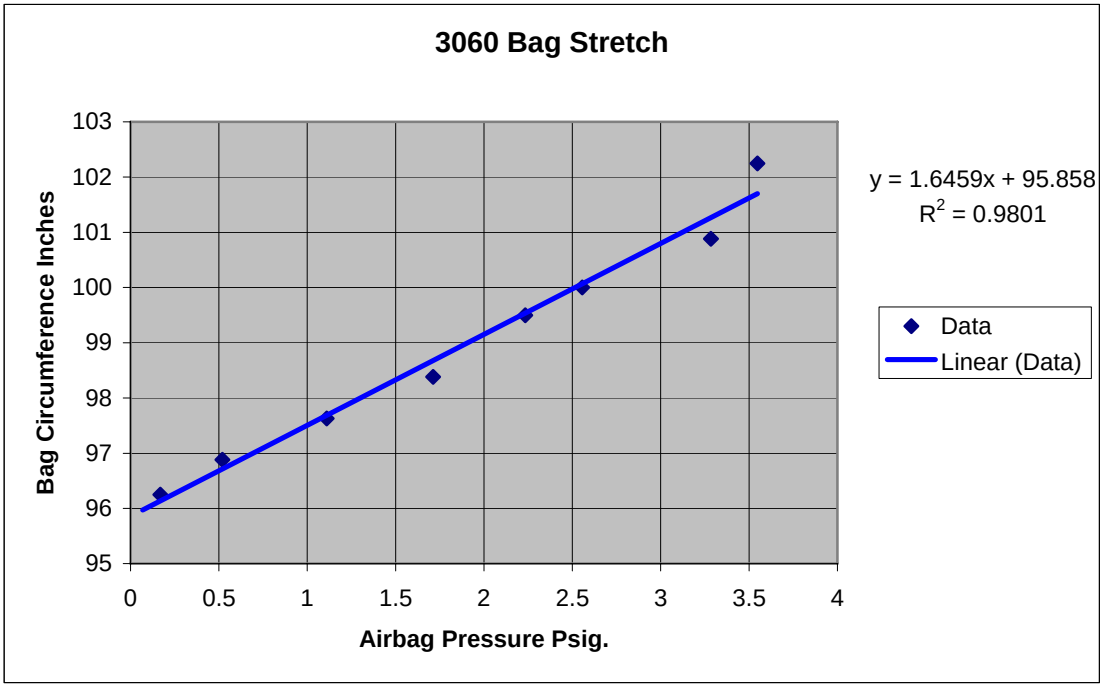

Figure 5-5: Elasticity Results for the Nominal 3060 Airbag

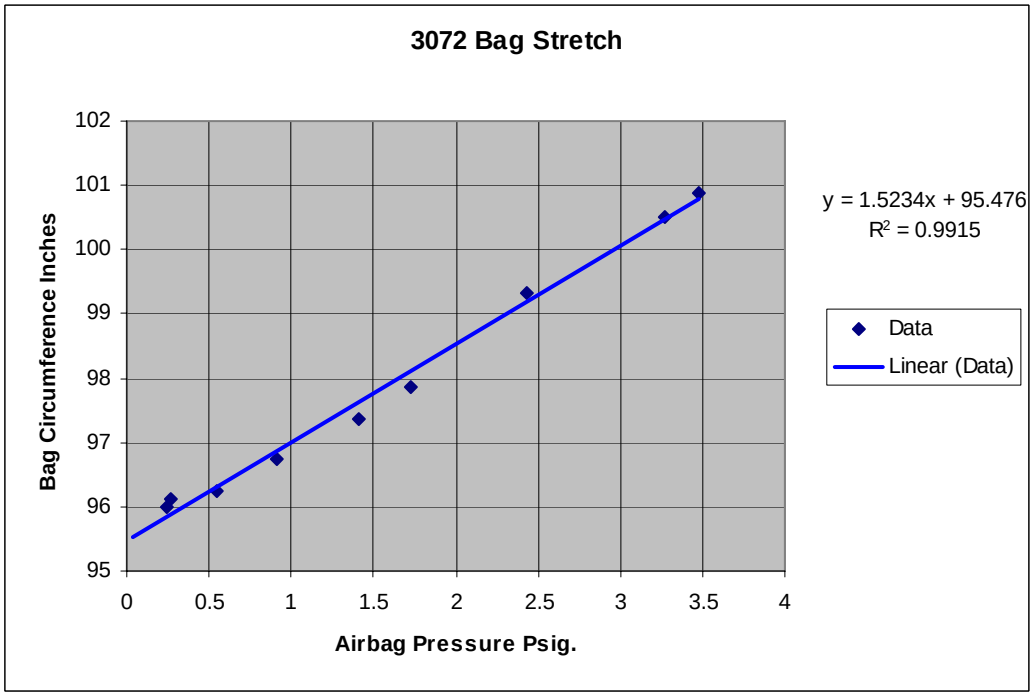

Figure 5-6: Elasticity Results for the Nominal 3072 Airbag

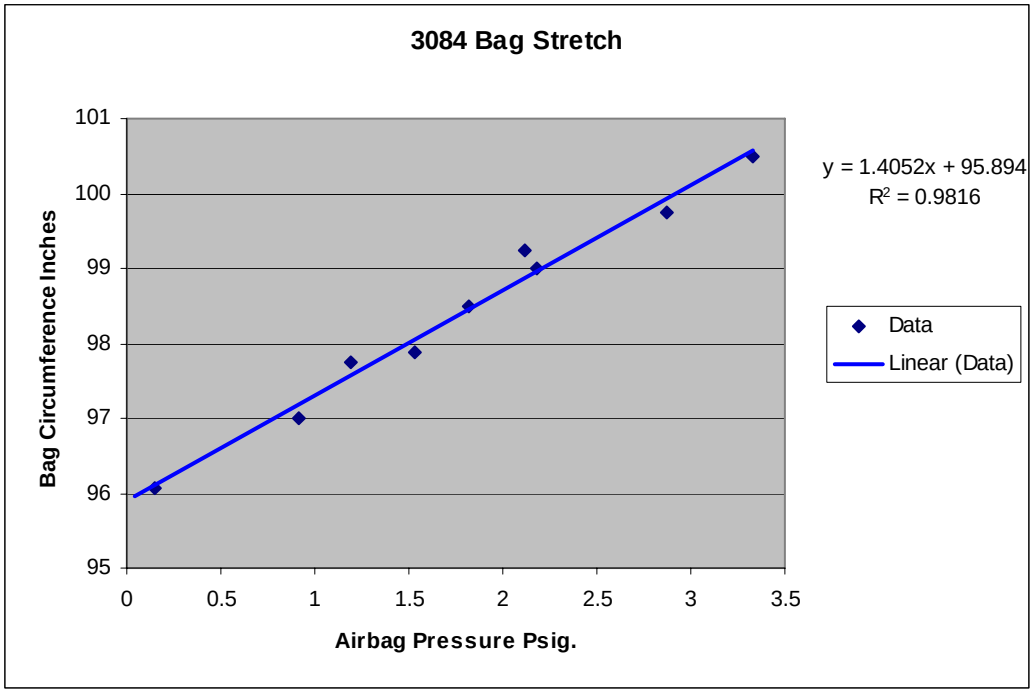

Figure 5-7: Elasticity Results for the Nominal 3084 Airbag

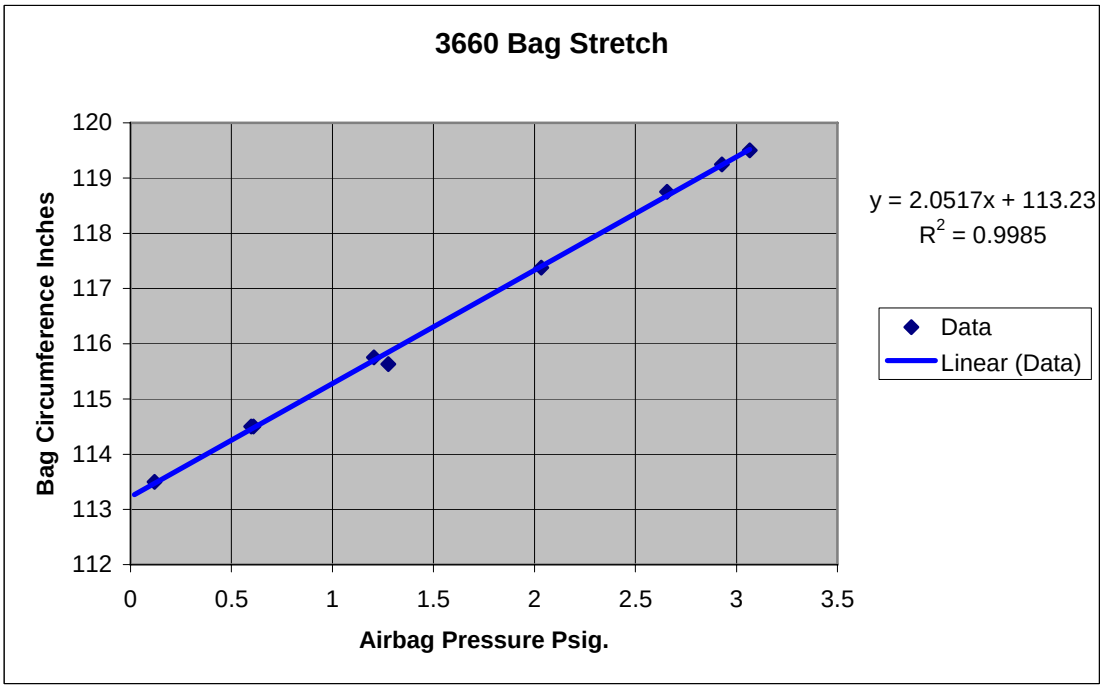

Figure 5-8: Elasticity Results for the Nominal 3660 Airbag

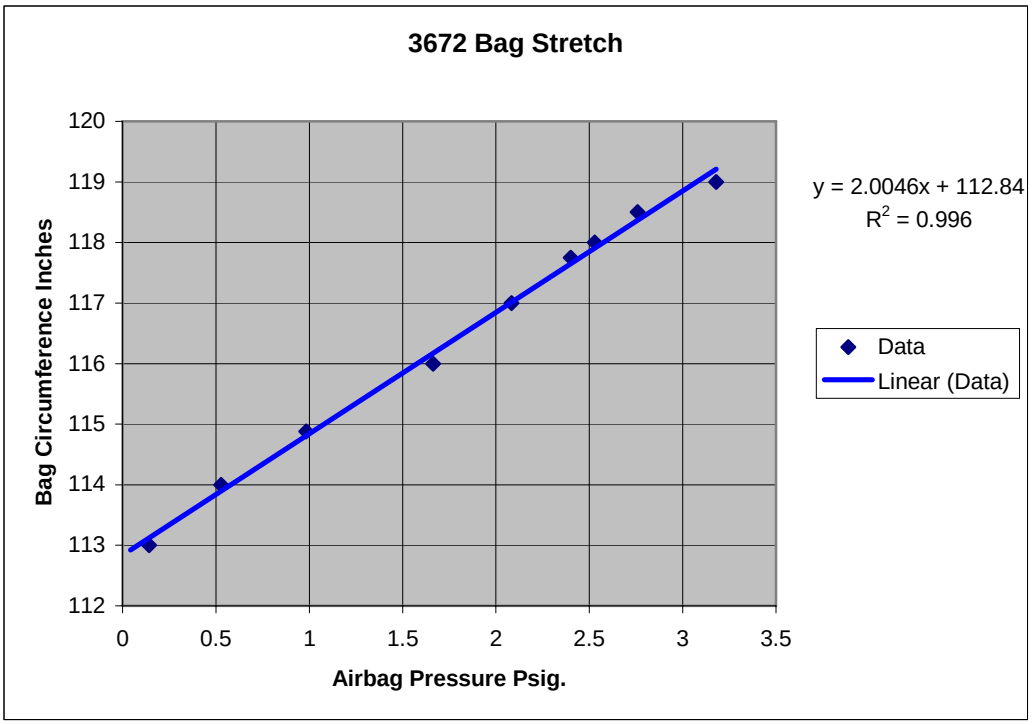

Figure 5-9: Elasticity Results for the Nominal 3672 Airbag

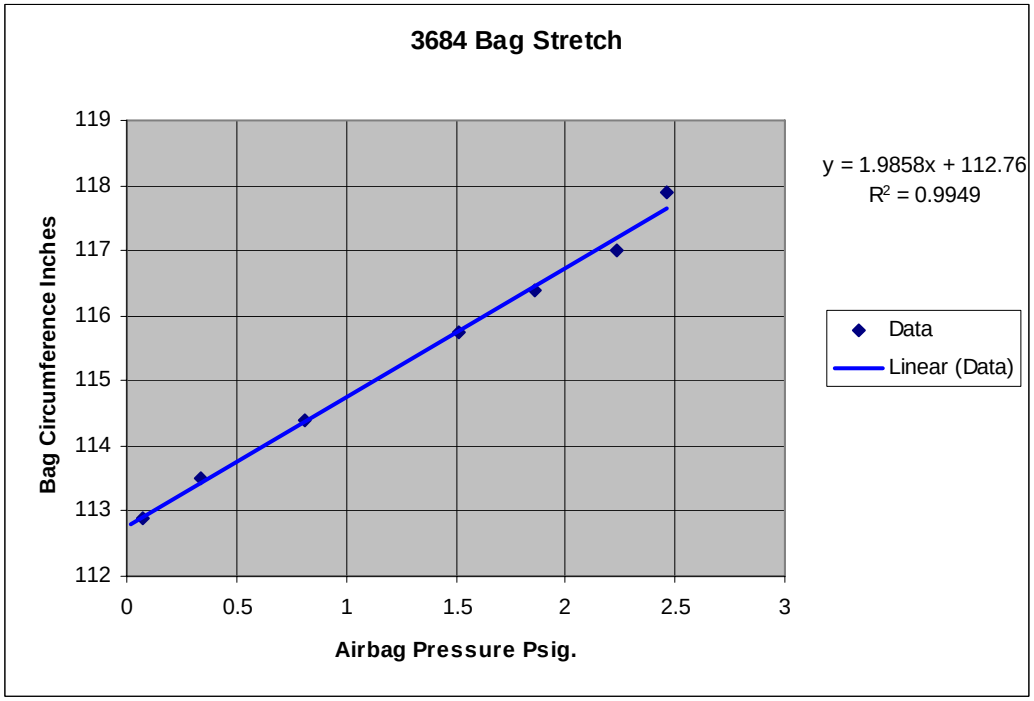

Figure 5-10: Elasticity Results for the Nominal 3684 Airbag

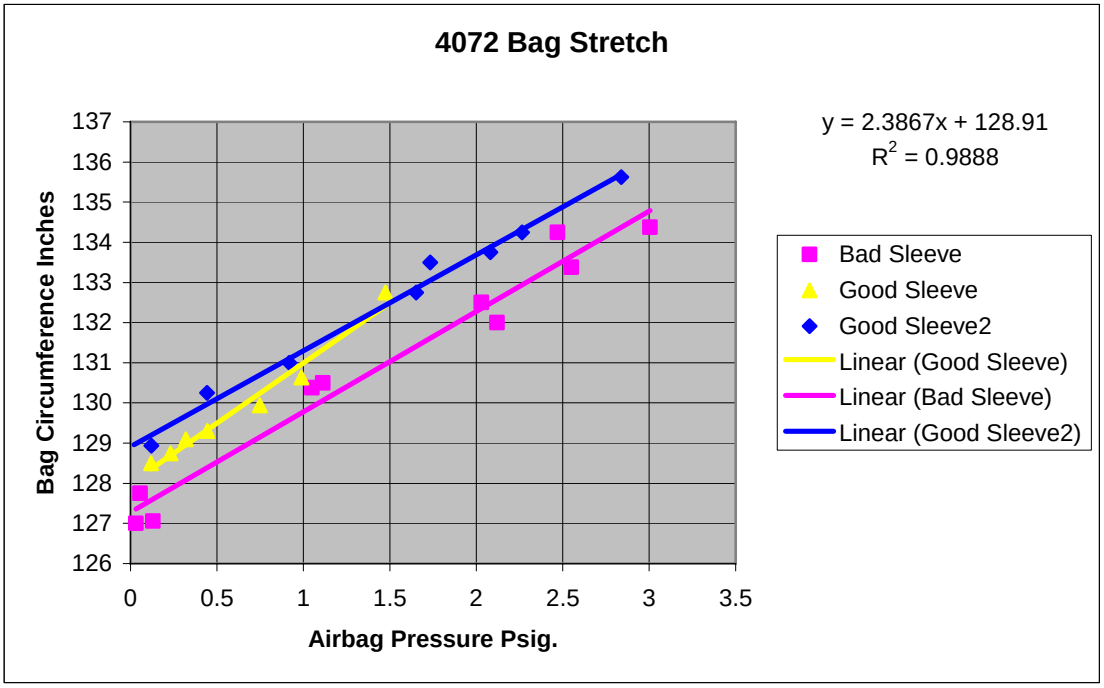

Figure 5-11: Elasticity Results for the Nominal 4072 Airbag

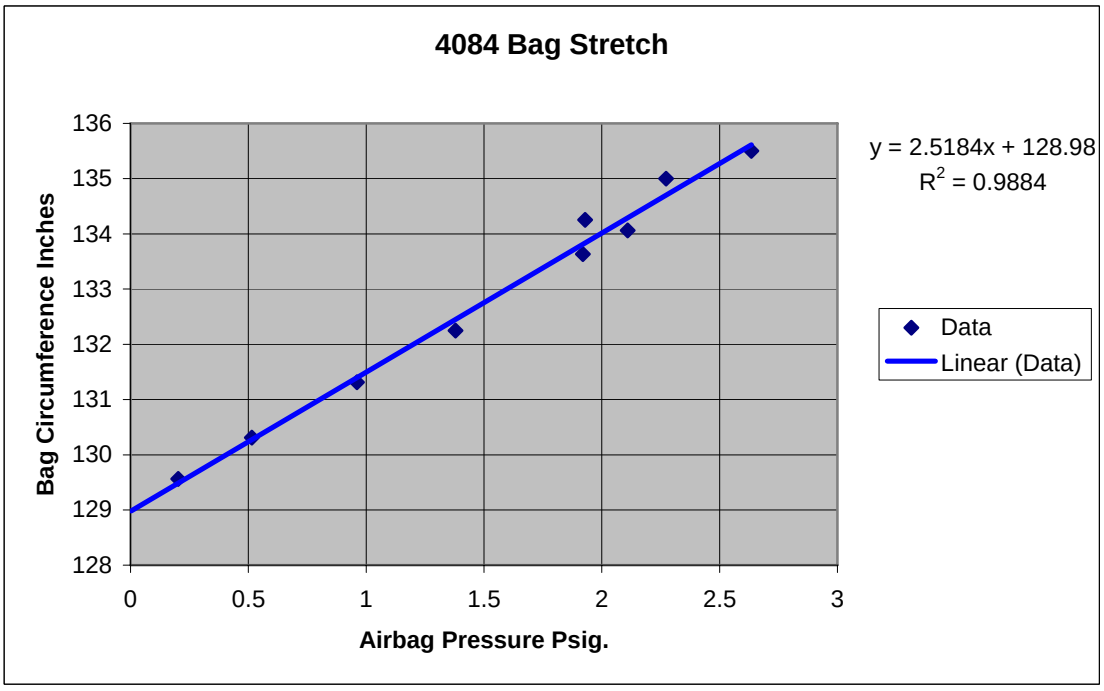

Figure 5-12: Elasticity Results for the Nominal 4084 Airbag

Airbag 4072 was the first airbag tested for elasticity and permeability. Initially, the sleeve for the tape measure grabbed the tape and stretched, giving inaccurate readings as noted in the figure. Figure 5-11 shows the elastic results for the nominal 4072 airbag. The sleeve was redesigned to be snag-free. Likewise, the seals kept blowing out at low pressure, causing inaccurate readings as seen in the figure. A 30-lb weight was hung on the door to crush the seals tight to solve this problem.

E. Permeability Analysis and Experimental Results

1. Analysis.

The permeability measurements were based an airbag pressure and an air mass flow rate into the airbag via the 1-inch diameter pipe. The air mass flow rate was measured with a Pitot tube mounted in the air pipe 2 inches from the discharge end. Because the static and stagnation pressure inlets are so close together on a Pitot tube, there is not enough distance for significant viscous energy losses; hence isentropic flow assumptions apply. The compressible isentropic gas mass flow rate in a pipe $\dot{m}$ from [3-2: pg 97] is

$$\dot{m} = P_0 A \sqrt{\frac{\gamma}{RT_0}} \frac{M}{\left(1+\frac{\gamma-1}{2}M^2\right)^{(\gamma+1)/[2(\gamma-1)]}} \tag{5-7}$$

where

P_0 = Pitot stagnation pressure in lbf/sqin

A = 1.060 inch diameter pipe cross sectional area = 0.88247 sqin

γ = Specific heat ratio, 1.4 for air at 60 ^{o}F, (our case) [5-2: pg 844]

T_0 = Pitot stagnation temperature also = airbag quiescent temperature

M = Mach number at Pitot tube

The Ideal Gas Constant is calculated from that given by [5-2: pg 884 and inside front cover].

$$R = 0.3704\frac{psia\ ft^3}{lbm\ ^oR} = 0.3704\frac{slug\ ft^4 144 in^2/ft^2}{s^2 in^2 lbm\ ^oR}$$
$$= 53.3376\frac{slug\ ft^2 32.174 lbm/slug}{s^2 lbm\ ^oR} = 1716.1\frac{ft^2}{s^2\ ^oR} = 247{,}118.4\ \frac{in^2}{s^2\ ^oR} \quad (5\text{-}8)$$

The Mach number M for compressible isentropic gas mass flow from [3-2: pg 92] is

$$M = \sqrt{\frac{2}{\gamma - 1}\left(\frac{P_0}{P}\right)^{(\gamma-1)/\gamma} - \frac{2}{\gamma - 1}} \quad (5\text{-}9)$$

where P is the static pressure in the Pitot tube. Equations (5-7) and (5-9) were used in conjunction with the measured static and stagnation pressure and temperature to arrive at an experimentally determined mass flow rate given in Tables 5-2 through 5-10 for each airbag. The higher speed Pitot readings during the experiments indicated supersonic velocities. Because of falling density at higher Mach numbers, these supersonic velocities should have lowered the mass flow rate and hence airbag pressure, but the opposite happened. This type of high speed compressible flow with friction is called Fanno flow, which typically tends toward Mach 1 when the pipe is long enough. Therefore, when the pressure data indicated supersonic flow, the Mach number was set to one.

2. Experimental Results.

The permeability results show pounds mass of air that leak out of the airbag per second as a function of airbag pressure P_g. These results are shown in Tables 5-2 through 5-10 and Figures 5-13 through 5-20 following. All pressures are in psig, temperature is

in degrees Rankine, and $\dot{m}$ in lbm/second. A column for gauge pressure in the airbag is included in the table for later use in Equation (5-10).

Table 5-2: Airbag 3060 Permeability Test Data

Airbag	P_g	P_0-P_{atm}	P-P_{atm}	T_0	M	$\dot{m}$
3060	0.1678	0.2434	-0.104	532.6	0.1837	0.0945
	0.5197	1.1014	-0.505	531.7	0.3944	0.1999
	1.1105	2.6456	-1.259	531.4	0.6148	0.3014
	1.7124	4.577	-2.247	530.8	0.8155	0.3804
	2.2325	5.9655	-2.961	531.5	0.9365	0.4191
	2.5558	6.9249	-3.466	531.5	1	0.4401
	3.2839	9.3271	-4.718	532.5	1	0.4886
	3.547	10.989	-5.767	532.5	1	0.5224

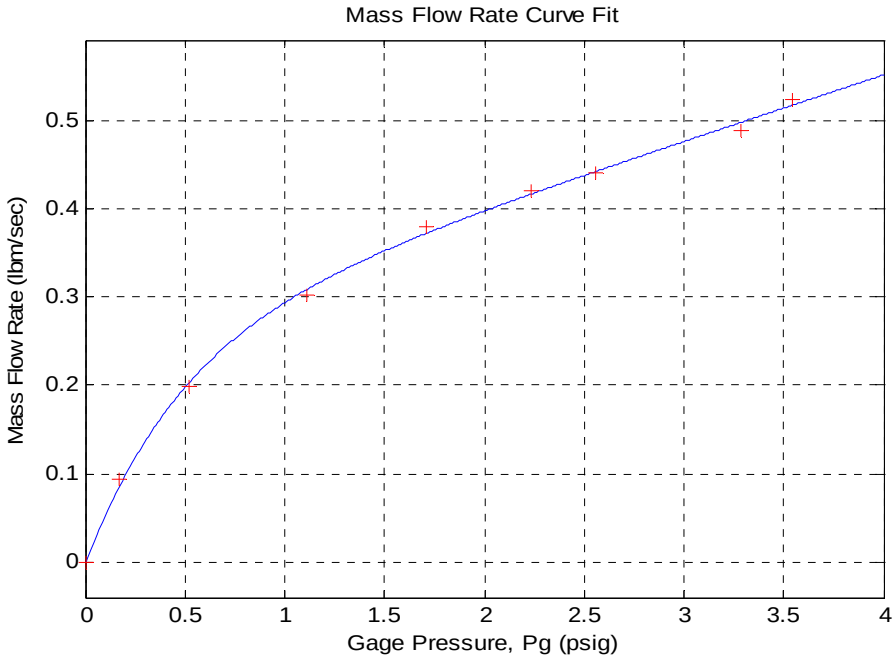

Figure 5-13: Permeability Results for the Nominal 3060 Airbag

Table 5-3: Airbag 3072 Permeability Test Data

Airbag	P_g	P_0-P_{atm}	P-P_{atm}	T_0	M	$\dot{m}$
3072	0.2409	0.3025	-0.134	536.4	0.2058	0.1054
	0.5448	1.0354	-0.484	536.2	0.3837	0.1938
	0.9159	2.0541	-0.995	535.9	0.5435	0.2685
	1.4139	3.4271	-1.722	536.1	0.7078	0.3374
	1.7247	4.4467	-2.312	536	0.8139	0.3757
	0.2703	0.3099	-0.135	531.6	0.2078	0.1069
	2.4346	6.3893	-3.334	531.2	0.9829	0.4292
	3.2691	9.1414	-4.981	532.7	1	0.4847
	3.4781	9.9965	-5.524	534.7	1	0.5011

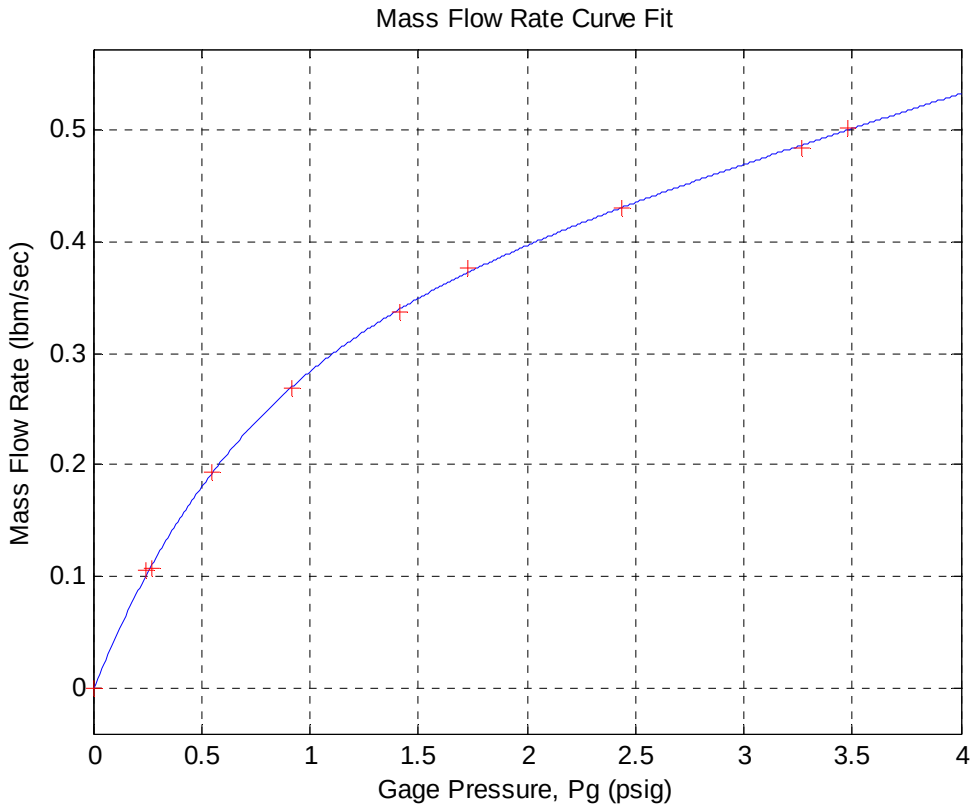

Figure 5-14: Permeability Results for the Nominal 3072 Airbag

Table 5-4: Airbag 3084 Permeability Test Data

Airbag	P_g	P_0-P_{atm}	P-P_{atm}	T_0	M	$\dot{m}$
3084	0.1466	0.2507	-0.107	532.7	0.1865	0.0959
	0.9178	2.5159	-1.151	531.7	0.5952	0.2934
	1.5347	4.6167	-2.15	531.2	0.8099	0.3802
	1.1901	3.4329	-1.608	531.4	0.6984	0.3369
	1.8218	5.6793	-2.722	531.2	0.9056	0.4116
	2.1795	7.0708	-3.426	531.6	1	0.4431
	2.1217	6.7801	-3.264	531.6	0.9935	0.4371
	2.8736	9.7936	-4.779	532.5	1	0.4981
	3.3269	11.824	-5.813	534.3	1	0.5384

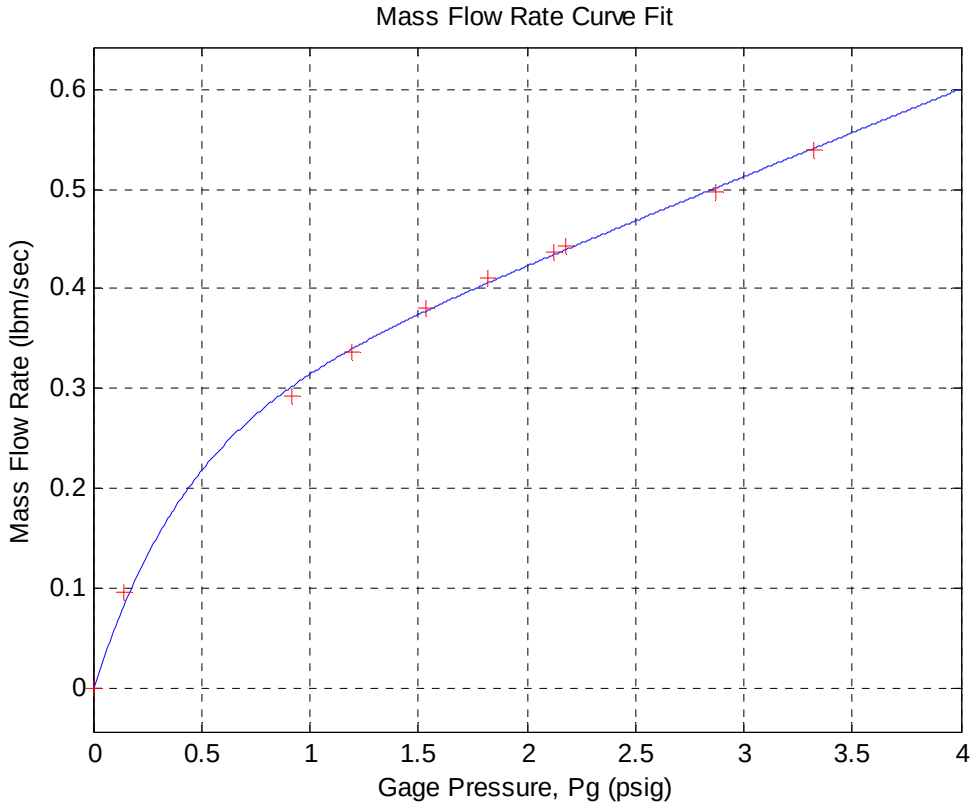

Figure 5-15: Permeability Results for the Nominal 3084 Airbag

Table 5-5: Airbag 3660 Permeability Test Data

Airbag	P_g	P_0-P_{atm}	P-P_{atm}	T_0	M	$\dot{m}$
3660	0.118558	0.190905	-0.08306	536.2	0.1631	0.0837
	0.596993	1.944764	-0.93581	536.3	0.5282	0.2615
	1.204808	4.995017	-2.50686	536.7	0.8569	0.3916
	0.608294	2.073749	-1.00222	536	0.5459	0.2695
	1.276136	5.027064	-2.54236	538.2	0.8613	0.3921
	2.033754	8.084599	-4.1721	536.5	1	0.4616
	2.656308	10.69878	-5.56284	537.4	1	0.5141
	2.926886	11.9694	-6.35183	537	1	0.54
	3.066346	13.48776	-7.31269	537	1	0.5708

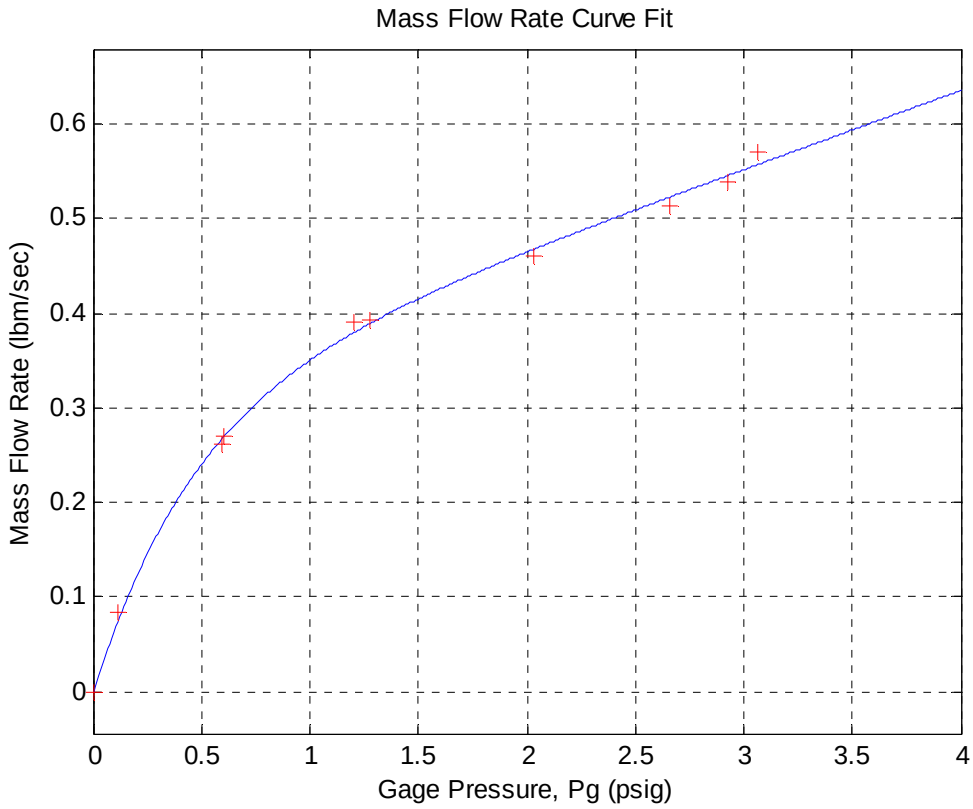

Figure 5-16: Permeability Results for the Nominal 3660 Airbag

Table 5-6: Airbag 3672 Permeability Test Data

Airbag	P_g	P_0-P_{atm}	P-P_{atm}	T_0	M	$\dot{m}$
3672	0.143408	0.269906	-0.12513	536	0.1959	0.1003
	0.527072	2.143781	-1.06447	535.8	0.5579	0.2746
	0.983843	4.320477	-2.23702	536.1	0.8013	0.3714
	1.66362	7.845008	-4.10299	536.4	1	0.4568
	2.083777	10.17792	-5.34957	536.7	1	0.5039
	2.395435	12.00603	-6.46064	537.9	1	0.5403
	2.52829	12.92083	-6.96462	538.7	1	0.5584
	2.758543	14.54457	-7.86724	539.7	1	0.5907
	3.178513	17.78964	-9.03565	539.8	1	0.6562

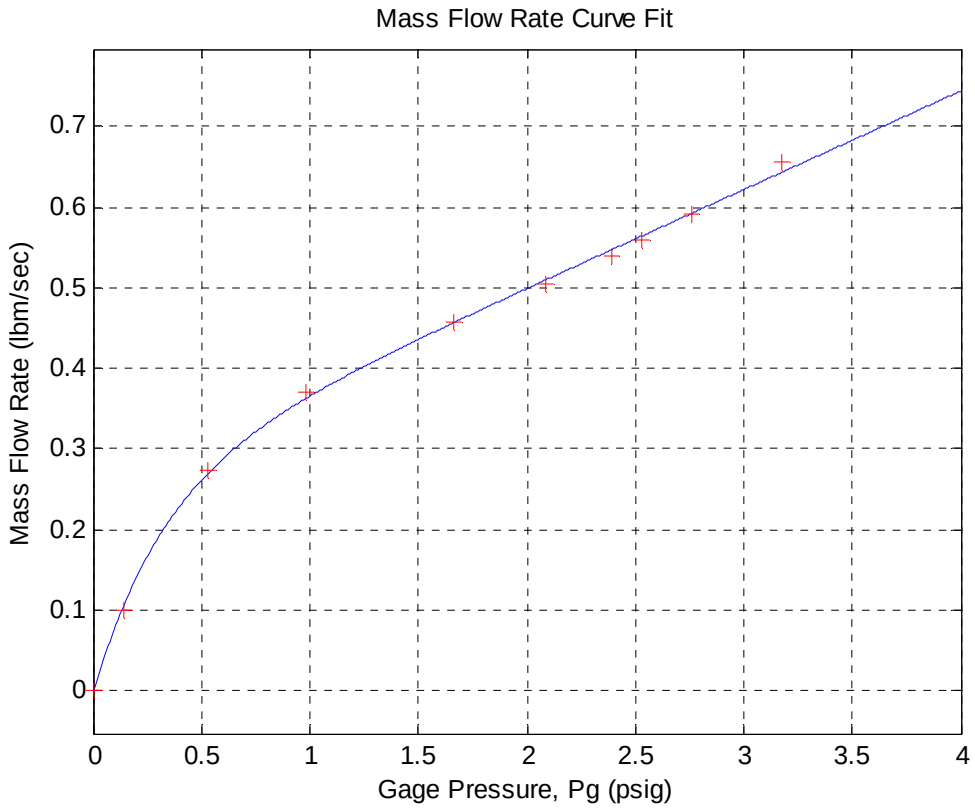

Figure 5-17: Permeability Results for the Nominal 3672 Airbag

Table 5-7: Airbag 3684 Permeability Test Data

Airbag	P_g	P_0-P_{atm}	P-P_{atm}	T_0	M	$\dot{m}$
3684	0.069648	0.135634	-0.0621	536.2	0.1386	0.0712
	0.338996	1.281372	-0.6102	535.3	0.4281	0.2152
	0.809485	3.904036	-1.90549	535.2	0.7514	0.3554
	1.510362	7.648819	-3.8578	535.3	1	0.4532
	1.856347	9.555015	-4.82909	535.7	1	0.4917
	2.236534	11.69528	-5.94024	536.5	1	0.5347
	2.458902	13.0903	-6.7146	537	1	0.5627

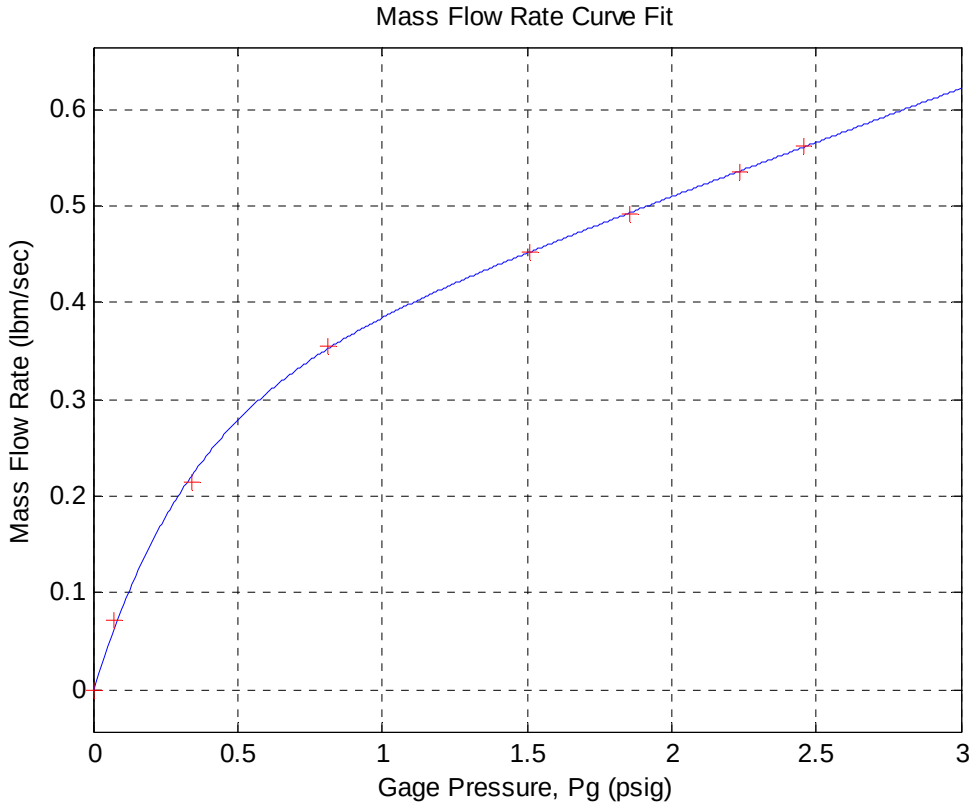

Figure 5-18: Permeability Results for the Nominal 3684 Airbag

Table 5-8: Airbag 4072 Permeability Test Data

Airbag	P_g	P_0-P_{atm}	P-P_{atm}	T_0	M	$\dot{m}$
4072	0.443349	0.792348	-0.50928	530.8	0.3564	0.1802
	0.917938	1.652874	-1.22084	530.8	0.5328	0.2598
	1.652292	3.015175	-2.44333	531.5	0.745	0.3385
	2.080483	3.796636	-3.31	532.4	0.8621	0.3697
	0.120347	0.1566	-0.07878	532.5	0.1512	0.0779
	1.733361	3.112925	-2.39549	531.3	0.7467	0.3407
	2.2642	4.033528	-3.54219	531.7	0.8934	0.3774
	2.839139	5.043936	-4.99159	532.1	1	0.4016

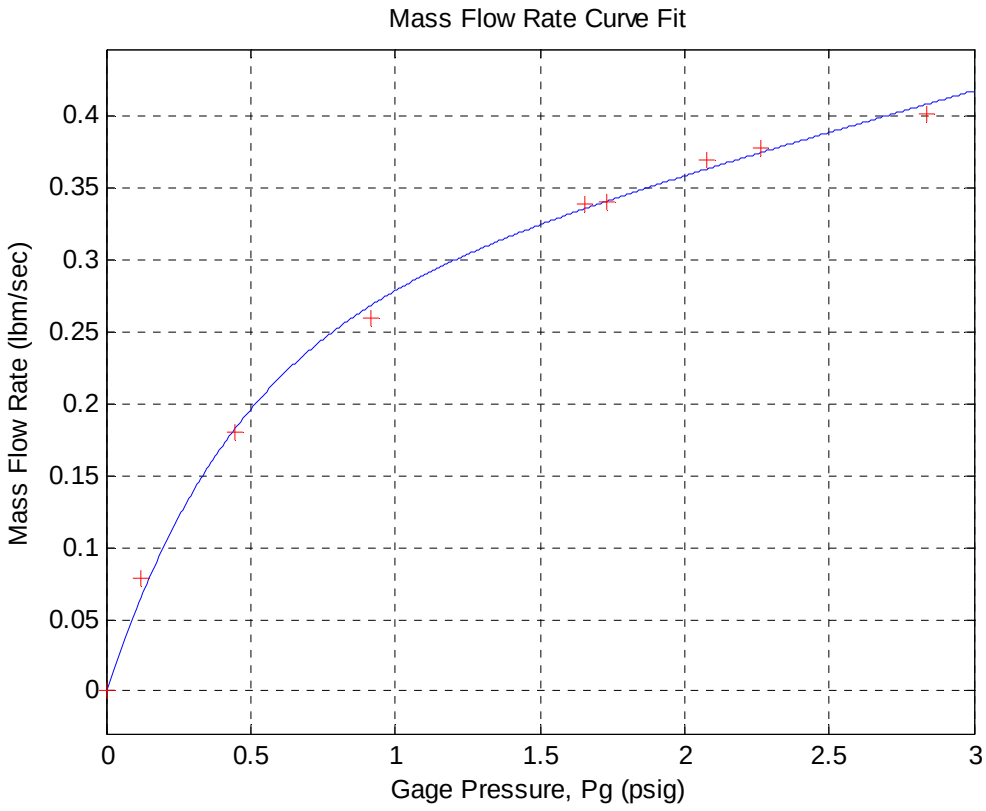

Figure 5-19: Permeability Results for the Nominal 4072 Airbag

Table 5-10: Airbag 4084 Permeability Test Data

Airbag	P_g	P_0-P_{atm}	P-P_{atm}	T_0	M	$\dot{m}$
4084	0.20344	0.62252	-0.3298	531.5	0.3042	0.1551
	0.5145	1.95887	-1.0673	531.5	0.543	0.2679
	0.95994	3.78199	-2.1089	531.8	0.7614	0.356
	1.37868	5.65019	-3.1534	533.3	0.9376	0.4121
	1.92001	7.97663	-4.5834	535.2	1	0.4599
	2.11543	8.89301	-5.1875	536.3	1	0.478
	1.93469	8.1895	-4.7117	535.3	1	0.4642
	2.27933	9.99693	-5.8444	536.2	1	0.5005
	2.63525	11.8577	-6.966	537.2	1	0.5377

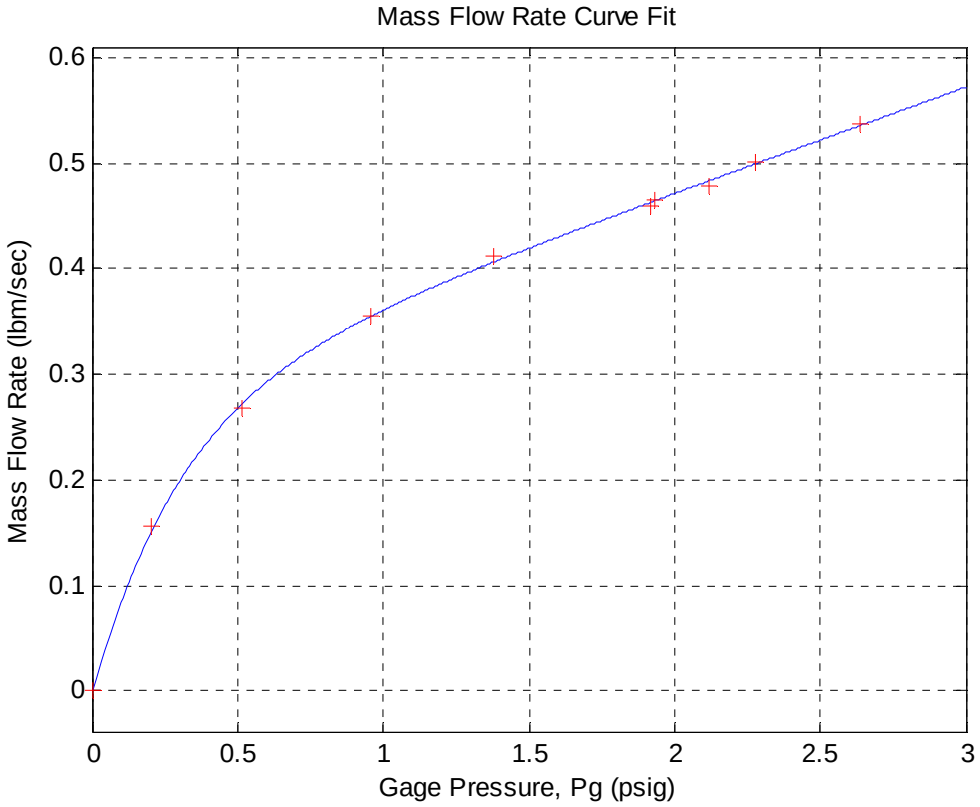

Figure 5-20: Permeability Results for the Nominal 4084 Airbag

Figure 5-20 shows the permeability results for the nominal 4084 airbag. This curve was also used for the nominal 4060 airbag since it was not available for permeability

testing. The results are used on a per square inch basis, so the surface area difference does not matter.

The permeability results show pounds mass of air that leak out of the airbag per second as a function of airbag pressure, measured by a pressure sensor in a quiescent location inside the airbag. The nonlinear air flow curve at low gauge pressures is an indication of flow through the initial pores in the unstrained fabric. Air flow jumps rapidly from zero gauge pressure, because there are open pores in the unstrained fabric that pass air with the slightest increase in gauge pressure. If fixed, these pores would choke the air flow to a constant rate as the pressure rose. Instead, these pores strain further open as gauge pressure rises, allowing more air flow. This occurs in the region of the curve that is linear with gauge pressure shown in the experimental results.

A constitutive model for mass flow rate through the pores that accommodates both the initial exponential flow rate through the unstrained pores and the linear variation with pressure for strained pores is as follows:

$$-\dot{m} = A_{Lf}\left[R_L P_g + \dot{m}_{A0}\left(1 - e^{-\alpha P_g}\right)\right], \text{ where } \dot{m}_{A0} = \dot{m}_0 / A_{Lf} \qquad (5\text{-}10)$$

The leak rate R_L is per unit area; therefore, the experimentally measured air mass flow must be divided by the fiber leak area A_{Lf} of each airbag. Leak area A_{Lf} is a constant for the permeability test, but a function of collidant contact area during collisions. Equation (5-10) expresses mass flow rate as a nonlinear function of gauge pressure, depending on three parameters, $\dot{m}_{A0}$ (or $\dot{m}_0$), α, and R_L. The three parameters were found by nonlinear least squares regression of Equation (5-10) to the permeability data as a function of pressure.

Table 5-11 shows the R_L and $\dot{m}_{A0}$ values for each airbag. Airbag height is in inches, and A_{Lf} is in square inches. A_{Lf} for the permeability experiment is calculated as the unstrained fabric area minus the initial pore area. A_{p0} used in the Fanno Equation (3-4) in Chapter 3, is measured microscopically to be approximately 0.01. A_{Lf} is essentially A_0, which is the airbag circumference × height plus the top and bottom circular areas minus the door area in the bottom. The units of $\dot{m}_{A0}$ are lbm/(sqin-second). αP_g is dimensionless, so $\alpha \sim 1/P_g$.

Table 5-11: R_L and $\dot{m}_{A0}$ Values for Each Airbag

Airbag	Height	A_{Lf}	R_L	$\dot{m}_{A0}$	α
	inches	sq in	sec/in	slinch/sqin-sec	
3060	56.25	6452	2.998E-08	1.011E-07	2.041
3072	68.5	7577	2.064E-08	9.951E-08	1.457
3084	79.5	8662	2.613E-08	7.470E-08	2.412
3660	56.5	8020	2.688E-08	9.762E-08	2.156
3672	68.5	9324	3.390E-08	7.090E-08	3.100
3684	79.5	10544	2.731E-08	7.062E-08	2.996
4072	68.25	10994	1.336E-08	5.820E-08	2.275
4084	80	12502	2.076E-08	5.607E-08	3.273

F. Summary

Empirical models were developed for airbag elasticity and airbag permeability. These results, unique to each airbag, provided values for the dynamic and thermodynamic models.

VII: Airbag Simulation and Comparison to Experiments

This chapter describes the coded mathematical simulation of the experiments. The full graphical results of two single airbag impact simulations are presented and compared to physical experimental results. Peak acceleration and peak pressure results of multiple airbag impact simulations are compared to drop test experimental results.

The mathematical models derived in Chapters 3 and 4 were used to build a simulation code for the collidant hitting an airbag. The airbag permeability model was based on the permeability experiments discussed in Chapter 5.

A. Simulation Code

The simulation code solves the physics and kinematics equations from Chapters 3 and 4 with an explicit $4^{th}/5^{th}$-order Runge-Kutta ordinary differential equation solver [7-1: pg 5-1]. The ordinary differential equations it solves are Equations (5-10), (3-8), and (3-33) for state variables $m, z, \dot{z}, \text{and } P$.

An initial conditions file that specifies the collidant downward velocity at initial contact with the airbag and the airbag pressure at that time is used to set the starting conditions of the simulation. Initial elevation is calculated as the height of the strained airbag dome center at the initial pressure. Initial mass inside the airbag is calculated as $m_0 = \rho_0 V_0$ where $\rho_0 = 1.2138 \times 10^{-7}$ slinch/inch^3 is the standard density at 750 feet above sea level at 60^{o}F and V_0 is the initial Phase 0 strained airbag volume calculated for the initial airbag pressure. The initial condition routine also initializes the appropriate airbag and collidant constant parameters.

At each time step, the ordinary differential equations for $m, z, \dot{z}$, and P involve other state variables. The terminal dome angle θ_t in Phase 2 must be calculated using a non-linear equation solver for the transcendental equation (4-17).

The static equilibrium Equations (3-18) and (3-44) are also transcendental equations, because they depend on the airbag geometry, which depends on strain, which in turn depends on stress through the constitutive Equation (3-3). Therefore, Equations (3-18) and (3-44) also require a non-linear equation solver at every time step.

Finally, because the geometry varies with azimuth angle of the rectangular collidant during Phases 2 and 3, the leak area and volume Equations (4-38) and (4-54) require numerical integration. These integrals were evaluated using adaptive Lobatto quadrature [7-1: pg 4-29]. To simplify the coupling of strain with geometry, uniform strain was assumed. Longitudinal stress and strain dependence on azimuth was neglected by calculating longitudinal stress for an equivalent cylindrical collidant. That is, the meridional radius, r, appearing in Equation (3-44) for σ_L was initially determined for a cylindrical collidant with the same face area of the actual rectangular collidant. Once the uniform state of strain was fixed at each time step, the area and volume integrations were carried out for geometry, including meridional radius, that varied with azimuth angle, ϕ.

State variable time histories and peak accelerations and pressures are plotted as a post-processing step. Since the Fanno equations do not enter the simplified differential equations, pore flow quantities such as pore resistance force are also calculated as a post-processing step.

B. Single Airbag Simulation Curves Compared to Impact Experiment

The simulation was run with our experimental permeability data. Simulation results are plotted on the same figure with the impact experimental results for comparison. Two cases were chosen for comparison with the experimental results. One was the nominal 14-inch by 18-inch gondola (designated as 1418) with 357 lb weight, dropped from 15 feet, hitting a nominal 40-inch diameter, 60-inch tall airbag (designated as 4060). The second was the 1418 gondola with 477 lb weight, dropped from 15 feet, hitting a nominal 30-inch diameter, 84-inch tall airbag (designated as 3084). The impact chronology is traced with video gondola kinematic data and airbag pressure data.

The initial contact starting time was determined for the experiment as the time when the gondola acceleration rose above −1 G. The problem with this ideal was that for most of the experiments the acceleration data was collected only after the acceleration had risen above −1 G. In the few cases with −1 G data, its timing was compared to the pressure data, which was comprehensive. The airbag pressure was steadily falling as the inflation tank blew down until impact; then it rose rapidly. The pressure nadir occurred approximately 16 milliseconds after the gondola acceleration broke above −1 G for the case of the 2525 gondola weighing 447 lbs hitting a 4072 airbag, one of the few cases with this much recorded pre-history. Therefore, 16 milliseconds before the pressure nadir was chosen as the starting point for initial gondola airbag contact for all cases. The gondola elevation and velocity and the airbag pressure at this time were used as the initial conditions for all the simulations. The simulations begin at first contact between the collidant and airbag, calculated as the height of the airbag when inflated to the initial condition pressure.

The experimental impact chronology begins for the first case with the gondola lower face falling at −268 inches/second and contacting the airbag upper face, as indicated by the gondola acceleration rising above −1 G in Figure 7-1 at the 0 millisecond mark. The drop test data is indicated by the thin blue line designated “Impact”. The simulation results are the magenta line with square data points designated “Sim”.

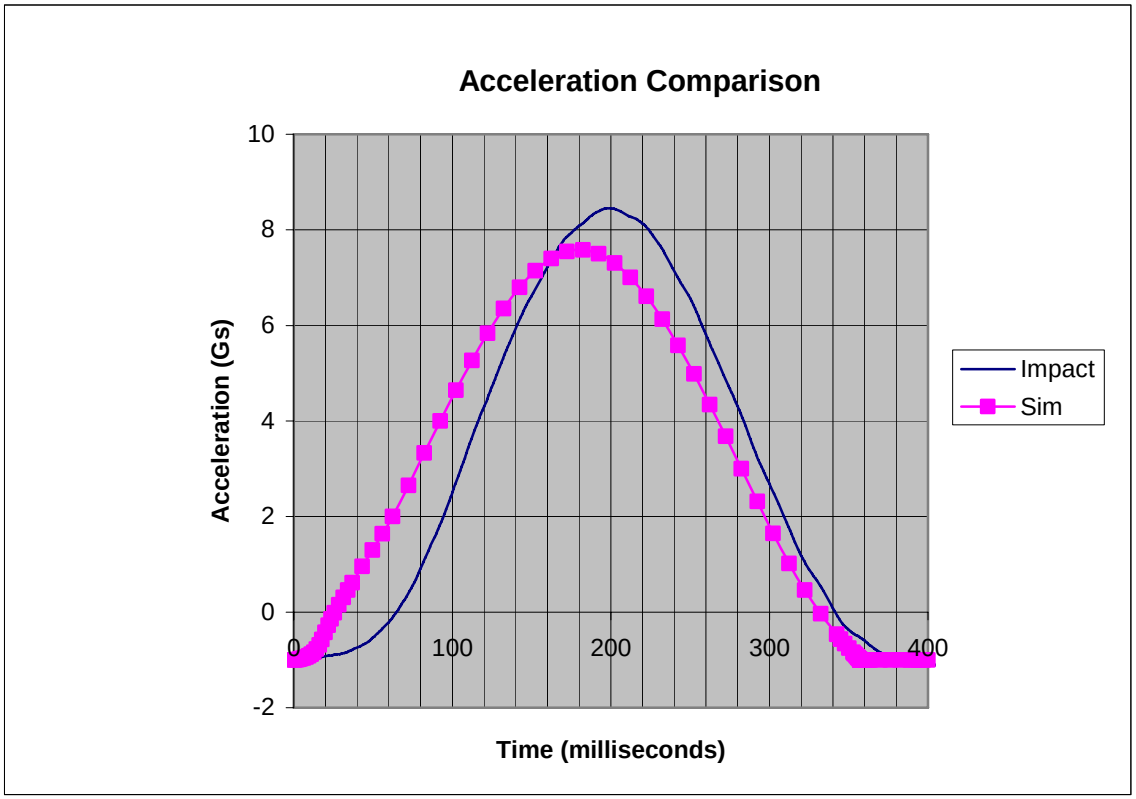

Figure 7-1: Gondola Smoothed Acceleration

The peak accelerations were different for the simulation and the experiment. The experiment peak was 8.45 G’s, whereas the Sim peak was 0.87 G’s or 10.3% lower at 7.58 G’s.

Airbag pressure starts at 0.396 psig and falls a bit at first before rising again a few dozen milliseconds later as Figure 7-2 shows. The initial fall in pressure shows up in both the drop test data and the simulations. The simulations show that the airbag actually increases in volume after initial impact as the top of the airbag moves from a hemispherical dome shape to a more flat-headed cylinder. This increase in volume lowers the airbag pressure. This effect seemed faster and more pronounced in the simulations than the drop test. The actual airbag had a more elliptical shaped dome than the hemisphere assumed for the simulation.

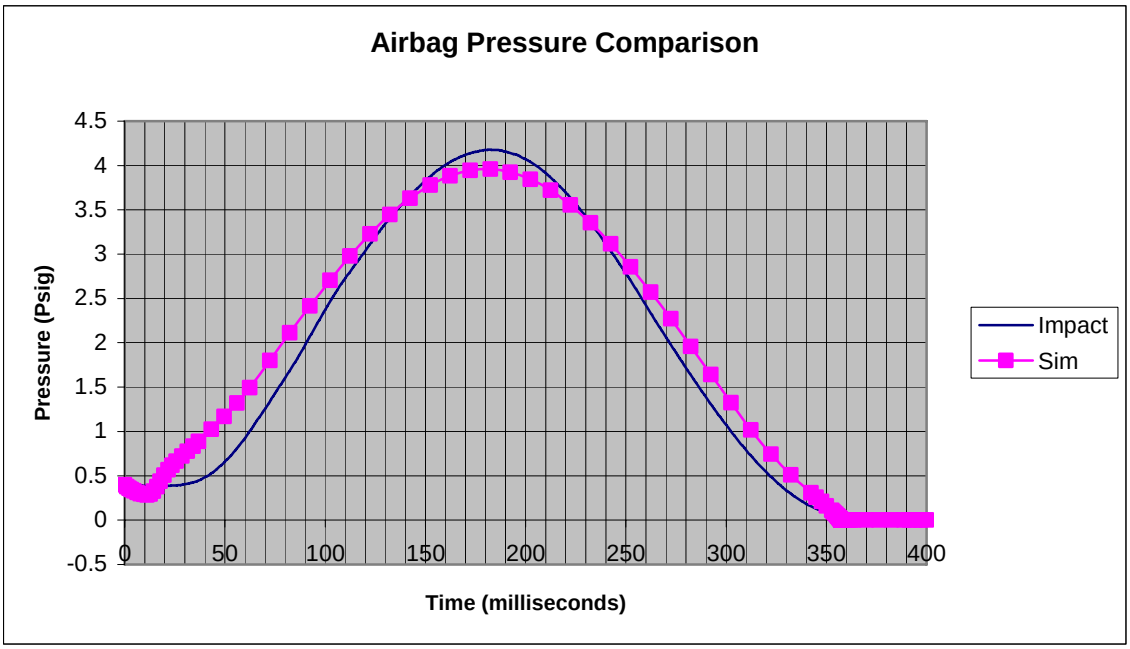

Figure 7-2: Airbag Smoothed Pressure

The peak pressures were different for the two simulations and the experiment. The experiment peak was 4.21 psig, whereas the simulation peak was lower by 0.25 psig, or 6.0%, at 3.96 psig.

The durations of the acceleration and pressure event in the simulations were slightly longer than the drop test. This longer duration, typical of a longer airbag, is probably due, at least in part, to the hemispherical dome being higher than the true elliptical dome. Unfortunately, the inflated airbag height at initial contact could not be determined precisely from the video instrumentation for direct comparison.

Gondola elevation was 123.7 inches at the 0 millisecond mark, as calculated by the simulation, and continues to fall, but less rapidly than in the experiment, as shown in Figure 7-3. Initially, the simulations track the experimental data closely. But the rebound occurs earlier in the simulations than the experiment. The rebound trajectory for the simulation follows the slope of the experimental rebound closely. The gondola penetrates an extra ~30 milliseconds and an extra 9.48 inches into the airbag during the experiment versus the simulations. The choice of starting time for the initial contact affects this outcome.

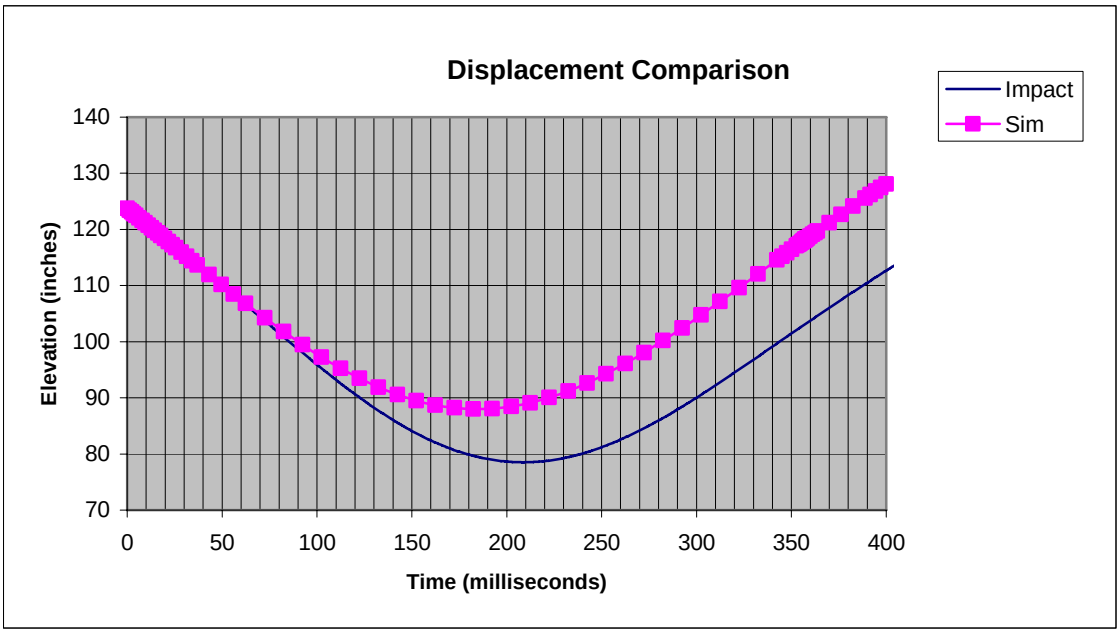

Figure 7-3: Gondola Smoothed Elevation

The simulation elevation reaches its nadir at about 185 milliseconds and nearly recovers to impact elevation another 185 milliseconds later. Full recovery would occur in the conservative simulation of an impermeable airbag, which would have no energy dissipation. In contrast, the experimental elevation reaches its nadir at about 210 milliseconds. Another 210 milliseconds later, its recovery to the initial contact elevation of 123.7 inches was less complete. This potential energy loss may be due to two sources of energy dissipation. One is friction of the gondola sliding along its guide cables, assumed to be negligible. The other is energy loss through pore flow of the permeable airbag fabric. This result would indicate that the experimentally determined permeability may have been under-recorded. The latter explanation is most likely because of the large amount of energy involved and because adjusting the permeability model improved the curve fit substantially.

Another measure of energy loss is the difference in kinetic energy loss. Gondola velocity was experimentally determined to be –268 inches/second at the 0 millisecond mark and remains negative during initial impact as seen in Figure 7-4. Initially, the simulations track the experimental data closely. The difference in minimum velocities is 12.08 inches/second. But the rebound is ~30 milliseconds earlier in the simulations than the experiment. The slope of the rebound velocity of the simulation is close to the slope of the experimental rebound velocity. The peak rebound velocity of the simulation is 266.2 inches/second, only 34.3 inches/sec higher than the experiment (231.8 inches/second), therefore retaining more kinetic energy. In fact, the kinetic energy loss for the simulation is only 20% versus 50% for the experiment, as noted at the end of Chapter 6. The lower predicted kinetic energy loss likely indicates that the

experimentally determined permeability is too low. The slopes of the final velocities for both cases match, because there is no collidant airbag contact, and gravity rules.

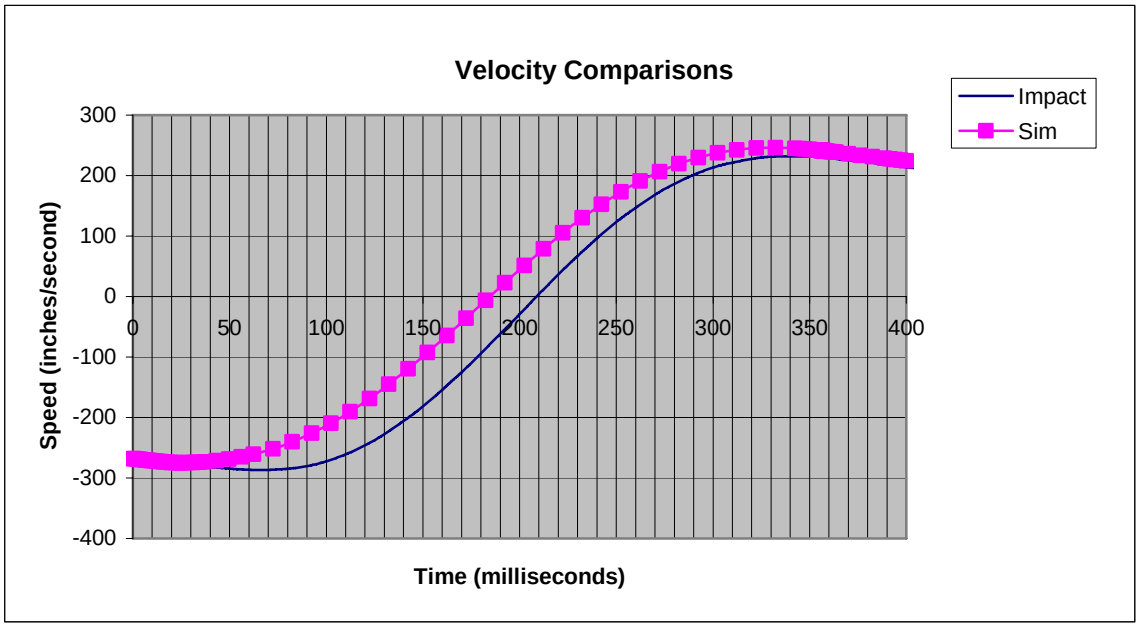

Figure 7-4: Gondola Smoothed Velocity

Figure 7-5 shows plots of the simulation airbag geometric parameters, L, R, r, s, and z as well as dome meridional (bubble) angle θ_t. Solid lines depict values of kinetic variables at the collidant corner ($\phi = \phi_C$) and dashed lines at the collidant side ($\phi = 0^\circ$). Approximately two thirds of the duration of the impact, the airbag was in Phase 3 impact geometry, from 60 milliseconds to 300 milliseconds as seen in Figure 7-6. The large errors in acceleration and pressure occur during the Phase 2 simulation, from 20 to 60 milliseconds, leading one to believe that the model or assumptions of Phase 2 are inaccurate. Fidelity improves during Phase 3.

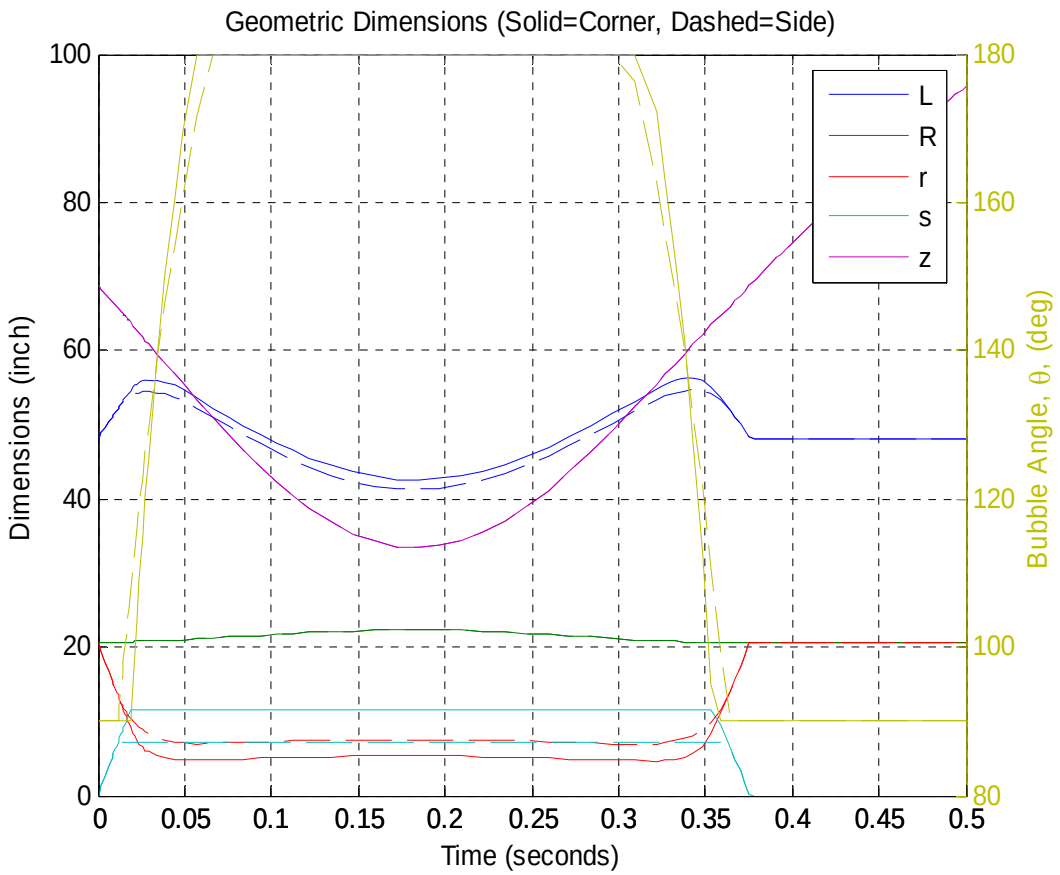

Figure 7-5: Simulated Airbag Dimensions

Figure 7-6 also shows the simulation's impact phases as well as the airbag volume. Mixed Phase 1 at the corner and Phase 2 at the side is indicated as Phase 1.5 at approximately 20 milliseconds. The airbag volume is compressed about 15%. Figure 7-7 shows plots of the simulation airbag air mass dropping off by about 4%. This high air retention might explain the higher rebound velocities relative to the experiment.

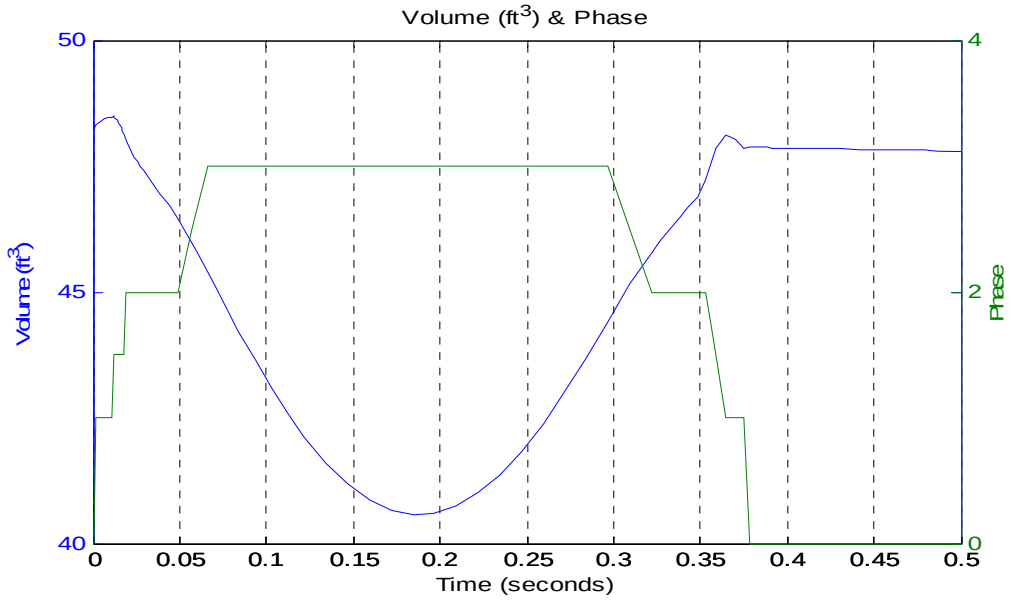

Figure 7-6: Airbag Volume and Impact Phases

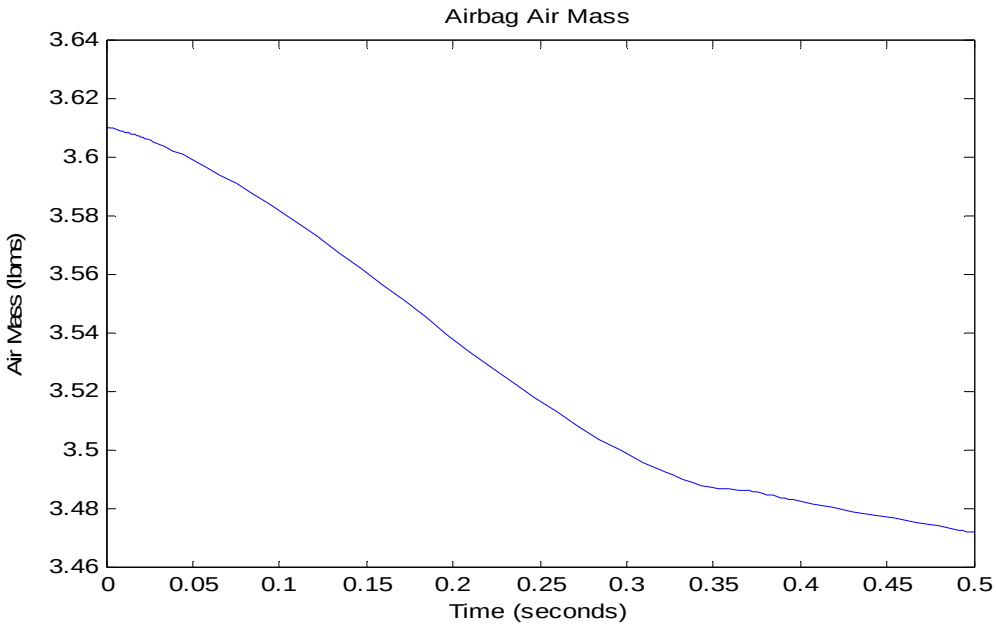

Figure 7-7: Airbag Air Mass

Figure 7-8 shows the airbag strains. Hoop strains are dominant, reaching almost 9%, whereas longitudinal strain stays below half a percent. As a result, the Poisson effect of

the hoop stress overwhelms the longitudinal stress effect on longitudinal strain, making it negative. The effect of the assumption of uniform longitudinal strain around the azimuth should be small, given the small amplitude of the strain. Accurate hoop strain modeling is important given its large amplitude. The variation in hoop strain with azimuth caused by the Poisson effect would be small given the low amplitude of longitudinal strain. Moreover, strains have an integrated effect on airbag pressure and collidant dynamics. Therefore, the assumption of uniform hoop strain is probably accurate to the experiment.

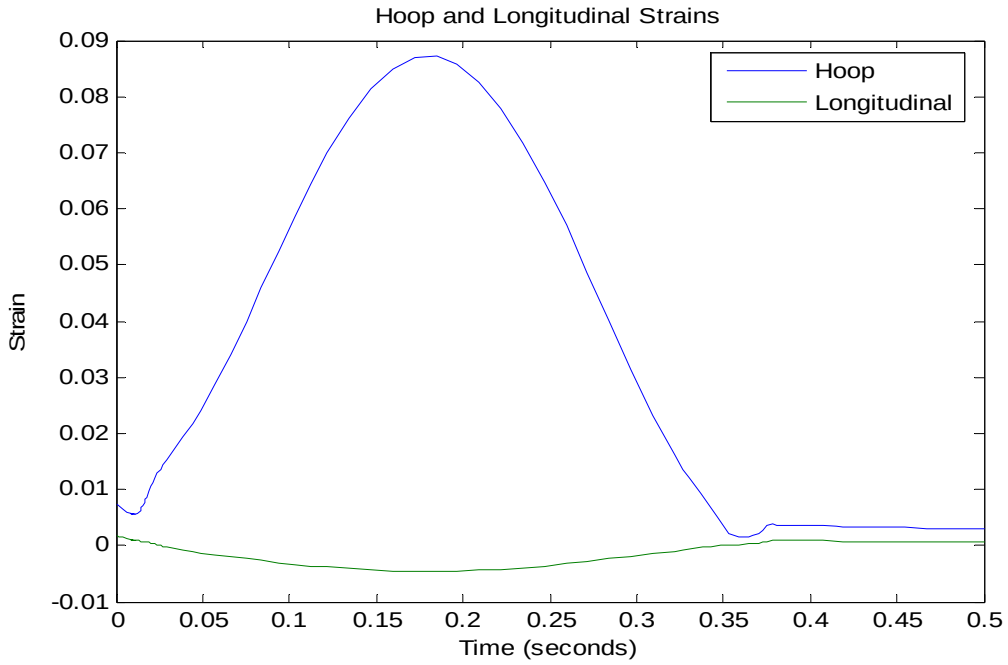

Figure 7-8: Airbag Hoop and Longitudinal Strains

Figure 7-9 shows the airbag pore flow resistance force, which is comparable in magnitude to the trampoline force, shown for comparison. It is essentially equivalent to the gauge pressure acting over the same pore area of an impermeable fabric. Thus,

ignoring the Fanno flow resistance force and replacing it with airbag pressure times pore area is a good simplification.

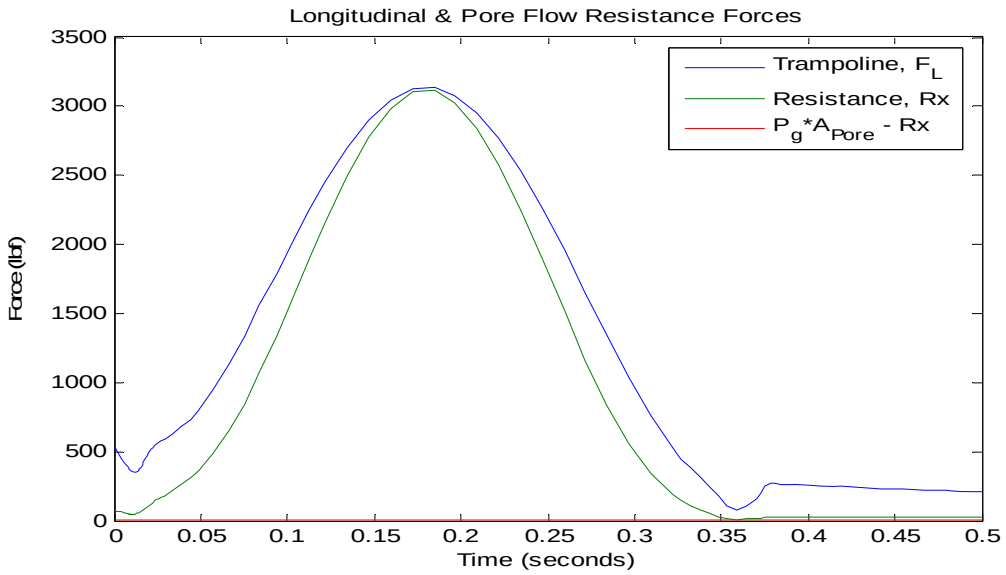

Figure 7-9: Airbag Pore Flow Resistance

Choosing a 16 millisecond later time in the experiment for the initial contact in the simulation yields a much closer fit to the experimental curves as shown in Figures 7-10 to 7-13. Simulation peak acceleration was within 7.1% of the experiment versus 10.3% for the 16 millisecond earlier contact. The simulation peak pressure was within 3.3% of the experiment versus 6.0% for the 16 millisecond earlier contact. The simulation's lowest elevation was within 4.81 inches of the experiment versus 9.48 inches for the 16 millisecond earlier contact. The simulation peak rebound velocity was within 25.7 inches/second of the experiment versus 34.3 inches/second for the 16 millisecond earlier contact. The collidant kinetic energy loss was only 19.7% versus 50% for the experiment. This result most likely indicates that collision experiment airbag had a

higher permeability than the simulation airbag. The simulation results show other symptoms of lower permeability, for instance, more airbag pressure retention, hence higher early and late pressures and hence higher early and late collidant accelerations. These conditions cause less airbag penetration, hence lower peak pressures and peak accelerations.

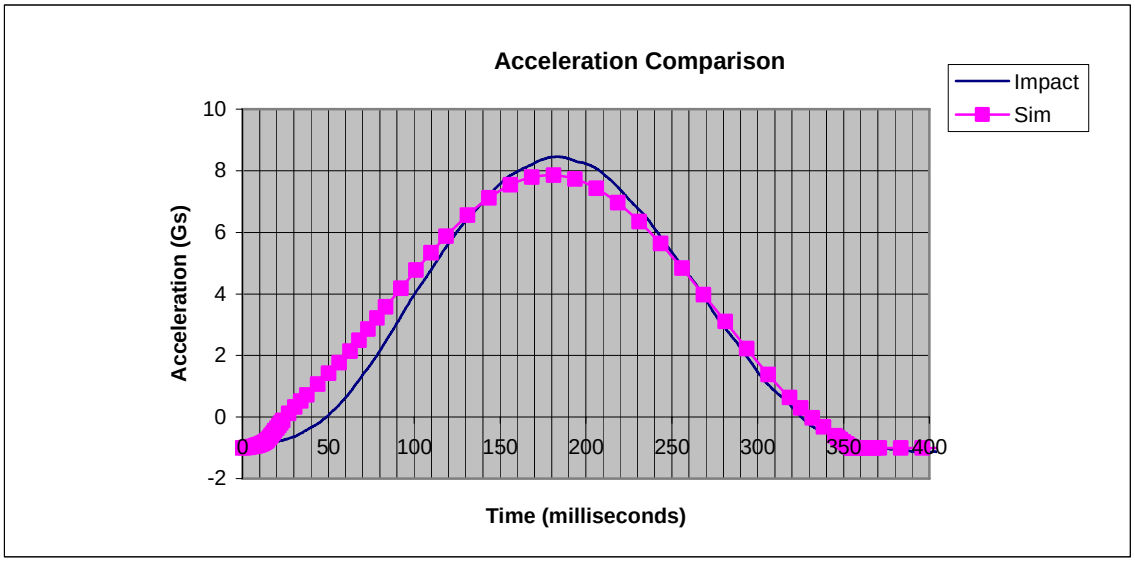

Figure 7-10: Later Contact Collidant Acceleration

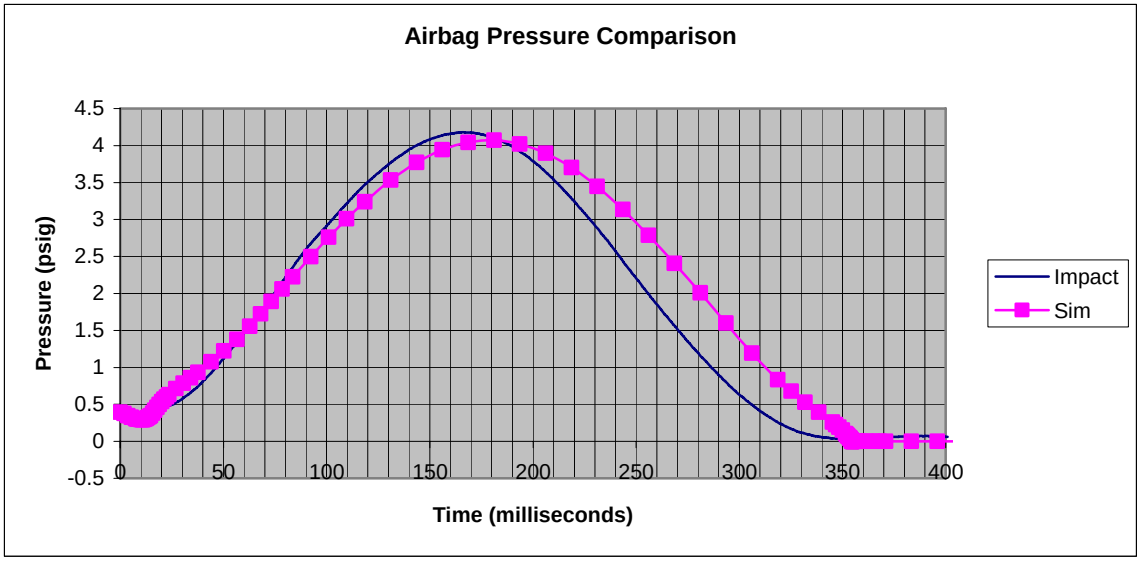

Figure 7-11: Later Contact Airbag Pressure

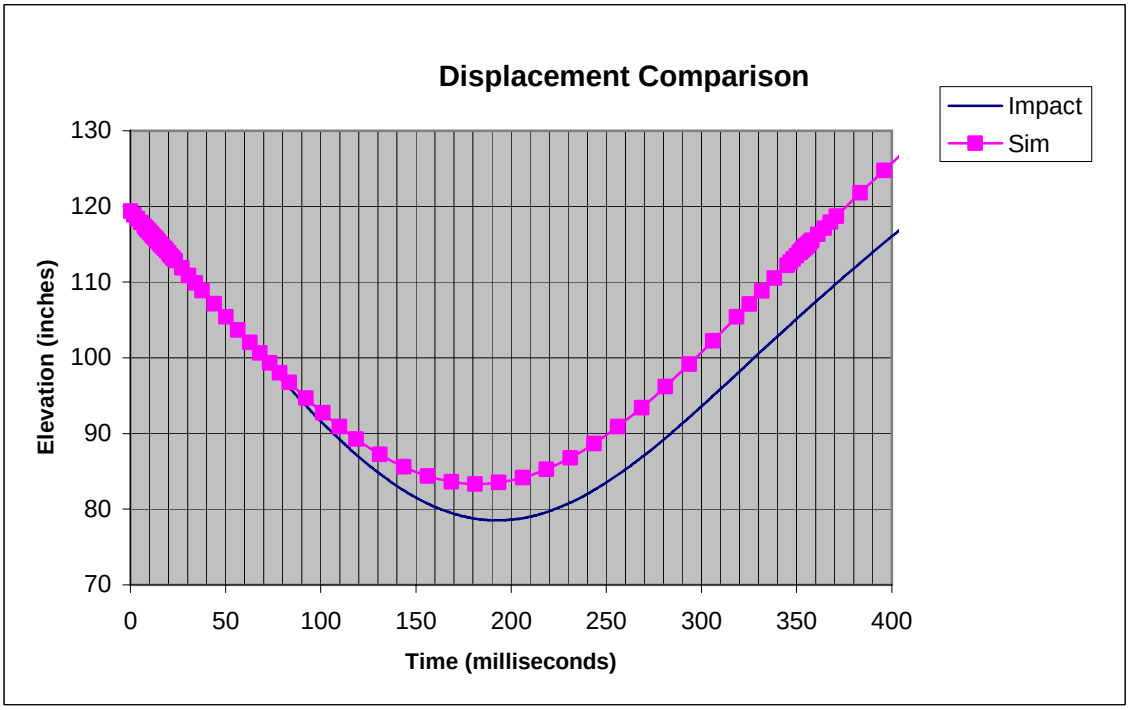

Figure 7-12: Later Contact Collidant Elevation

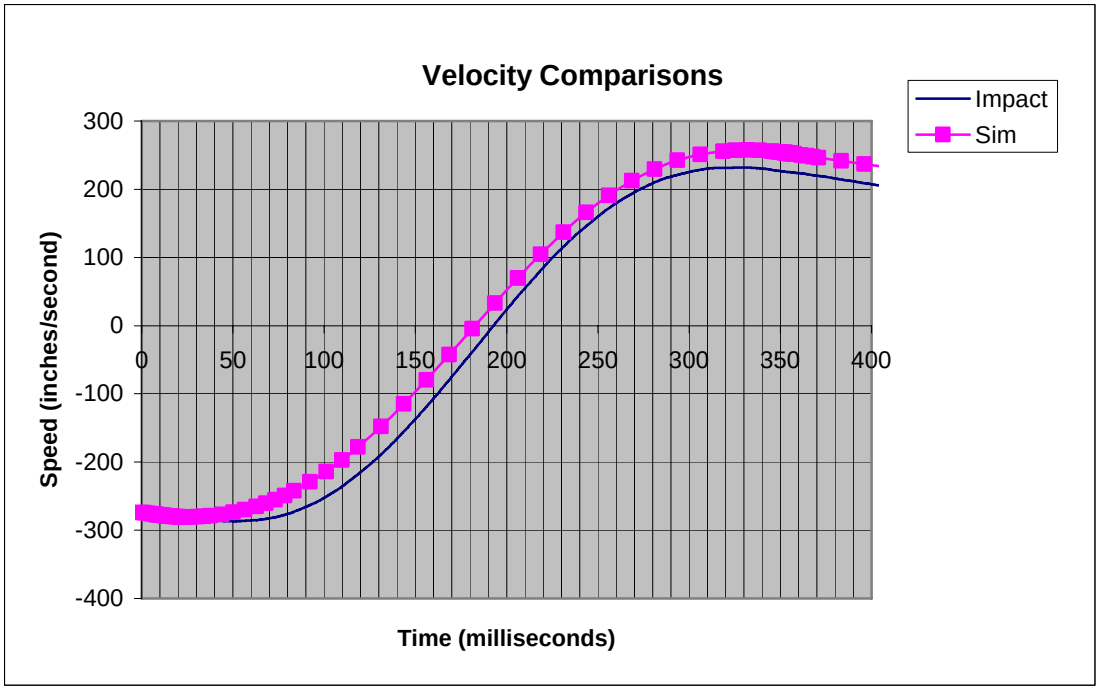

Figure 7-13: Later Contact Collidant Velocity

Given the higher fidelity of Phase 3 versus Phase 2 in the simulation, the case of an airbag that spends an even larger fraction of the impact in Phase 3 is examined. This case is a 3084 airbag with a 477 lb gondola. The heavier gondola penetrates deeper. The smaller diameter means smaller *r* and hence shorter Phase 1 and 2. Figure 7-14 shows the accelerations for this case. The fit is tighter than the 4060 airbag case. The difference in peak acceleration is only 3.6% (about a third of the 4060 error). The time at which peak acceleration occurs in the simulation is coincident with the experiment, versus leading by 20 milliseconds in the 4060 case.

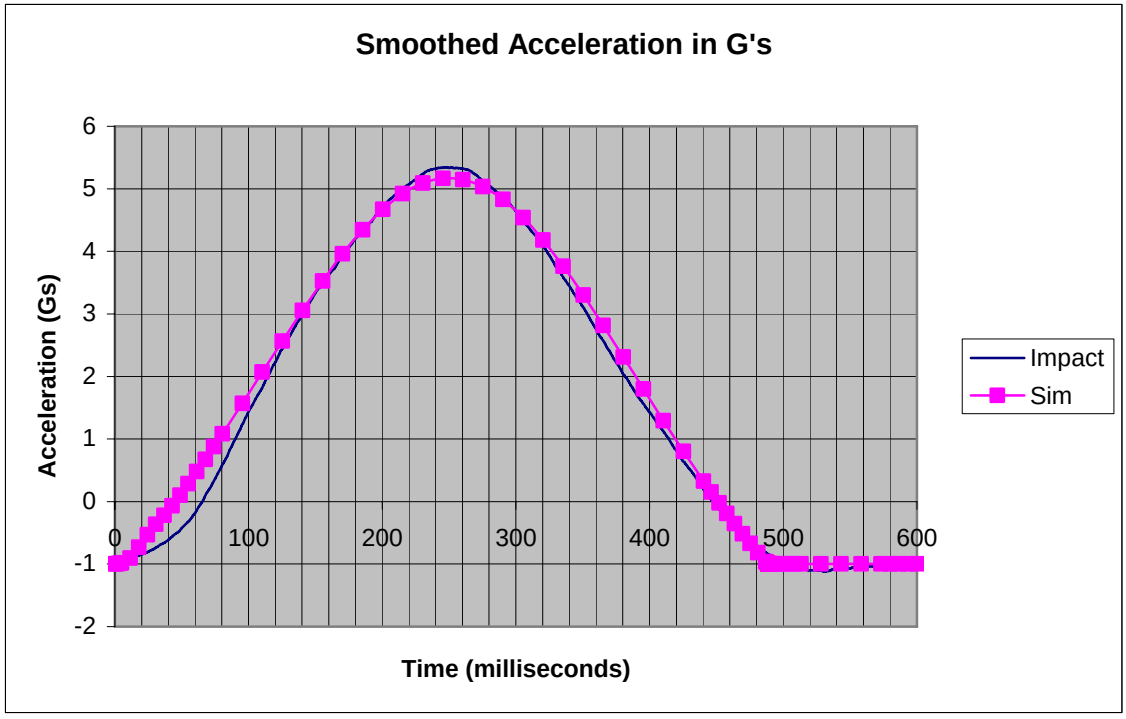

Figure 7-14: Acceleration for Airbag 3084 with 477 lb Gondola

Figure 7-15 shows the pressures for this case. The fit is tighter than the 4060 airbag case. The difference in peak pressure is only 2.1% (about a third of the 4060 error). The peak pressure in the simulation is coincident with the experiment as in the 4060 case. The major error occurs during Phase 2 of the impact (from 20 to 60 milliseconds). The other looseness of fit occurs on the down slope where the simulation probably has too much air still in the airbag, leading to added pressure.

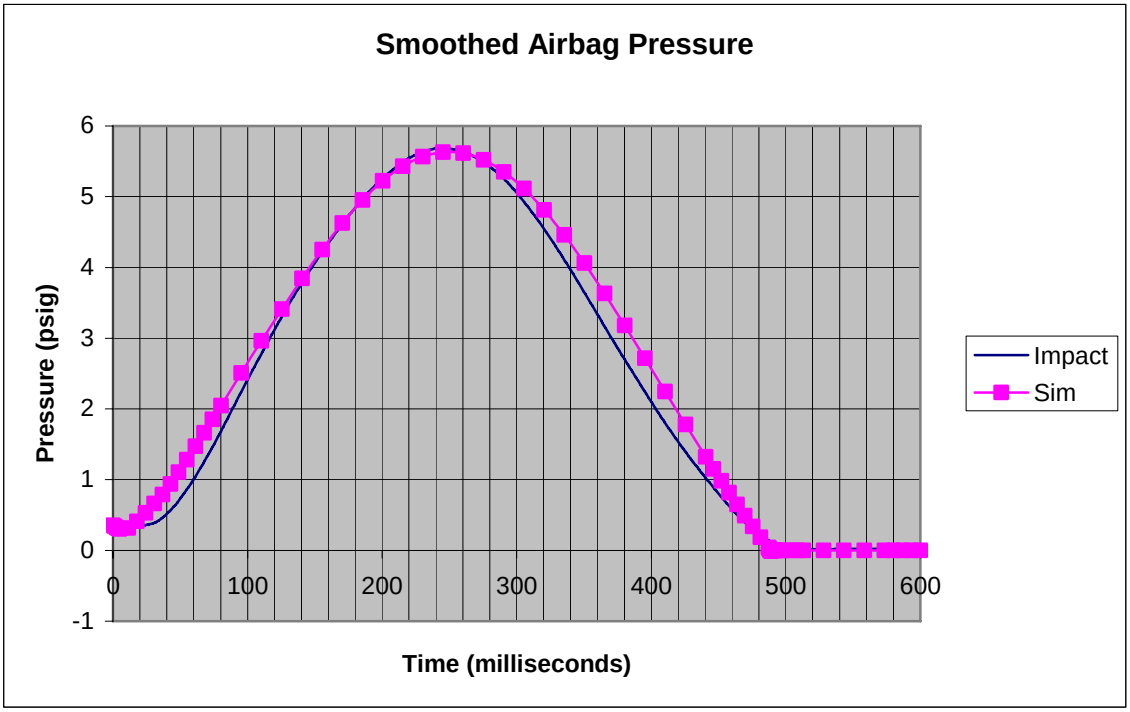

Figure 7-15: Pressure in 3084 Airbag

Figure 7-16 shows the gondola displacements/elevations for the 3084 case. The fit is tighter than the 4060 airbag case. The difference in minimum elevation is only 3.28 inches (about a third of the 4060 error). The minimum elevation in the simulation is almost coincident with the experiment versus leading by 30 milliseconds in the 4060 case. The looseness of fit occurs at least in part, due to the accumulated velocity errors.

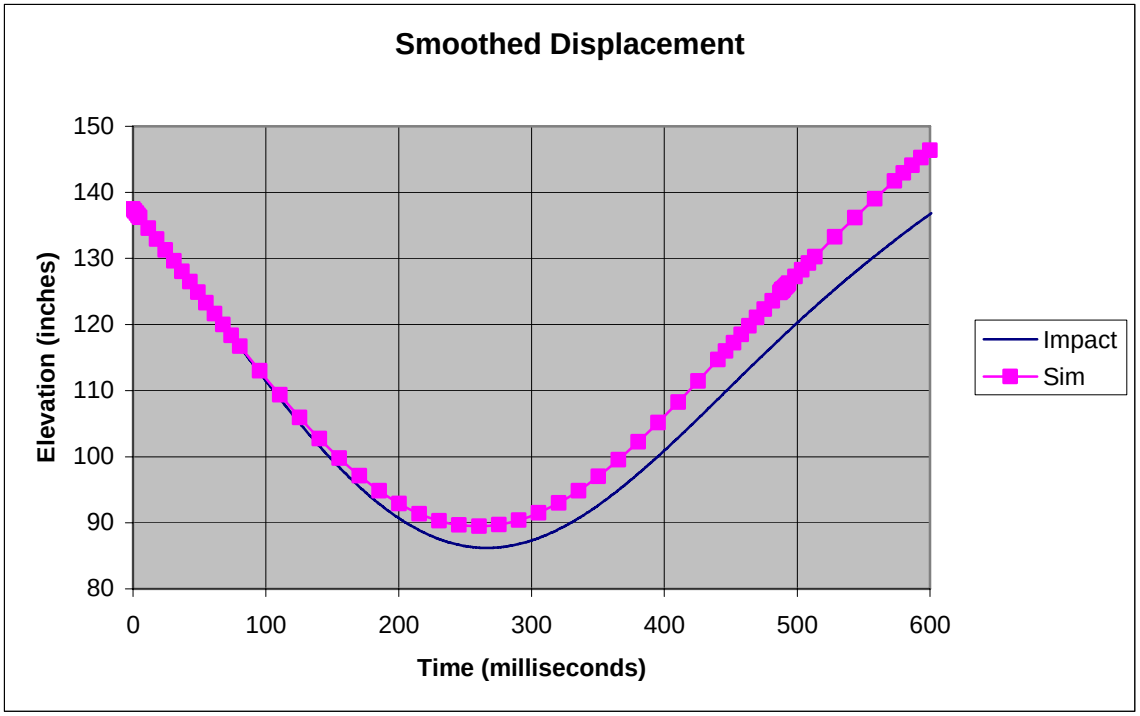

Figure 7-16: Gondola Elevation for 3084 Airbag

Figure 7-17 shows the gondola velocities for the 3084 case. The fit is tighter than the 4060 airbag case. The difference in minimum velocities is only 6.63 inches/second (about 55% of the 4060 error). The zero velocity in the simulation is almost coincident with the experiment versus leading by 30 milliseconds in the 4060 case. The difference in maximum velocities is 22.40 inches/second (about 65% of the 4060 error). The discrepancy occurs, at least in part, due to the accumulated acceleration errors during rebound. Under-predicting permeability may also be at fault, because the predicted velocities are consistently more positive than the experiment.

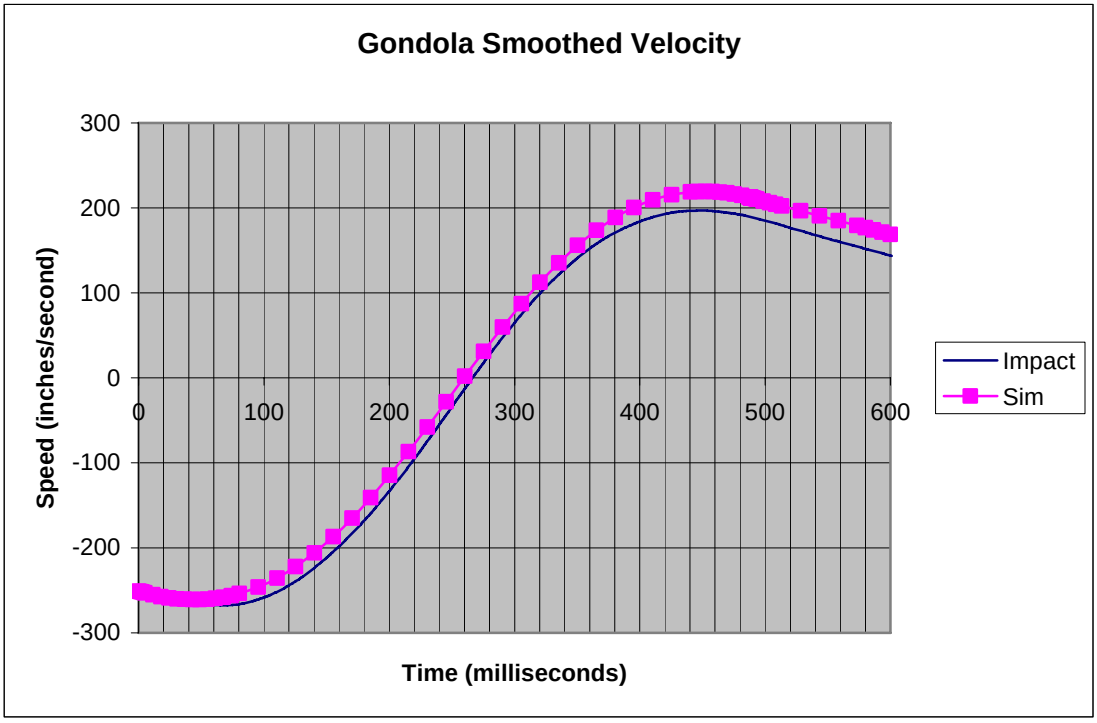

Figure 7-17: Gondola Velocity for 3084 Airbag

C. Multiple Airbag Simulation Peaks Compared to Impact Experiments

1. Peak Accelerations.

The peak accelerations predicted by the simulations were consistently lower than the experimental impact results. Table 7-1 shows the peak collidant accelerations from simulations and impact experiments, the difference, and the percentage difference with the impact as the reference. The gondola for these experiments was the 1418 gondola, and the drop height was 15 feet. Figures 7-18 to 7-26 show these differences graphically.

Table 7-1: Comparison of Peak Accelerations from the Measured Permeability Simulation to the Drop Test

	Gondola 1418 Weight (lbs)											
	357				477				597			
Airbag	Sim	Exper	Diff.	Diff. %	Sim	Exper	Diff.	Diff. %	Sim	Exper	Diff.	Diff. %
3060	7.56	8.89	-1.33	-15.0	6.95	8.57	-1.62	-18.9	6.58	7.33	-0.75	-10.3
3660	7.71	8.71	-1.00	-11.5	7.06	7.92	-0.86	-10.9	6.64	7.23	-0.59	-8.1
4060	7.58	8.45	-0.87	-10.3	6.91	7.86	-0.95	-12.1	6.48	7.35	-0.87	-11.8
3072	6.60	6.9	-0.30	-4.4	6.04	6.4	-0.36	-5.7	5.7	6.67	-0.98	-14.6
3672	6.46	6.87	-0.41	-6.0	5.88	6.28	-0.41	-6.5	5.5	6.1	-0.6	-9.8
4072	6.55	7.01	-0.46	-6.6	5.96	6.47	-0.51	-8.0	5.57	6.11	-0.54	-8.8
3084	5.65	5.86	-0.21	-3.6	5.15	5.34	-0.19	-3.6	4.83	5.1	-0.27	-5.3
3684	5.46	5.68	-0.22	-3.9	4.96	5.25	-0.29	-5.6	4.64	5.01	-0.37	-7.4
4084	5.61	6.21	-0.60	-9.7	5.08	5.56	-0.48	-8.6	4.74	5.17	-0.43	-8.3

The simulation results regarding peak accelerations were consistently lower than the drop test results, varying from 3.6% to 18.9% lower. The differences between the simulations and the drop tests were fairly consistent on a percentage basis over the various airbags and gondola weights. No major trends emerged, except that the error between simulation and experiment shrunk as the airbag height increased. The taller airbags spend a larger fraction of impact time in Phase 3 of impact. Perhaps Phase 3 is better modeled than Phase 1 and 2. The hemispherical geometry assumption of Phase 1 and 2 may be less accurate than an elliptical shape assumption, but simpler to model. Of the remaining minor trends, the most significant one was that the middle diameter (36-inch) airbags showed the most consistently close fit between the simulation and the drop test.

The simulation matches the slope and curvature of the experimental data in most cases. The experimental motion data had some random jitter in the image analysis

software that caused the centroid to jump around inside the flashlight image, causing displacement measurement noise.

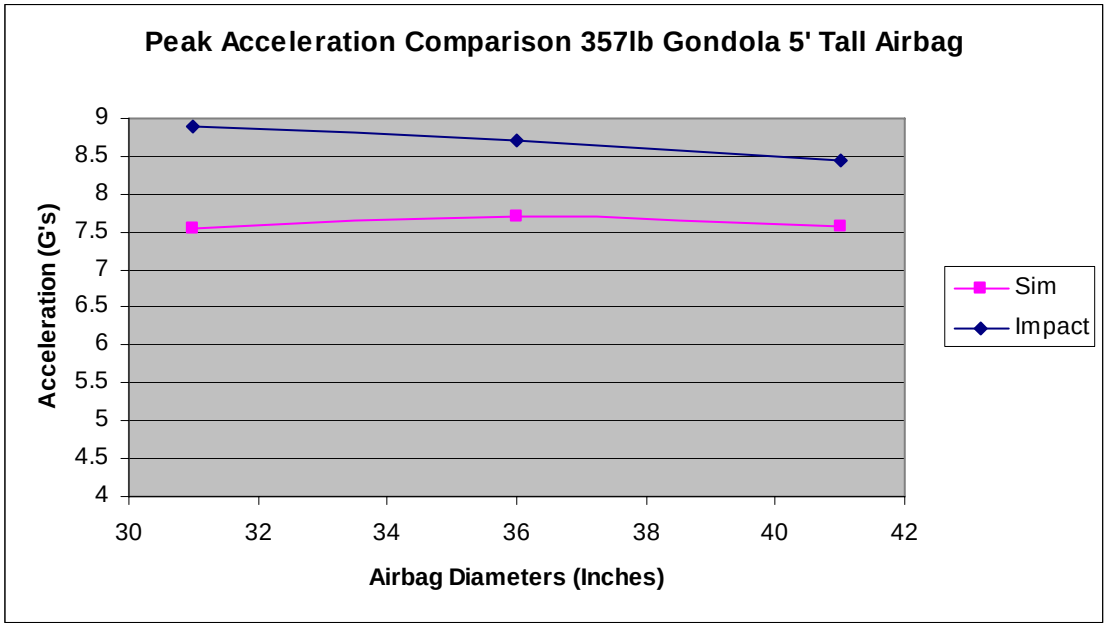

Figure 7-18: Peak Acceleration Comparisons 5-foot Tall Airbag

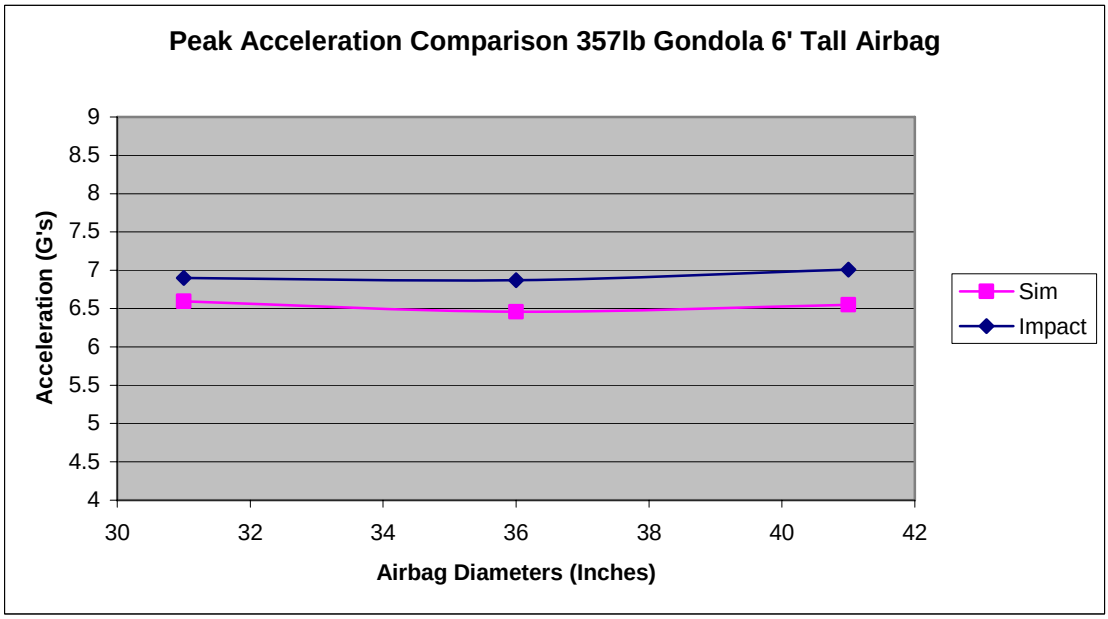

Figure 7-19: Peak Acceleration Comparisons 6-foot Tall Airbag

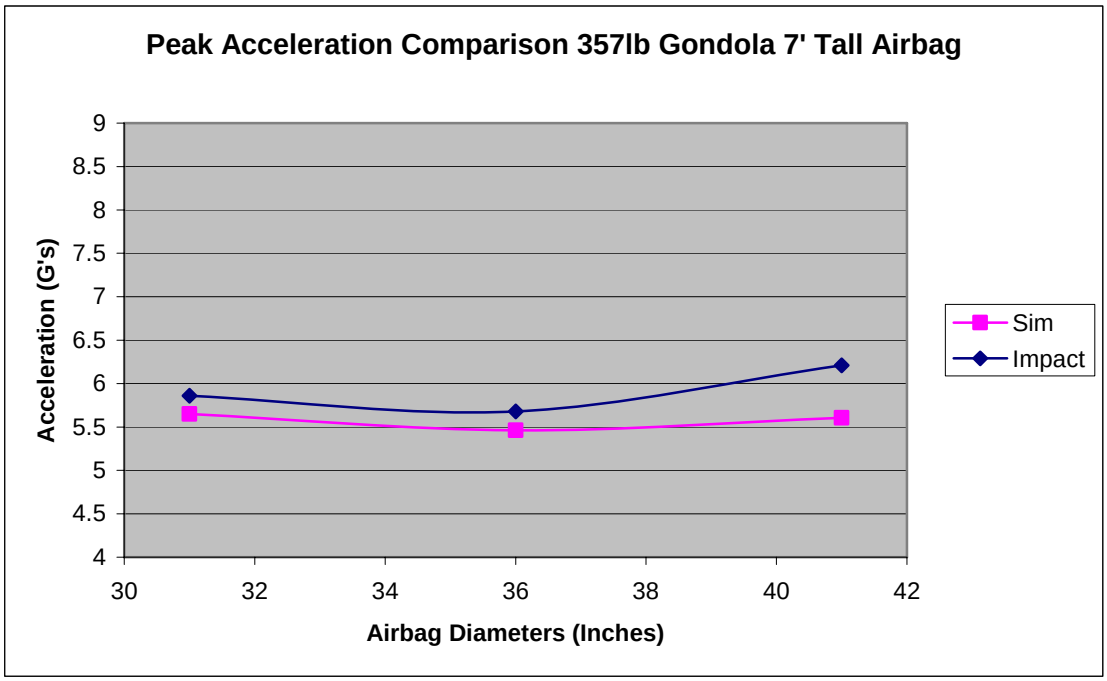

Figure 7-20: Peak Acceleration Comparisons 7-foot Tall Airbag

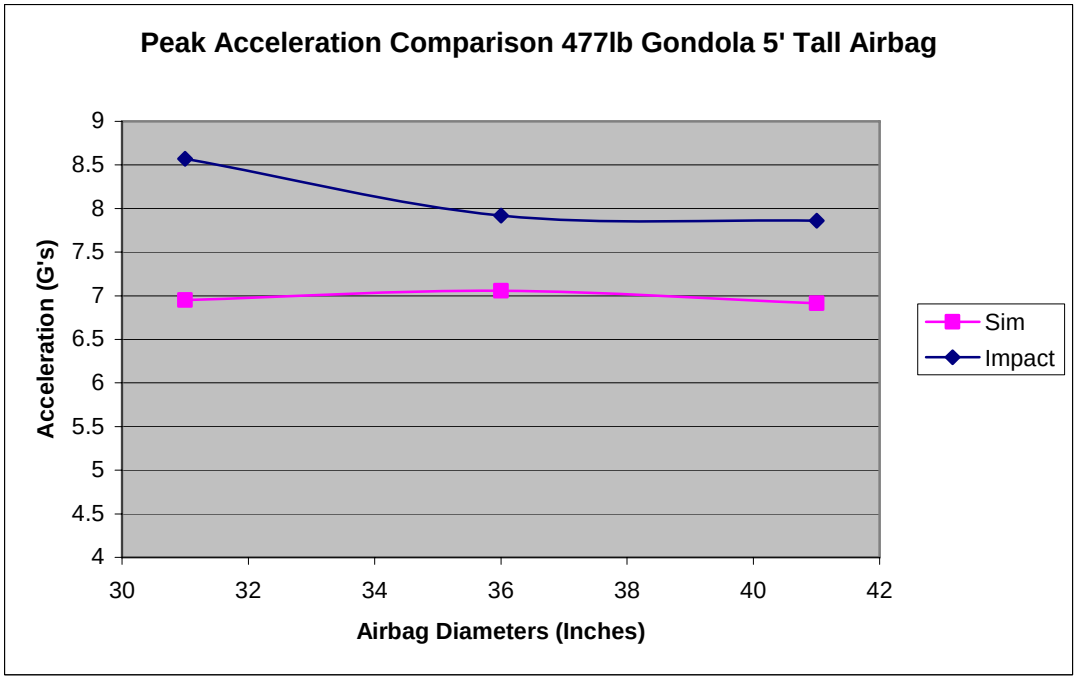

Figure 7-21: Peak Acceleration Comparisons 5-foot Tall Airbag

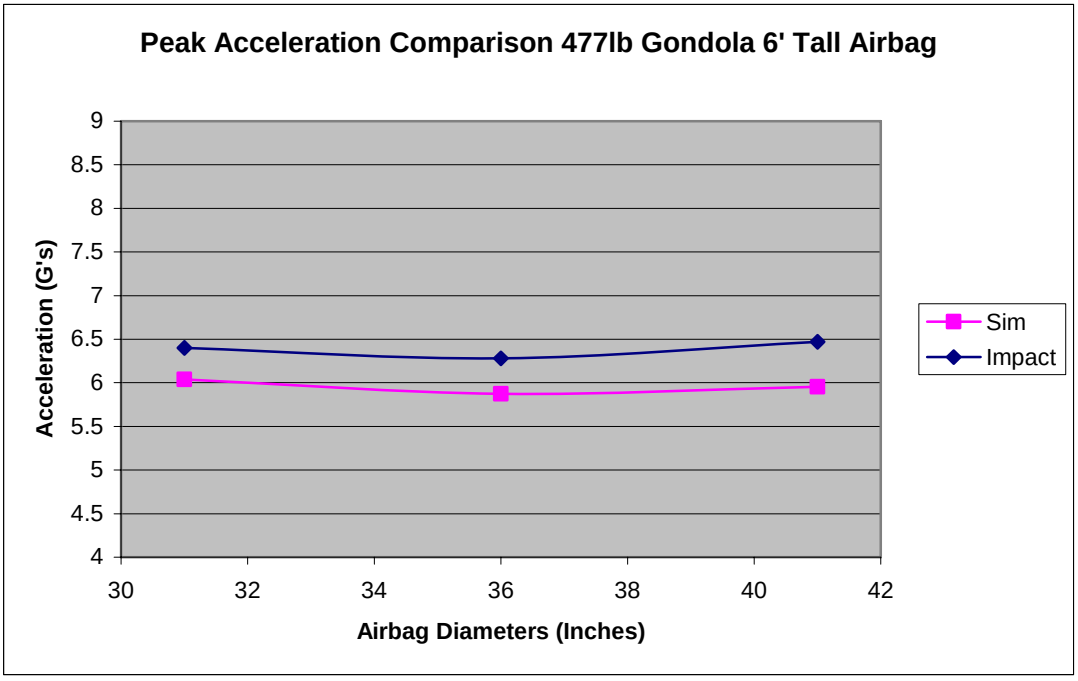

Figure 7-22: Peak Acceleration Comparisons 6-foot Tall Airbag

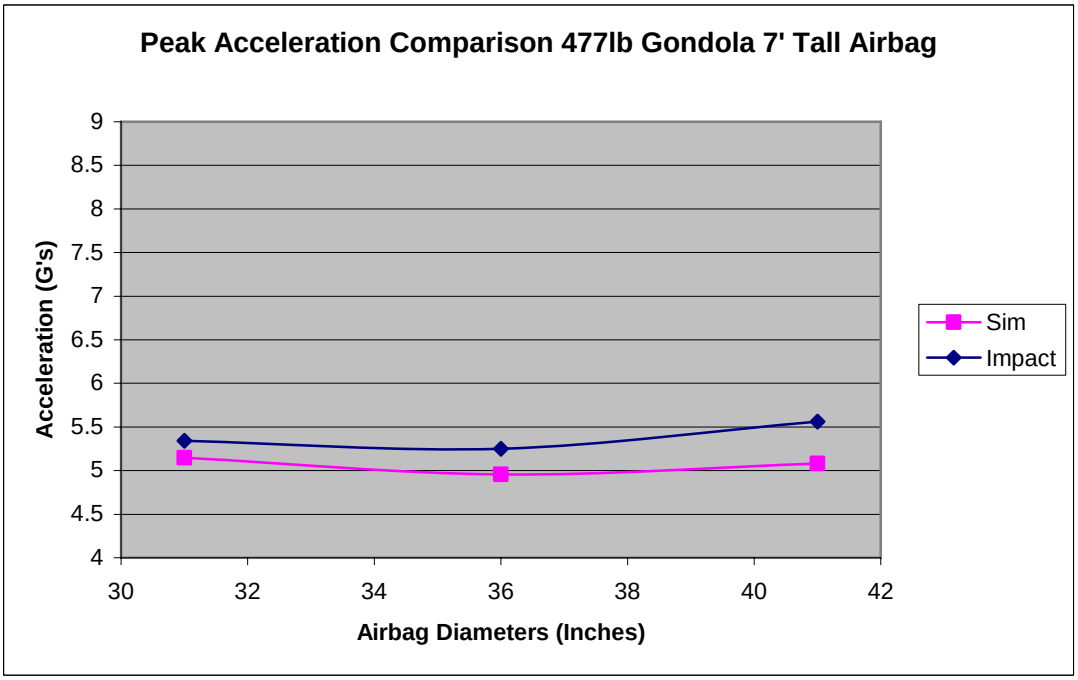

Figure 7-23: Peak Acceleration Comparisons 7-foot Tall Airbag

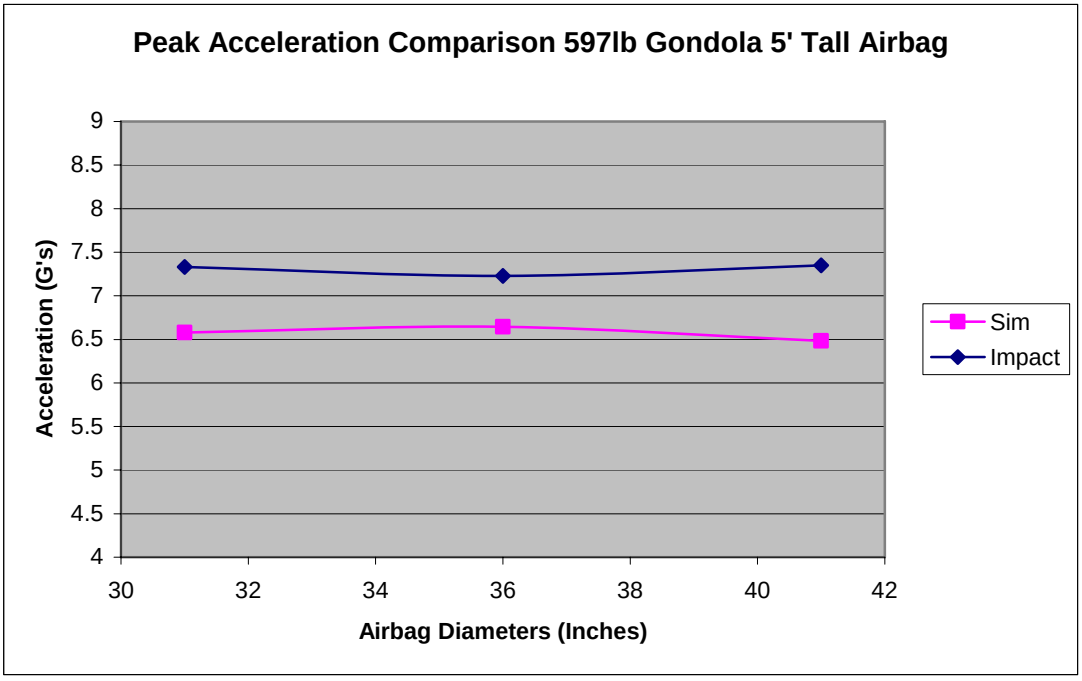

Figure 7-24: Peak Acceleration Comparisons 5-foot Tall Airbag

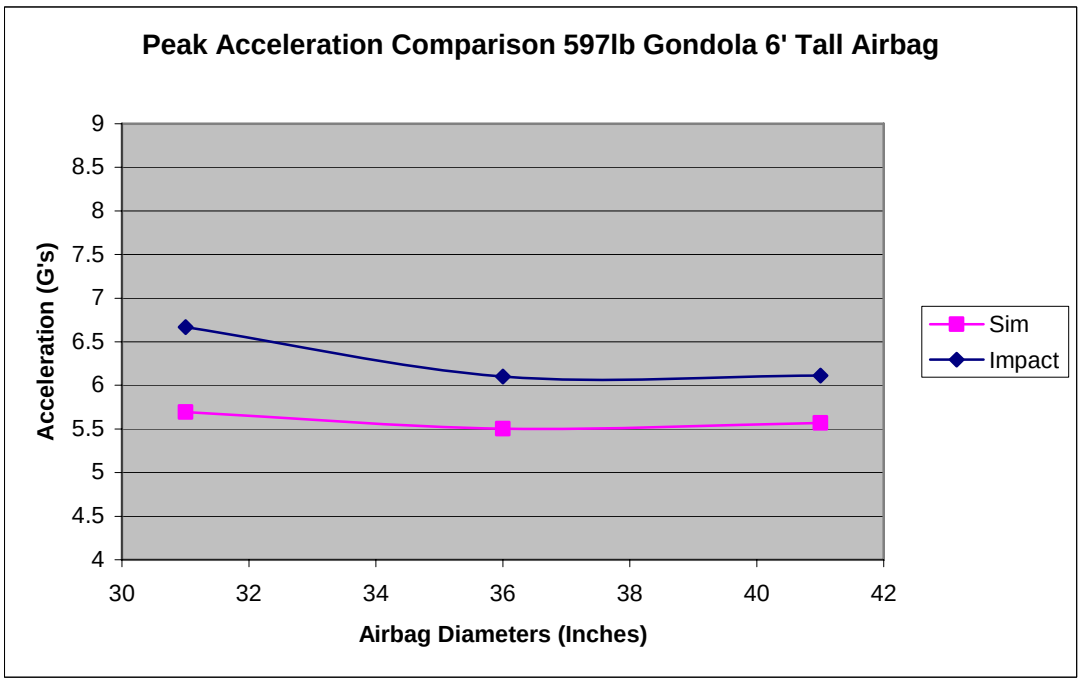

Figure 7-25: Peak Acceleration Comparisons 6-foot Tall Airbag

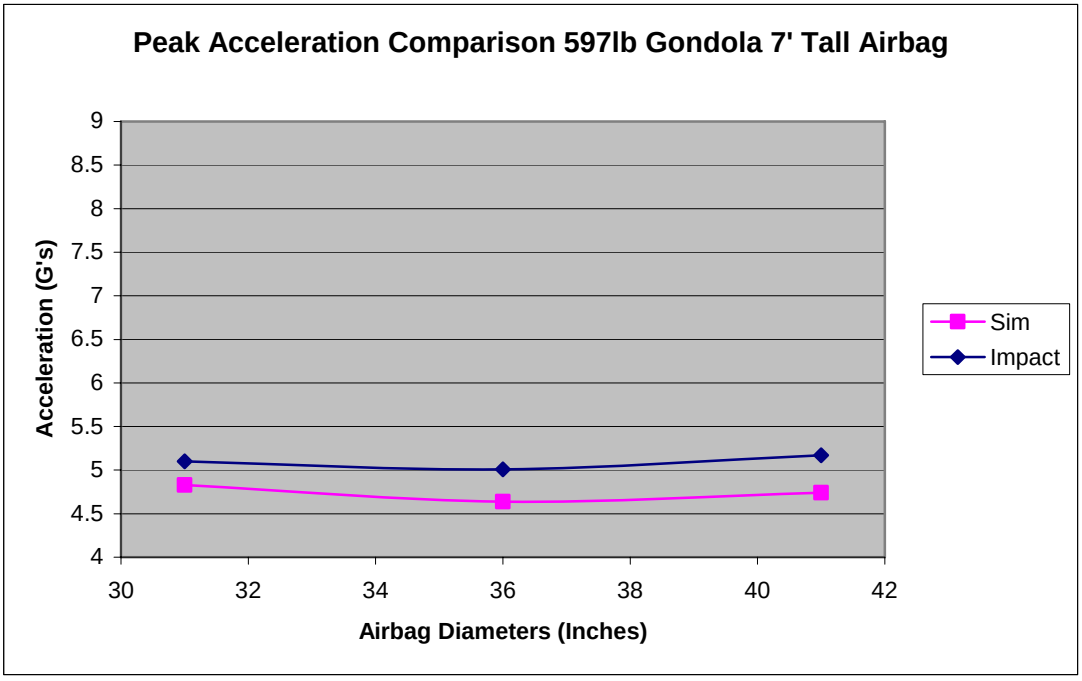

Figure 7-26: Peak Acceleration Comparisons 7-foot Tall Airbag

2. Peak Pressures.

The peak pressures predicted by the simulations were consistently lower than the experimental impact results. Table 7-2 shows the peak airbag pressures from simulations and impact experiments, the difference, and the percentage difference with the impact as the reference. The gondola for these experiments was the 1418 gondola, and the drop height was 15 feet. Figures 7-23 to 7-31 show these differences graphically.

Table 7-2: Comparison of Peak Pressures from the Simulation to the Drop Test

	Gondola 1418 Weight (lbs)											
	357				477				597			
Airbag	Sim	Exper	Diff.	Diff. %	Sim	Exper	Diff.	Diff. %	Sim	Exper	Diff.	Diff. %
3060	5.72	6.21	-0.491	-7.9	6.89	7.71	-0.82	-10.7	7.98	9.23	-1.25	-13.6
3660	4.75	4.95	-0.197	-4.0	5.72	6.11	-0.39	-6.4	6.61	7.19	-0.58	-8.0
4060	3.96	4.21	-0.252	-5.98	4.76	5.15	-0.39	-7.6	5.5	6.02	-0.52	-8.6
3072	5.22	5.39	-0.174	-3.23	6.30	6.55	-0.26	-3.9	7.31	7.78	-0.47	-6.0
3672	4.16	4.21	-0.045	-1.07	5.01	5.1	-0.09	-1.7	5.8	6.09	-0.29	-4.7
4072	3.55	3.61	-0.056	-1.56	4.28	4.39	-0.11	-2.4	4.96	5.14	-0.18	-3.4
3084	4.64	4.7	-0.059	-1.26	5.61	5.73	-0.12	-2.1	6.53	6.73	-0.2	-3.0
3684	3.66	3.53	0.129	3.67	4.42	4.31	0.107	2.5	5.13	5.06	0.07	1.4
4084	3.13	3.2	-0.073	-2.29	3.77	3.83	-0.06	-1.6	4.37	4.41	-0.04	-0.8

The simulation results regarding peak pressures were consistently lower than the drop test results, varying from 0.83% to 13.55% lower. The differences between the simulations and the drop tests on a percentage basis over the various airbags and gondola weights showed a major trend – fit improved as airbag height increased. The taller airbags spend a larger fraction of impact time in Phase 3 of impact. Of the remaining minor trends, the most significant one was that the airbags showed better fit as their diameter increased. The slopes and curvatures of the simulations and experiments match in every case.

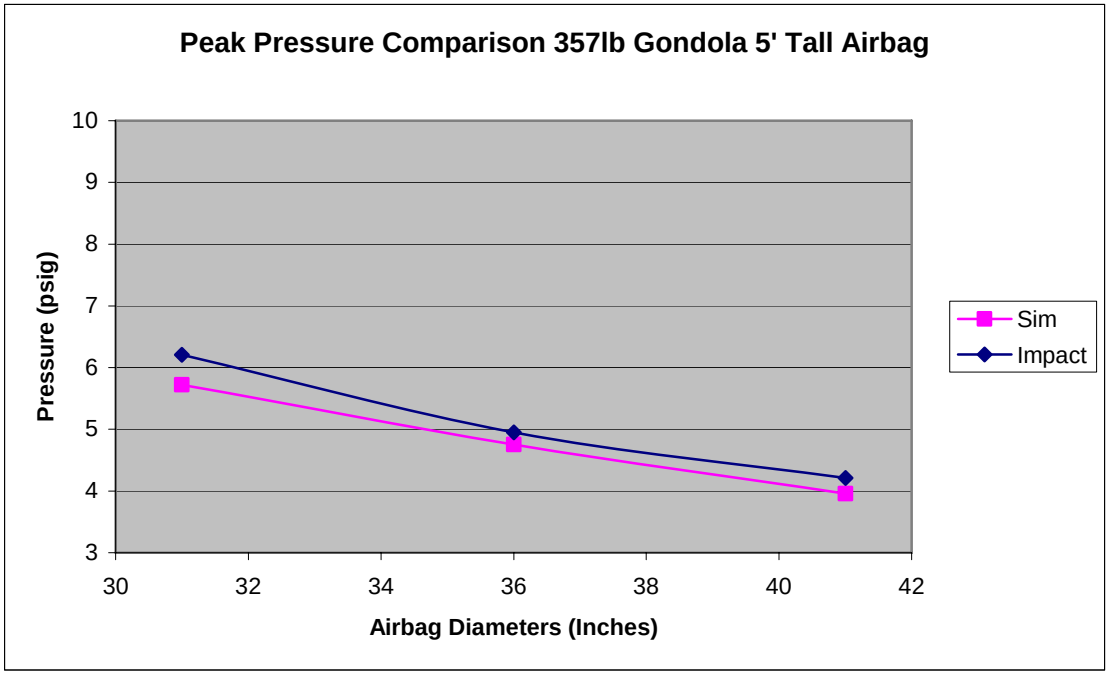

Figure 7-27: Peak Pressure Comparisons 5-foot Tall Airbag

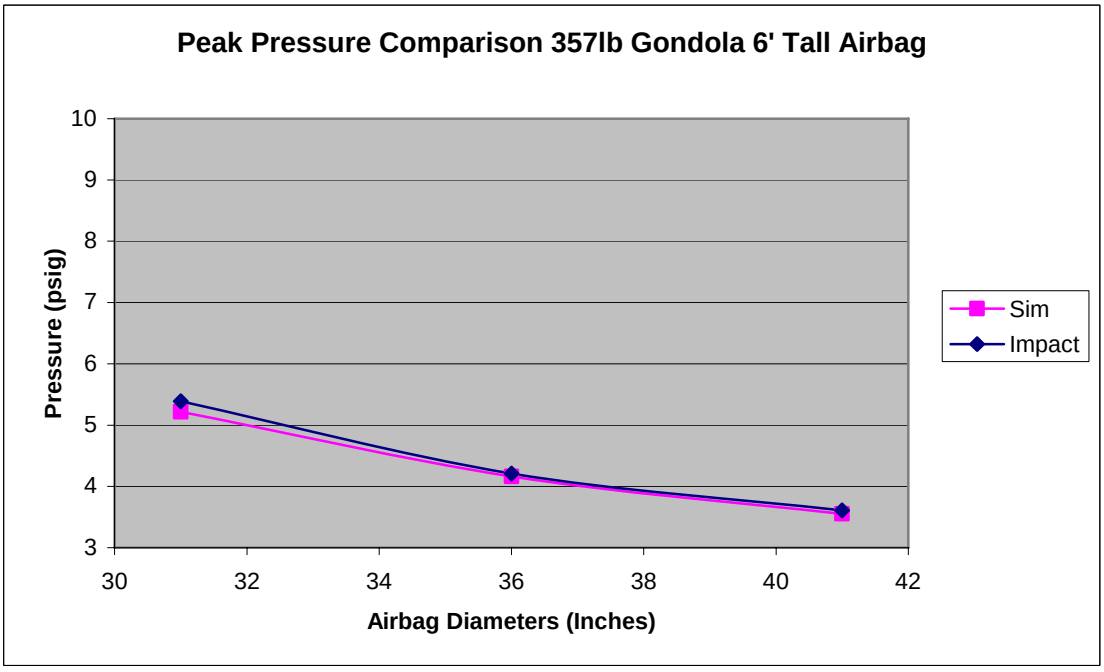

Figure 7-28: Peak Pressure Comparisons 6-foot Tall Airbag

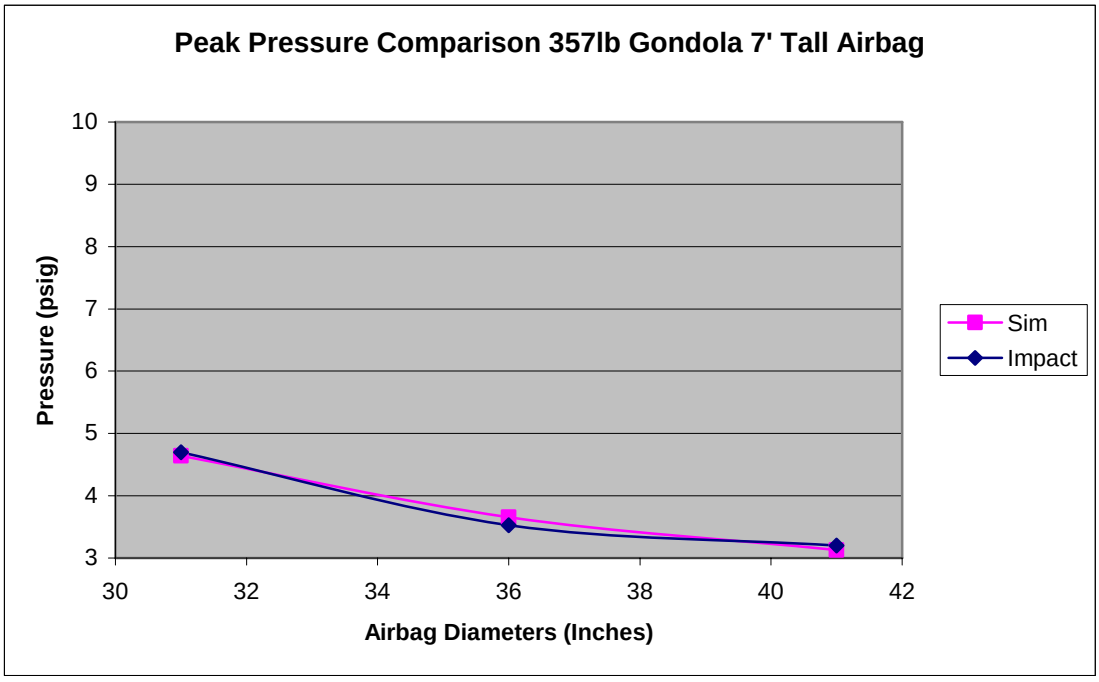

Figure 7-29: Peak Pressure Comparisons 7-foot Tall Airbag

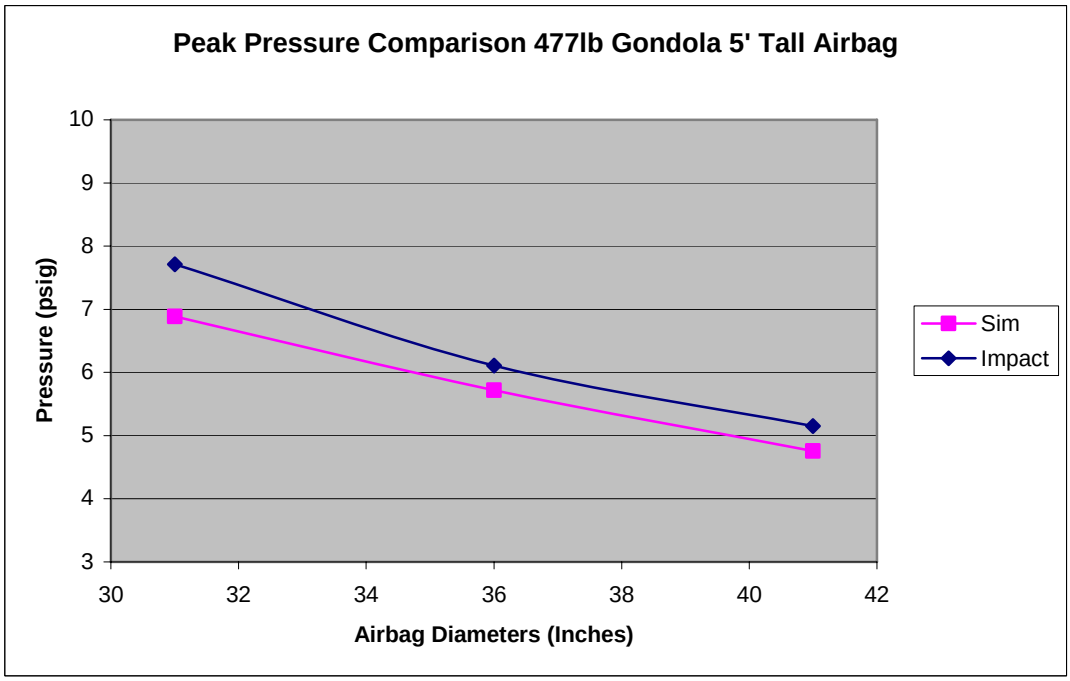

Figure 7-30: Peak Pressure Comparisons 5-foot Tall Airbag

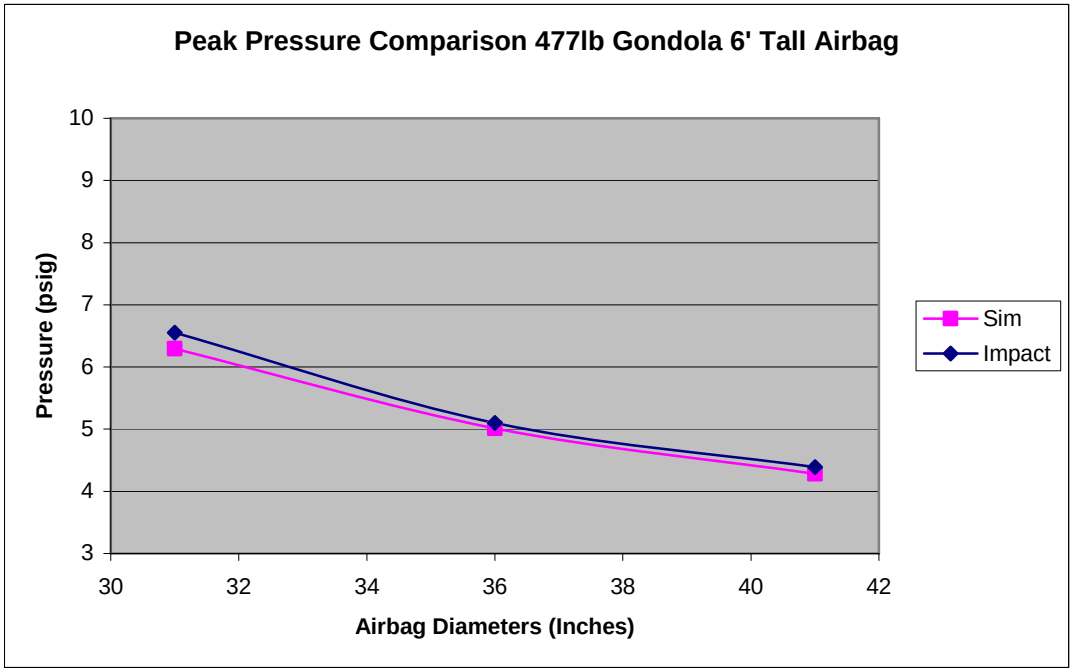

Figure 7-31: Peak Pressure Comparisons 6-foot Tall Airbag

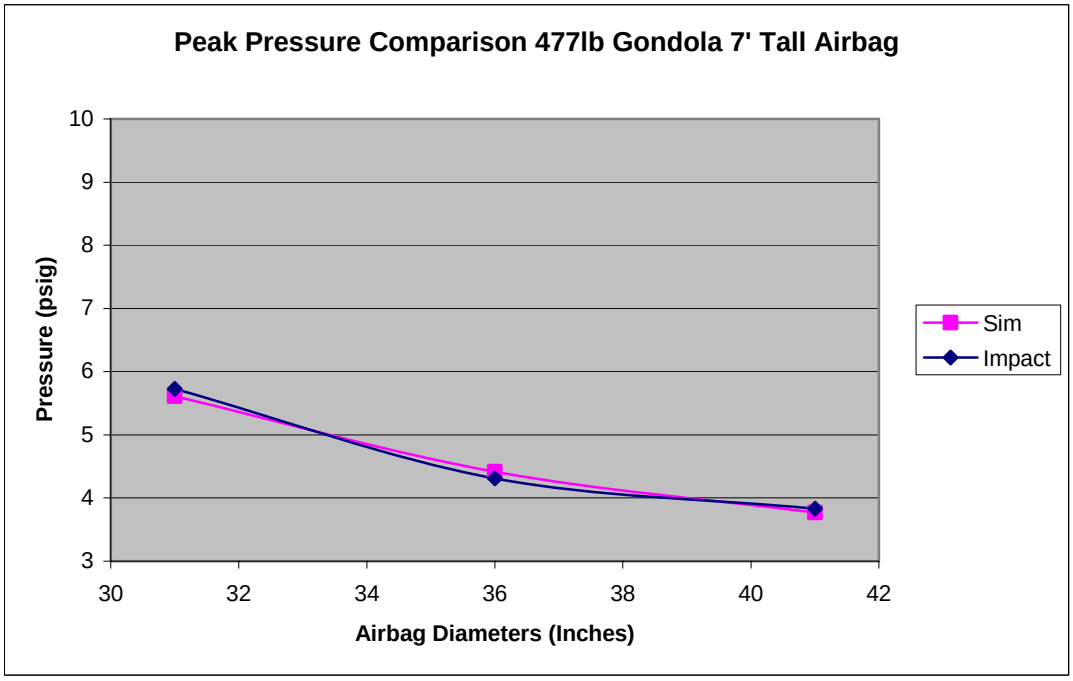

Figure 7-32: Peak Pressure Comparisons 7-foot Tall Airbag

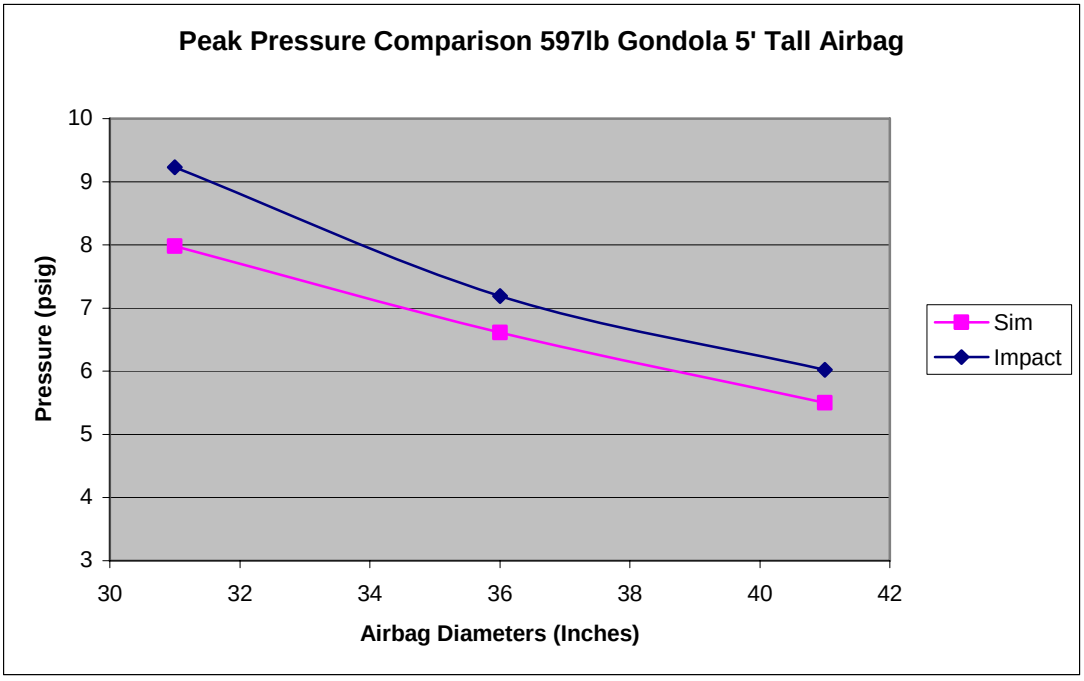

Figure 7-33: Peak Pressure Comparisons 5-foot Tall Airbag

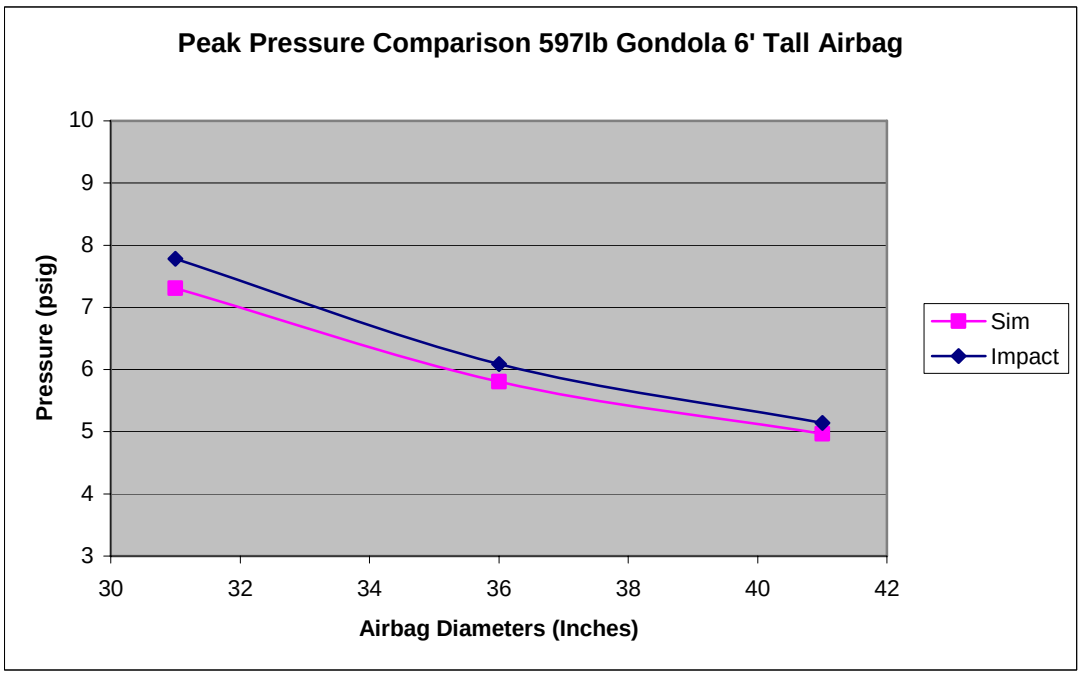

Figure 7-34: Peak Pressure Comparisons 6-foot Tall Airbag

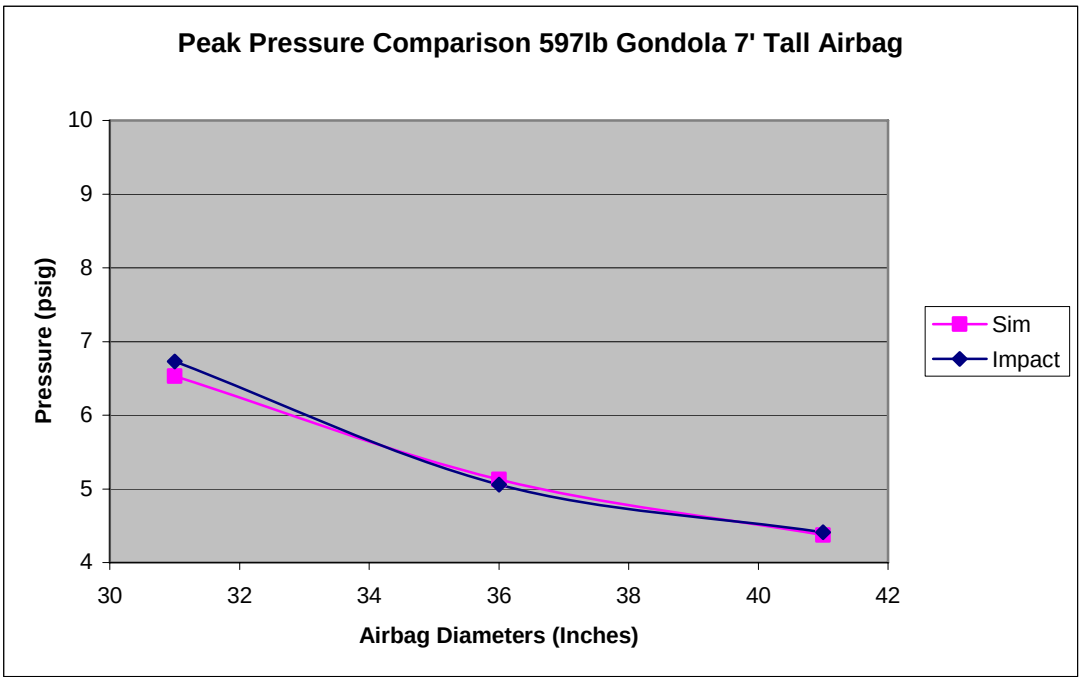

Figure 7-35: Peak Pressure Comparisons 7-foot Tall Airbag

All the initial conditions for the simulations and experiments described in this chapter are shown in Table 7-3 as a summary of inputs to the simulation. The elevation for the simulation is the top of the airbag when the collidant initially contacts it. The variation in these heights with each simulation is caused by the different initial airbag pressures producing more or less longitudinal stretch. The elevation for the experiments is the height of the image centroid of the flashlight, which was attached at the top of the gondola, relative to the bottom of the image frame at 16 milliseconds before the nadir in experimental airbag pressure. The variation in these elevations is larger than the simulations. These variations may be caused by inadvertent movement of the camera or ambiguity in determining time of contact from acceleration data.

Table 7-3: Initial Conditions for Simulation and Drop Test

Airbag & Wt	millisec	Psig.	In/sec	Elev Inch	Calc Elev
3084-357lb	1168	0.322	-250	137.25	86.11
3084-477lb	902	0.357	-251	137.49	86.12
3084-597lb	1010	0.395	-251	137.67	86.13
3072-357lb	994	0.324	-266	125.68	75.08
3072-477lb	1054	0.251	-267	125.22	75.07
3072-597lb	1152	0.346	-268	125.39	75.08
3060-357lb	1153	0.358	-274	120.15	62.85
3060-477lb	1122	0.297	-281	115.39	62.84
3060-597lb	1063	0.305	-277	119.27	62.84
3684-357lb	913	0.363	-240	139.19	87.28
3684-477lb	936	0.370	-237	140.26	87.28
3684-597lb	910	0.338	-247	135.91	87.28
3672-357lb	953	0.321	-257	131.86	76.27
3672-477lb	980	0.322	-258	131.59	76.27
3672-597lb	1078	0.319	-258	133.25	76.27
3660-357lb	949	0.308	-270	123.08	64.28
3660-477lb	1091	0.306	-273	121.63	64.28
3660-597lb	1065	0.334	-273	123.59	64.28
4084-357lb	941	0.392	-237	143.81	88.90
4084-477lb	964	0.371	-239	144.11	88.90
4084-597lb	1068	0.360	-237	145.40	88.89
4072-357lb	1042	0.396	-246	138.35	77.12
4072-477lb	977	0.388	-251	136.35	77.12
4072-597lb	1265	0.396	-253	135.42	77.12
4060-357lb	1101	0.396	-268	123.73	68.87
4060-477lb	1227	0.407	-272	122.00	68.87
4060-597lb	1130	0.397	-267	125.85	68.87

D. Summary

The simulations agreed fairly well with the experimental data in accuracy and trend. Peak collidant accelerations were within 20% and airbag pressures were within 14% of the drop test results at most. On average, accelerations differed by 8.7% and pressures by only 3.9%. The agreement could have been improved by modeling the initial dome at its top end of the airbag as an ellipse rather than a hemisphere. Duration of the impact event was modeled remarkably well with the simulation agreeing with the experiment within about 5%. The initial drop in pressure predicted by the simulation was much less

pronounced in the experiment. A 20 millisecond or so longer delay before a rise in pressure was observed in the experiment.

The longer airbags had better match between the simulation and experiments. A larger fraction of the dynamics was caused by Phase 3 impact with the longer airbags, leading one to believe that Phase 3 impact modeling was more faithful to the experiment than Phase 1 or 2. Phase 1 and 2 relied on an airbag geometry model that had a hemispherical dome on top and ignored the dome on the bottom of the airbag. This 4 inch high dome on the bottom may have a significant effect on Phase 1 and 2 dynamics by either collapsing or stretching during initial impact. The dome on the top of the airbag is more in the shape of an ellipse than a hemisphere. This shortness of height changes the timing and dynamics of Phase 1 and 2 initial impact. Modeling the upper dome as an ellipse would require changing the meridional radius r with meridional angle θ, as well as possibly changing the origin of r as Phase 2 progresses. Investigating these complications is left to future work.

The drop in gondola kinetic energy was 50% with the experiments but only 20% with the simulation. Since air leaking out of the airbag is the major source of dissipation, the simulation airbag permeability may be understated. Investigating this possibility is left to future work.

Chapter VIII: Conclusions and Recommendations

A. Conclusions

The most accurate airbag model compared to experimental results, and fastest airbag impact simulation relative to any extant in the literature, was developed. Experimental collidant rebound velocities exceeded the desired 15 feet/second munition ejection speed with airbag pressures below nine psig. Experimental collidant impact peak accelerations were below 18 G's, much less than the 50-G threshold for human injury for collisions up to 30 mph.

Major contributions were made to the understanding of low pressure airbags.

1. The most extensive publicly available data on impact response of low pressure airbags was collected. It provides a rich source of experimental data to design low pressure airbags.
2. A kinematically complex, yet low-order, math model of a permeable, elastic, cylindrical airbag was derived. It is offered as a candidate benchmark model to verify more complicated finite element or finite volume models. The resulting simulations of this model run in four to five processor minutes and provide an efficient tool suitable for design trade studies.
3. The experiments demonstrated that munition-ejection accelerations and safe collision decelerations are achievable with practical low-pressure airbags.

A total of 435 airbag collision tests were performed, a larger and more diverse set of experiments than any other in the literature. Conducting the world's most comprehensive set of public airbag experiments revealed new knowledge in airbag behavior. Trends

gleaned from the experiments provide guidance in determining the geometric parameters of an airbag design. Lengthening airbags reduced collidant peak accelerations and airbag peak pressures the most of any airbag parameter. Somewhat surprisingly, increasing airbag diameter had little effect on collidant peak accelerations but significantly reduced peak airbag pressures. Increasing collidant face areas increased peak accelerations and peak airbag pressures. For a given airbag, increasing collidant mass reduced peak accelerations but increased airbag peak pressures. Although not an airbag parameter trend, the experiment confirmed that increasing collidant impact velocities had the greatest effect on peak accelerations and peak pressures, increasing both, as expected.

The lesson for airbag engineers is that lengthening the airbag is the best way to reduce injuries. For ejectors, this lesson shows that a longer airbag stroke can achieve higher ejection speeds with equivalent or lower force on the projectile. In the case of a bomb bay, there is a stroke length limitation; but the airbag design should use the full stroke length.

The simulation results were closer to their drop test experimental results than any other simulations in the literature. On average, simulation peak accelerations were within 8.7% and peak pressures were within 3.9% of the experiments. Two thirds of the peak accelerations had single digit agreement between simulations and experiments. Only 6% of the airbag pressure simulations were more than 10% different from the experiments. A minor adjustment to initial contact times brings even closer agreement between the simulations and experiments. Using more realistic airbag permeabilities would also improve the fit.

The dynamic airbag model of the dissertation compared more favorably to experimental results than any of the model validations found in the literature. Moreover, it is validated over a larger range of experiments and with more parameters varied and tested. The airbag models in the literature that varied the most from their experiments had significant permeability or vent holes. The better performance of the dissertation's model is probably due to better permeability physics modeling. The dissertation has a realistic permeability model that accounts for actual leak areas, combined with reasonably accurate volume calculations based on assumed geometry, and reduction to an efficient 12 degree-of-freedom mathematical model. A key contribution was the insight that led to effectively integrating of multi-disciplinary equations into a model that captures the most important effects of a complex fluid-structure interaction problem.

The experimental measurements presented sources of error. Though most of the sensor noise was filtered out, the image analysis software added non-physical dynamics by moving the image centroid around inside the flashlight image when the image expanded beyond the centroid window.

The simulation model used simplifying assumptions that led to inaccuracies. Assuming the top of the airbag was a perfect hemisphere may explain distortions in Phase 1 and 2 of impact dynamics when the flattened dome may be better represented as an elliptical shape. Likewise, neglecting the dome on the bottom of the airbag was a modeling simplification but a distortion of reality. Accounting for the ballooning at the bottom of the airbag and more accurately representing dome flattening at the top of the airbag may reduce the simulation error. The airbag permeability affects the simulation significantly also. Some doubts about the air mass flow rates during the permeability

tests, as well as large difference between kinetic energy for the experiment versus the simulation, point to more accurate permeability measurements as a major means of affecting the simulation fit.

B. Recommendations

The airbag permeability tests should be rerun with a better apparatus. A 2-inch diameter fill pipe should be used, so all air flow velocities would be subsonic and hence more accurately measured. The Pitot static pressure sensor measuring vacuum should be a vacuum measurement sensor rather than a gauge pressure sensor operating off scale. The Pitot tube flow instrument should be calibrated against the OMEGA-Alicat-1400 compressible gas flow meter at the lower flow rates, or a high-flow meter should be used to measure mass flow directly.

The drop tests should be rerun with a better apparatus. A way to detect first contact between the gondola and the airbag should be developed. A small flashlight on the top of the airbag would indicate when the gondola hit it and provide an elevation for the top of the airbag. In this way, the initial conditions can be determined more accurately. Adding an accelerometer to the gondola would be a second source of acceleration data to the differentiation of the video displacement (especially since such differentiation is inherently noisy).

The math model should be improved to include the doming at the bottom of the airbags. Accounting for this phenomenon may reduce the fit error. A flatter dome on the top of the airbag might reduce errors in Phase 1 and 2 dynamics. Replacing the hemispherical dome with an elliptical dome may prove to more accurately capture the

volume changes that were less accurately modeled in Phase 1 and 2 than in Phase 3. Accounting for the varying stress and strain in the airbag dome would give more precise volumes and strain energies. This effect is assumed to be in the few percent region. Tracking wrapped or wrinkled fabric against the collidant would reduce the strain and stress in the unwrapped fabric. This effect is also assumed to be in the few percent region. The effect of wrapping and wrinkling was videoed for dozens of experiments. A grid was drawn on the dome of the airbag and filmed from above during impact. This effect is as yet not analyzed. Modeling the inflation process for an ejector application has yet to be done completely. This inflator needs to recreate the conditions in the airbag that were achieved during the collision rebounds on a timely basis.

In order to confirm the hypothesis that poor permeability modeling accounted for the large errors compared to experimental results in the literature, the proposed permeability properties from this research could be used in the high fidelity finite element simulations. Since LSDyna, for example, only permits permeability to be modeled as a simple function of pressure, the current permeability model, which also accounts for leak area, would have to be fit to a function of pressure *a priori*. Such a simulation might also lead to better understanding of Phase 1 and 2 geometries, if it proved more accurate.

Bibliography

Chapter I:

1-1 Hallquist, John. *LSDyna Theoretical Manual*. Livermore, CA: Livermore Software Technology Corporation, 1998.

Chapter II:

2-1 ---. *Catholic Encyclopedia: Joseph-Michel Montgolfier*. New York: New Advent Publishing, 1914.

2-2 Brown, Glenn, Roy Haggard, Brook Norton. "Inflatable Structures for Deployable Wings," AIAA, A01-29254 (2001).

2-3 Sherman, Donald. "Blink of an Eye," *Motor Trend*, v45 n5 (May 1993).

2-4 ---. "Air Bags Handle the Heavy Lifting," *Machine Design*, (October 21, 1999).

2-5 Ehrich, R.D. and J.R. Beaty. "Precision Delivery of Unguided Submunitions from a Tactical Standoff Missile," *AGARD Guidance, Control and Positioning of Future Precision Guided Stand-Off Weapons Systems*, (SEE N87-16000 08-15) (1986).

2-6 Taylor, Anthony P. "Investigation of the Application of Airbag Technology to Provide a Soft Landing Capability for Military Heavy Drop," AIAA, A01-29283 (2001).

2-7 Huxley-Reynard, C.S. "An Airbag Landing System for the Beagle2 Mars Probe," AIAA, A01-29306 (2001).

2-8 Brown, Glenn, Roy Haggard, and Brook Norton. "Inflatable Structures for Deployable Wings," AIAA, A01-29254 (2001).

2-9 Struttman, James. ""Inflatable Spaceborne Antenna Structures," *The Second Space Technology Alliance Workshop on Inflatable Structures*, Wright Patterson Air Force Base: (April 26, 2000).

2-10 ---. "Soft Landings," *Ward's Auto World* (June 2001).

2-11 Dreher, Peter A. "System for Collision Damage Reduction," *U.S. Patent & Trademark Office.* #6,106,038 (August 2000).

2-12 Strother, Charles and Richard Morgan. "The Efforts of the National Highway Traffic Safety Administration in the Development of Advanced Passive Protection Systems and Child Restraint Systems," *SAE Conference*

Proceedings P-53. Santa Monica CA: The RAND Corporation Reports 740580, 1974.

2-13 ---. "Federal Motor Vehicle Safety Standard 208," *49 Code of Federal Regulations Chapter V (10-1-02 Edition) Section 571.208*.

2-14 Nefske, Donald. "A Basic Airbag Model," *SAE 2nd International Conference on Passive Restraints*. Detroit, MI: Society of Automotive Engineers 720426, May 22, 1972.

2-15 King, Howard A.; Sneden, Kilian. "Weapon Integration: Key to the 'Clean Machine'," *Aerospace America,* AIAA, August 1984.

2-16 Vendetti, Vince. "Preliminary Compressed Air Dispense Simulator", Naval Surface Warfare Center, Dahlgren Division. Dahlgren, VA: Technical Report, September 2003.

2-17 Malcolm, David J., Peter G. Glockner. "Collapse by Ponding of Air-Supported Membranes," *Journal of the Structural Division, Proceedings of the American Society of Civil Engineers.* Vol. 104, No. ST9, September 1978.

2-18 Szyszkowski, W., P.G. Glockner. "Finite Deformation and Stability Behavior of Spherical Inflatables Under Axi-Symmetric Concentrated Loads," *International Journal of Non-Linear Mechanics.* Pergamon Press Ltd., Great Britain, Vol. 19, No. 5, 1984.

2-19 Nieboer, J.J., Wismans, J., de Coo, P.J.A. "Airbag Modeling Techniques," *SAE (Society of Automotive Engineers) Transactions*, v 99, n Sect 6, 1990, p 1855-1870

2-20 Bruijs, W.E.M., de Coo, P.J.A., Ashmore, R.J., Giles, A.R. "Airbag Simulations with the Madymo FEM Module," *SAE Special Publications*, n 906, *Analytical Modeling and Occupant Protection Technologies*, 1992, p 19-27

2-21 Fitzpatrick, Michael U., Thompson, Kelly E. "PASSIM-PLUS, a Multi-element, Passenger Airbag Model," *SAE Technical Paper Series*, 1991, 12p

2-22 Cooper, Michelle, Sinclair, Robert, Sanders, John, Frigerio, Jacapo. "Design and testing of an airbag landing attenuator system for a generic crew return vehicle," *Collection of Technical Papers - 18th AIAA Aerodynamic Decelerator Systems Technology Conference and Seminar, Collection of Technical Papers - 18th AIAA Aerodynamic Decelerator Systems Technology Conference and Seminar*, 2005, p 146-168

2-23 He, Wen, Zhong, Zhihua, Yang, Jikuang. "Research on experimental validation of computer simulation of working performance of automobile airbag," *Jixie*

Gongcheng Xuebao/Chinese Journal of Mechanical Engineering, v 38, n 4, April, 2002, p 126-129

2-24 Xiao, Fan, Wang, Hong-Yan. "Numeration of occupant with restriction system's dynamic response in frontal impact," *Tongji Daxue Xuebao/Journal of Tongji University*, v 32, n 9, September, 2004, p 1220-1224

2-25 Wawa, Charles J., Chandra, Jim S., Verma, Mukul K. "Implementation and validation of a finite element approach to simulate occupant crashes with airbags: Part I - airbag model," *American Society of Mechanical Engineers, Applied Mechanics Division, AMD*, v 169, *Crashworthiness and Occupant Protection in Transportation Systems*, 1993, p 269-286

2-26 Wawa, Charles J., Chandra, Jim S., Verma, Mukul K. "Implementation and validation of a finite element approach to simulate occupant crashes with airbags: Part II - airbag coupling with crash victim," *American Society of Mechanical Engineers, Applied Mechanics Division, AMD*, v 169, *Crashworthiness and Occupant Protection in Transportation Systems*, 1993, p 287-309

2-27 Mu, William, Sheng, Jianping, Chen, Chao. "Relationship of driver airbag design parameters to an out-of-position small female thorax injury," *American Society of Mechanical Engineers, Applied Mechanics Division, AMD*, v 237, 1999, p 219-231

2-28 Kim, Hyunsun, Kirby, Bryn P. D. "Investigation of external airbags for rotorcraft crashworthiness," *Journal of Aircraft*, v 43, n 3, May/June, 2006, p 809-816

2-29 Lakshminarayan, V., Lasry, David. "Finite element simulation of driver folded air bag deployment," *SAE (Society of Automotive Engineers) Transactions*, v 100, n Sect 6, 1991, p 1969-1977

2-30 Matsumoto, Hiroyuki, Sakakida, Masafumi, Kurimoto, Koji. "Parametric evaluation of vehicle crash performance," *SAE (Society of Automotive Engineers) Transactions*, v 99, n Sect 6, 1990, p 635-646

2-31 Hoffmann, Rainer, Ulrich, Dirk, Protard, Jean-Baptiste, Wester, Harald, Jaehn, Norbert, Scharnhorst, Thomas. "Finite element analysis of occupant restraint system interaction with PAM-CRASH," *SAE (Society of Automotive Engineers) Transactions*, v 99, n Sect 6, 1990, p 1901-1912

2-32 Lu, Zi, Chan, Philemon. "Finite Element Simulation Study of Airbag Load Phenomena," SAE 2005-01-0301, *SAE Technical Papers*, 2005

2-33 Personal communication with Mr. Steven Pitroff, Chief Airbag Engineer, Delphi Corporation.

Chapter III:

3-1 Fox, Robert, McDonald, Alan. *Introduction to Fluid Mechanics.* New York, John Wiley & Sons, 1973. pg 530

3-2 Saad, Michel. *Compressible Fluid Flow: 2nd Edition.* Englewood Cliffs, NJ: Prentice Hall, 1993.

3-3 Tsai, Stephen, H. Thomas Hahn. *Introduction to Composite Materials.* Westport, CT: Technomic Publishing, 1980. pg 17

Chapter IV:

4-1 Martins, Joaquim, Sturdza, Peter, Alonso, Juan. "The Connection between the Complex Step Derivative Approximation and Algorithmic Differentiation," AIAA-2001-0921, 2001.

Chapter V:

5-1 www.ni.com/labview/

5-2 Cengel, Yunus. *Introduction to Thermodynamics and Heat Transfer.* McGraw-Hill, New York, NY, 1997.

5-3 Popov, E. P. *Mechanics of Materials, 2nd Edition.* Prentice-Hall, Englewood Cliffs, NJ, 1976.

Chapter VI:

6-1 www.endevco.com/products

6-2 www.photron.com

6-3 Myers, Raymond, Douglas Montgomery. *Response Surface Methodology.* New York: John Wiley & Sons, 1995.

6-4 Neter, John, William Wasserman, G.A. Whitmore. *Applied Statistics.* Boston: Allyn & Bacon, 1978.

Chapter VII:

7-1 *MATLAB Math for Use with MATLAB.* Natick, MA, The MathWorks, Inc., 2006.

APPENDIX A

A. Pore Flow Resistance Force

The shear force on the fabric pore is caused by compressible flow with friction through the pores based on Fanno flow equations. The force acting on the pores is the shear force on the edge of the pores of the viscous gas blowing by – so called compressible flow with friction. Dr. Fanno modeled this type of flow, and it now bears his name. Fanno flow equations provide a flow resistance force R_x applied to the walls of the channel. Figure A-1 shows a fabric pore and its control volume, through which Fanno flow applies.

From [3-1], R_x is a function of pressure drop across the pore and the mass flow rate times the change in velocity across the pore.

$$R_x = (P_p - P_a)A_p + \dot{m}(u_a - u_p) \tag{A-1}$$

The subscripts indicate the airbag inside surface of the pore with *p* and the outside surface with *a* where the static pressure is atmospheric.

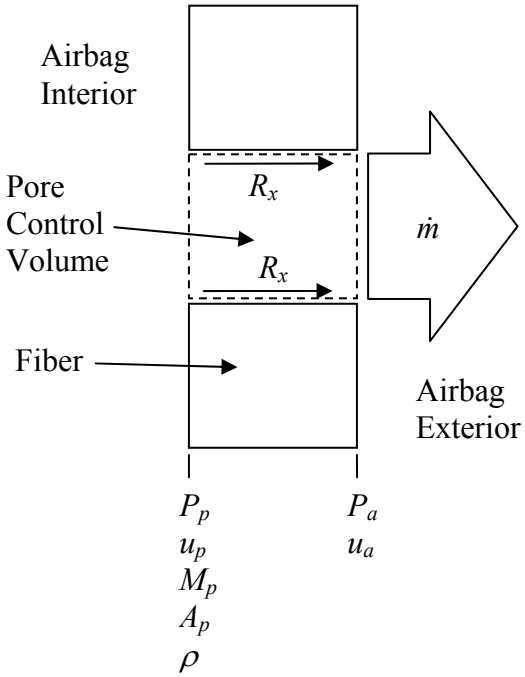

Figure A-1: Fanno Flow through the Airbag Pore

The remaining unknown in Equation (A-1) is the pore exit flow velocity u_a. From [3-2], the pore exit flow velocity u_a is a function of Mach number M_a at the pore exit and the critical velocity u^* at an imaginary exit in a Fanno conduit long enough to achieve Mach 1, where the asterisk indicates properties at Mach 1.

$$u_a = u^* \sqrt{\frac{\gamma+1}{2+(\gamma-1)M_a^2}}\, M_a \tag{A-2}$$

The γ is the ratio of specific heats, 1.4 for an Ideal Gas, typical of airbags. The critical velocity u^* can be calculated from the pore entrance conditions.

$$u^* = \frac{u_p \sqrt{\frac{2+(\gamma-1)M_p^2}{\gamma+1}}}{M_p} \tag{A-3}$$

Pore exit Mach number is a function of pore entrance Mach number and the ratio of the known pressures.

$$\frac{P_a}{P^*} = \frac{1}{M_a}\sqrt{\frac{\gamma+1}{2+(\gamma-1)M_a^2}} = \frac{P_a}{P_p}\frac{P_p}{P^*} = \frac{P_a}{P_p}\left(\frac{1}{M_p}\sqrt{\frac{\gamma+1}{2+(\gamma-1)M_p^2}}\right) \tag{A-4}$$

Since the properties at the pore entrance are known, the equation is rearranged to be a quadratic in M_a. The lowest positive real root is the only practical answer.

$$M_a = \sqrt{\frac{-b+\sqrt{b^2+\gamma^2-1}}{b(\gamma-1)}} \quad \text{where } b = \frac{P_a}{P_p}\left(\frac{1}{M_p}\sqrt{\frac{\gamma+1}{2+(\gamma-1)M_p^2}}\right) \tag{A-5}$$

The resulting expanded equation for u_a is

$$u_a = u_p\sqrt{\frac{\frac{2}{M_p^2}+\gamma-1}{\frac{2}{M_a^2}+\gamma-1}} \tag{A-6}$$

Substituting back into the flow resistance equation (A-10) yields

$$R_x = (P_a - P_p)A_p + \dot{m}u_p\sqrt{\frac{\frac{2}{M_p^2}+\gamma-1}{\frac{2}{M_a^2}+\gamma-1}} \tag{A-7}$$

where P_p is known from Equation (3-13) and u_p is known from Equation (3-5).

B. Dynamic System of the Fabric and Collidant

To find the longitudinal stress, a model was made of the dynamic system of the fabric and collidant. Longitudinal strain energy in the airbag is part of the potential energy of a dynamic system comprising the airbag and the collidant but not the air inside or outside of the airbag. This Fabric-Mass system is shown in Figure A-2.

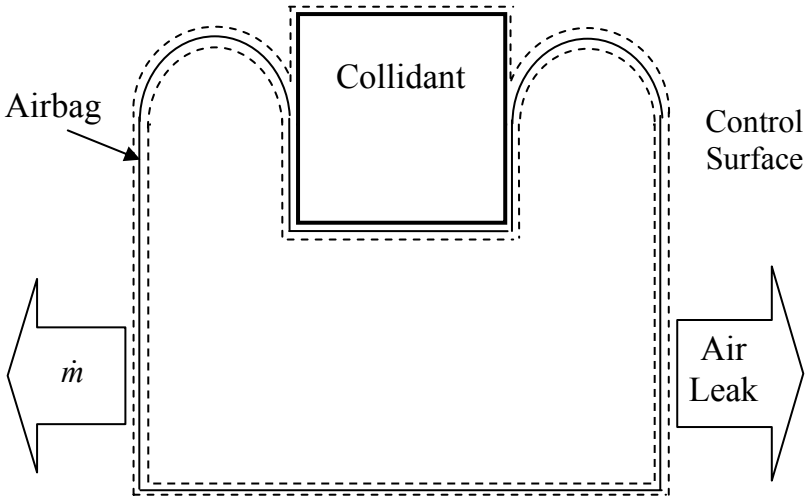

Figure A-2: Dynamic System of Airbag and Collidant

The energy equation for the Fabric-Mass system has external work applied to it by gage pressure inside the airbag times its change in volume plus the shear work of the air escaping through the pores. The energy inside the system is the strain energy of the airbag, Π, as well as the kinetic and potential energy of the collidant, since the airbag mass is negligible.

a. Work Applied to the Dynamic System.

The $P\delta V$ boundary work in Equation (A-8) is negative during compression, with pressure increasing as volume decreases in the inelastic case. It reduces kinetic energy of the collidant; therefore, the sign of $P\delta V$ on the left side of the energy equation is positive. This boundary work does not act on the unblocked pores, hence it applies to the moving surface areas, A_{Lf} and A_{face}, excluding the pore area, even though δV applies to all the moving surface areas, A_L and A_{face}. The boundary work is adjusted appropriately.

Flow through the pores applies a shear force on the fabric adjoining the pores in the direction of the flow and in the direction of the fabric motion (increasing volume); hence

it behaves in the same direction as $P\delta V$, and it, too, is positive on the left hand side of the energy equation. Hence

$$P_g \delta V \frac{A_{Lf} + A_{face}}{A_L + A_{face}} + \delta W_{shear} = \frac{1}{2} M \dot{z}^2 + Mgz + \Pi \tag{A-8}$$

The shear work is caused by compressible flow with friction through the pores based on Fanno flow equations. The Fanno flow provides a flow resistance force R_x. This force times the control surface average displacement is the approximate shear work. The shear work actually only results from the displacement of the leak area, but lacking a simple way to calculate this displacement, we use average boundary displacement.

$$\delta W_{shear} = R_x \frac{\delta V}{A_L + A_{face}} \tag{A-9}$$

R_x was defined in Equation (A-7), hence

$$\delta \dot{W}_{shear} = \left[(P_p - P_a) A_p + \dot{m} u_p \left(\sqrt{\frac{2}{(\gamma - 1) M_p^2} + 1} \sqrt{\frac{-2b}{b + \sqrt{b^2 + \gamma^2 - 1}} + 1} - 1 \right) \right] \frac{\dot{V}}{A_L + A_{face}} \tag{A-10}$$

Though the rate of shear work is not a function of longitudinal stress, it is a function of airbag pressure P via the pore pressure and Bernoulli's equation.

The left hand side of the energy equation (A-8) expands to an equation where definition of the coefficient P_f is convenient for future calculations.

$$P_g \delta V \frac{A_{Lf} + A_{face}}{A_L + A_{face}} + R_x \frac{\delta V}{A_L + A_{face}} = \frac{P_g \left(A_{Lf} + A_{face} \right) + R_x}{A_L + A_{face}} \delta V = P_f \delta V \tag{A-11}$$

b. Fabric Strain Energy.

Fiber strain energy is different in the leak area A_L from the collidant contact area A_C. In the leak area of the fabric, both hoop stress and longitudinal stress are active. In the collidant contact area of the fabric, the fabric is unloaded in the hoop direction as it folds

around the collidant, but remains taught in the longitudinal direction; hence longitudinal stress remains active, though hoop stress does not. Because of the single direction of stress in the collidant side contact area, the strain equation is only $\varepsilon_{side} = \sigma_L / E_L$. The strain energy is only $\left(\sigma_L^2 / 2E_L\right) tA_{side}$.

On the bottom face of the collidant, the longitudinal stresses cross the face orthogonally, hence causing a Poisson effect and doubling the strain energy on the face. Because of the active Poisson effect in the collidant bottom face contact area, the strain equation in one direction is $\varepsilon_{face} = \sigma_L \left(1 - \nu_L\right) / E_L$. The total face area strain energy is $\left(\sigma_L^2 \left(1 - \nu_L\right) / E_L\right) tA_{face}$.

As a first-order approximation to this total fabric strain energy, the strain energies are integrated over the fiber leak area and the fiber contact area, multiplied by fabric thickness, and averaged over the range of total strain and assumed uniform over their respective areas.

$$\begin{aligned}\Pi &= \frac{1}{2} t \left[\int_{A_{Lf}} \left(\sigma_H \varepsilon_H + \sigma_L \varepsilon_L\right) dA + \int_{A_{side}} \sigma_L \varepsilon_{side} dA + 2 \int_{A_{face}} \sigma_L \varepsilon_{face} dA \right] \\ &= \frac{t}{2} \left(\left(\sigma_H \varepsilon_H + \sigma_L \varepsilon_L\right) A_{Lf} + \sigma_L \left(\varepsilon_{side} A_{side} + 2 \varepsilon_{face} A_{face} \right) \right) \\ &= \frac{t}{2} \left(\left(\sigma_H \varepsilon_H + \sigma_L \varepsilon_L\right) A_{Lf} + \frac{\sigma_L^2}{E_L} \left(A_{side} + 2\left(1 - \nu_L\right) A_{face} \right) \right)\end{aligned} \qquad \text{(A-12)}$$

c. Differential Form of Energy Equation.

The differential form of the energy Equation (A-8) reveals

$$P_f \dot{V} = M \left(g + \ddot{z}\right) \dot{z} + \dot{\Pi} \qquad \text{(A-13)}$$

The strains are detailed with the constitutive equation (3-12). Expanding fabric strain energy rate yields

$$\dot{\Pi} = \frac{t}{2}\Big[\left(\dot{\sigma}_H\varepsilon_H + \sigma_H\dot{\varepsilon}_H + \dot{\sigma}_L\varepsilon_L + \sigma_L\dot{\varepsilon}_L\right)A_{Lf} + \left(\sigma_H\varepsilon_H + \sigma_L\varepsilon_L\right)\dot{A}_{Lf}$$
$$+ \frac{2\sigma_L\dot{\sigma}_L}{E_L}\left(A_{side} + 2\left(1-\nu_L\right)A_{face}\right) + \frac{\sigma_L^2}{E_L}\left(\dot{A}_{side} + 2\left(1-\nu_L\right)\dot{A}_{face}\right)\Big]$$
$$= \frac{t}{2}\Bigg[\left(\dot{\sigma}_H\varepsilon_H + \sigma_H\left(\frac{\dot{\sigma}_H}{E_H} - \frac{\dot{\sigma}_L\nu_L}{E_L}\right) + \dot{\sigma}_L\varepsilon_L + \sigma_L\left(\frac{\dot{\sigma}_L}{E_L} - \frac{\dot{\sigma}_H\nu_H}{E_H}\right)\right)A_{Lf}$$
$$+ \dot{A}_{Lf}\left(\sigma_H\varepsilon_H + \sigma_L\varepsilon_L\right) + \frac{2\sigma_L\dot{\sigma}_L}{E_L}\left(A_{side} + 2\left(1-\nu_L\right)A_{face}\right) + \frac{\sigma_L^2}{E_L}\left(\dot{A}_{side} + 2\left(1-\nu_L\right)\dot{A}_{face}\right)\Bigg] \tag{A-14}$$

Collecting the time derivatives

$$\dot{\Pi} = \frac{t}{2}\Bigg[\dot{\sigma}_H A_{Lf}\left(\varepsilon_H + \frac{\sigma_H}{E_H} - \frac{\sigma_L\nu_H}{E_H}\right) + \dot{\sigma}_L A_{Lf}\left(\varepsilon_L + \frac{\sigma_L}{E_L} - \frac{\sigma_H\nu_L}{E_L}\right)$$
$$+ \dot{\sigma}_L\frac{2\sigma_L}{E_L}\left(A_{side} + 2\left(1-\nu_L\right)A_{face}\right) + \dot{A}_{Lf}\left(\sigma_H\varepsilon_H + \sigma_L\varepsilon_L\right) + \frac{\sigma_L^2}{E_L}\left(\dot{A}_{side} + 2\left(1-\nu_L\right)\dot{A}_{face}\right)\Bigg] \tag{A-15}$$

From Ref [3-Tsai-p17], $\nu_H / E_H = \nu_L / E_L$, which allows use of the constitutive equation to simplify further.

$$\dot{\Pi} = A_{Lf}t\left(\dot{\sigma}_H\varepsilon_H + \dot{\sigma}_L\varepsilon_L\right) + \dot{\sigma}_L\frac{\sigma_L}{E_L}t\left(A_{side} + 2\left(1-\nu_L\right)A_{face}\right)$$
$$+ \dot{A}_{Lf}\frac{t}{2}\left(\sigma_H\varepsilon_H + \sigma_L\varepsilon_L\right) + \frac{\sigma_L^2}{E_L}\frac{t}{2}\left(\dot{A}_{side} + 2\left(1-\nu_L\right)\dot{A}_{face}\right) \tag{A-16}$$

Substituting back into the differential form of the energy equation

$$P_f\dot{V} = M\left(g + \ddot{z}\right)\dot{z}$$
$$+ A_{Lf}t\left(\dot{\sigma}_H\varepsilon_H + \dot{\sigma}_L\varepsilon_L\right) + \dot{\sigma}_L\frac{\sigma_L}{E_L}t\left(A_{side} + 2\left(1-\nu_L\right)A_{face}\right) \tag{A-17}$$
$$+ \dot{A}_{Lf}\frac{t}{2}\left(\sigma_H\varepsilon_H + \sigma_L\varepsilon_L\right) + \frac{\sigma_L^2}{E_L}\frac{t}{2}\left(\dot{A}_{side} + 2\left(1-\nu_L\right)\dot{A}_{face}\right)$$

Before collecting terms of $\dot{\sigma}_L$, two other unknowns are defined. The hoop stress rate is a function of airbag pressure rate and longitudinal stress rate found by differentiating Equation (A-17).

$$\begin{aligned}\dot{\sigma}_H &= \frac{\dot{P}_g R_0 \left(E_H - \nu_H \sigma_L\right) + P_g R_0 \left(E_H - \nu_H \dot{\sigma}_L\right)}{E_H t - P_g R_0} + \frac{\dot{P}_g P_g R_0^2 \left(E_H - \nu_H \sigma_L\right)}{\left(E_H t - P_g R_0\right)^2} \\ &= \frac{P_g R_0 \left(E_H - \nu_H \dot{\sigma}_L\right)}{E_H t - P_g R_0} + \frac{\dot{P}_g R_0 E_H t \left(E_H - \nu_H \sigma_L\right)}{\left(E_H t - P_g R_0\right)^2}\end{aligned} \tag{A-18}$$

A more accurate expression is found by differentiating Equation (A-18), but is not used here to avoid the complication of incorporating $\dot{R}_x$. To simplify subsequent calculations, hoop stress rate is simplified to its partial derivatives

$$\dot{\sigma}_H = \sigma_{H,P}\, \dot{P} + \sigma_{H,\sigma_L}\, \dot{\sigma}_L \tag{A-19}$$

where

$$\sigma_{H,P} = \frac{R_0 E_H t \left(E_H - \nu_H \sigma_L\right)}{\left(E_H t - P_g R_0\right)^2} \tag{A-20}$$

$$\sigma_{H,\sigma_L} = \frac{-\nu_H P_g R_0}{E_H t - P_g R_0} \tag{A-21}$$

d. Differential Form of Longitudinal Stress.

Likewise, the airbag volume change rate is a function of longitudinal stress rate. As shown in Chapter 4, Volume depends only on the kinematic state variables z, ε_H, and ε_L. Hence the equation for $\dot{V}$ depends on the partial derivatives of V with respect to those variables multiplied by $\dot{z}$, $\dot{\varepsilon}_H$, and $\dot{\varepsilon}_L$ respectively.

$$\dot{V} = V_{,z}\, \dot{z} + V_{,\varepsilon_H}\, \dot{\varepsilon}_H + V_{,\varepsilon_L}\, \dot{\varepsilon}_L = V_{,z}\, \dot{z} + \left\{V_{,\varepsilon}\right\}^T \left[C\right] \begin{Bmatrix} \dot{\sigma}_H \\ \dot{\sigma}_L \end{Bmatrix} \tag{A-22}$$

Alternatively,

$$\dot{V} = V_{,z}\,\dot{z} + \{V_{,\sigma}\}^T \begin{Bmatrix} \dot{\sigma}_H \\ \dot{\sigma}_L \end{Bmatrix} = V_{,z}\,\dot{z} + V_{,\sigma_H}\,\dot{\sigma}_H + V_{,\sigma_L}\,\dot{\sigma}_L \tag{A-23}$$

where

$$\{V_{,\sigma}\}^T = \{V_{,\varepsilon}\}^T [C] \tag{A-24}$$

Substituting (3–36) into Equation (A-17) yields

$$\begin{aligned} & P_f \left(V_{,z}\,\dot{z} + V_{,\sigma_H} \left(\sigma_{H,P}\,\dot{P} + \sigma_{H,\sigma_L}\,\dot{\sigma}_L \right) + V_{,\sigma_L}\,\dot{\sigma}_L \right) \\ & = M\left(g+\ddot{z}\right)\dot{z} + A_{Lf} t \left(\left(\sigma_{H,P}\,\dot{P} + \sigma_{H,\sigma_L}\,\dot{\sigma}_L \right) \varepsilon_H + \dot{\sigma}_L \varepsilon_L \right) \\ & \quad + \dot{\sigma}_L t \frac{\sigma_L}{E_L} \left(A_{side} + 2\left(1-\nu_L\right) A_{face} \right) \\ & \quad + \dot{A}_{Lf} \frac{t}{2} \left(\sigma_H \varepsilon_H + \sigma_L \varepsilon_L \right) + \frac{\sigma_L^2}{E_L} \frac{t}{2} \left(\dot{A}_{side} + 2\left(1-\nu_L\right) \dot{A}_{face} \right) \end{aligned} \tag{A-25}$$

Collecting terms and rearranging, separates out $\dot{\sigma}_L$.

$$\begin{aligned} \dot{\sigma}_L = \frac{\left\{ M\left(g+\ddot{z}\right)\dot{z} - P_f \left(V_{,z}\,\dot{z} + V_{,\sigma_H}\,\sigma_{H,P}\,\dot{P} \right) + A_{Lf} t \sigma_{H,P}\,\dot{P}\varepsilon_H \right.}{\left. + \dot{A}_{Lf} \frac{t}{2} \left(\sigma_H \varepsilon_H + \sigma_L \varepsilon_L \right) + \frac{\sigma_L^2}{E_L} \frac{t}{2} \left(\dot{A}_{side} + 2\left(1-\nu_L\right) \dot{A}_{face} \right) \right\}} \\ \left\{ P_f \left(V_{,\sigma_H}\,\sigma_{H,\sigma_L} + V_{,\sigma_L} \right) - A_{Lf} t \left(\sigma_{H,\sigma_L}\,\varepsilon_H + \varepsilon_L \right) \right. \\ \left. - \frac{\sigma_L t}{E_L} \left(A_{side} + 2\left(1-\nu_L\right) A_{face} \right) \right\} \end{aligned} \tag{A-26}$$

To simplify subsequent control volume calculations for $\dot{P}$, longitudinal stress rate is simplified to its partial derivatives

$$\dot{\sigma}_L = \dot{\sigma}_{L,\dot{P}}\,\dot{P} + \dot{\sigma}_{L,\dot{z}}\,\dot{z} \tag{A-27}$$

where

$$\dot{\sigma}_{L,\dot{P}} = \frac{A_{Lf} t \sigma_{H,P}\, \varepsilon_H - V_{,\sigma_H}\, \sigma_{H,P}\, P_f}{\left\{ P_f \left(V_{,\sigma_H}\, \sigma_{H,\sigma_L} + V_{,\sigma_L} \right) - A_{Lf} t \left(\sigma_{H,\sigma_L}\, \varepsilon_H + \varepsilon_L \right) - \frac{\sigma_L t}{E_L} \left(A_{side} + 2\left(1-\nu_L\right) A_{face} \right) \right\}} \tag{A-28}$$

$$\dot{\sigma}_{L,\dot{z}} = \frac{M\left(g+\ddot{z}\right) - V_{,z}\, P_f + A_{Lf,z} \frac{t}{2} \left(\sigma_H \varepsilon_H + \sigma_L \varepsilon_L \right) + \frac{\sigma_L^2}{E_L} \frac{t}{2} \left(A_{side,z} + 2\left(1-\nu_L\right) A_{face,z} \right)}{P_f \left(V_{,\sigma_H}\, \sigma_{H,\sigma_L} + V_{,\sigma_L} \right) - A_{Lf} t \left(\sigma_{H,\sigma_L}\, \varepsilon_H + \varepsilon_L \right) - \frac{\sigma_L t}{E_L} \left(A_{side} + 2\left(1-\nu_L\right) A_{face} \right)} \tag{A-29}$$

A_{Lf}, A_{side}, and A_{face} are functions of z only; therefore, $A_{Lf} = A_{Lf,z}\, \dot{z}$, $A_{face} = A_{face,z}\, \dot{z}$, and $A_{side} = A_{side,z}\, \dot{z}$.

REPORT DOCUMENTATION PAGE

Form Approved
OMB No. 074-0188

PLEASE DO NOT RETURN YOUR FORM TO THE ABOVE ADDRESS.

1. REPORT DATE *(DD-MM-YYYY)*	**2. REPORT TYPE**	**3. DATES COVERED** *(From – To)*
12-03-2007	**Doctoral Dissertation**	Jan 1998 – Mar 2007

4. TITLE AND SUBTITLE

Dynamic Response of a Collidant Impacting a Low Pressure Airbag

5a. CONTRACT NUMBER

5b. GRANT NUMBER

5c. PROGRAM ELEMENT NUMBER

6. AUTHOR(S)

Dreher, Peter, A.

5d. PROJECT NUMBER

5e. TASK NUMBER

5f. WORK UNIT NUMBER

7. PERFORMING ORGANIZATION NAMES(S) AND ADDRESS(S)

Air Force Institute of Technology
Graduate School of Engineering and Management (AFIT/EN)
2950 Hobson Way
WPAFB OH 45433-7765

8. PERFORMING ORGANIZATION REPORT NUMBER

AFIT/DS/ENY/07-09

9. SPONSORING/MONITORING AGENCY NAME(S) AND ADDRESS(ES)

10. SPONSOR/MONITOR'S ACRONYM(S)

11. SPONSOR/MONITOR'S REPORT NUMBER(S)

12. DISTRIBUTION/AVAILABILITY STATEMENT

APPROVED FOR PUBLIC RELEASE; DISTRIBUTION UNLIMITED.

13. SUPPLEMENTARY NOTES

14. ABSTRACT

There are many uses of low pressure airbags, both military and commercial. Many of these applications have been hampered by inadequate and inaccurate modeling tools.

This dissertation contains the derivation of a four degree-of-freedom system of differential equations from physical laws of mass and energy conservation, force equilibrium, and the Ideal Gas Law. Kinematic equations were derived to model a cylindrical airbag as a single control volume impacted by a parallelepiped collidant. An efficient numerical procedure was devised to solve the simplified system of equations in a manner amenable to discovering design trends. The largest public airbag experiment, both in scale and scope, was designed and built to collect data on low-pressure airbag responses, otherwise unavailable in the literature. The experimental results were compared to computational simulations to validate the simplified numerical model. Experimental response trends are presented that will aid airbag designers. The two objectives of using a low pressure airbag to demonstrate the feasibility to 1) accelerate a munition to 15 feet per second velocity from a bomb bay, and 2) decelerate humans hitting trucks below the human tolerance level of 50 G's, were both met.

15. SUBJECT TERMS

Dynamics

16. SECURITY CLASSIFICATION OF:			**17. LIMITATION OF ABSTRACT**	**18. NUMBER OF PAGES**	**19a. NAME OF RESPONSIBLE PERSON**
REPORT	**ABSTRACT**	**c. THIS PAGE**			Dr. Robert A. Canfield PhD
U	**U**	**U**	**UU**	211	**19b. TELEPHONE NUMBER** *(Include area code)* (937) 255-6565, ext 4723; e-mail: Robert.Canfield@afit.edu

NONPRINT FORM

1. Type of Product:	2. Operating System/Version:	3. New Product or Replacement:	4. Type of File:
Dissertation Data	Microsoft XP	New Product	Spreadsheets

5. Language/Utility Program:

Microsoft Excel

6. # of Files/# of Products:	7. Character Set:	8. Disk Capacity:
453	N/A	N/A
	9. Compatibility:	**10. Disk Size:**
	N/A	N/A

11. Title:

Dynamic Response of a Collidant Impacting a Low Pressure Airbag

12. Performing Organization:	13. Performing Report #:	14. Contract #:
AFIT/ENY	AFIT/DS/ENY/07-09	N/A
		15. Program Element #:
		N/A

16. Sponsor/Monitor:	17. Sponsor/Monitor # Acronym:	19. Project #:
N/A	N/A	N/A
	18. Sponsor/Monitor #:	**20. Task #:**
	N/A	N/A
		21. Work Unit #:
		N/A

22. Date:	23. Classification of Product:
March 12, 2007	Unclassified
24. Security Classification Authority:	**25. Declassification/Downgrade Schedule:**

26. Distribution/Availability:

APPROVED FOR PUBLIC RELEASE; DISTRIBUTION UNLIMITED.

NONPRINT FORM

27. Abstract:

There are many uses of low pressure airbags, both military and commercial. Many of these applications have been hampered by inadequate and inaccurate modeling tools.

This dissertation contains the derivation of a four degree-of-freedom system of differential equations from physical laws of mass and energy conservation, force equilibrium, and the Ideal Gas Law. Kinematic equations were derived to model a cylindrical airbag as a single control volume impacted by a parallelepiped collidant. An efficient numerical procedure was devised to solve the simplified system of equations in a manner amenable to discovering design trends. The largest public airbag experiment, both in scale and scope, was designed and built to collect data on low-pressure airbag responses, otherwise unavailable in the literature. The experimental results were compared to computational simulations to validate the simplified numerical model.

28. Classification of Abstract:	**29. Limitation of Abstract:**
Unclassified	N/A

30. Subject Terms:	**30a. Classification of Subject Terms:**
Dynamics	Unclassified

31. Required Peripherals:

DVD drive

32. # of Physical Records:	**33. # of Logical Records:**	**34. # of Tracks:**
N/A	N/A	N/A

35. Record Type:	**36. Color:**	**37. Recording System:**
N/A	N/A	N/A

38. Recording Density:	**39. Parity:**	**40. Playtime:**
N/A	N/A	N/A

41. Playback Speed:	**42. Video:**	**43. Text:**	**44. Still Photos:**	**45. Audio:**
N/A	N/A	N/A	N/A	N/A

46. Other:

N/A

47. Documentation/Supplemental Information:

N/A

48. Point of Contact and Telephone Number:

Dr. Peter Dreher 937-765-0409

REPORT DOCUMENTATION PAGE

Form Approved
OMB No. 074-0188

PLEASE DO NOT RETURN YOUR FORM TO THE ABOVE ADDRESS.

1. REPORT DATE *(DD-MM-YYYY)*	**2. REPORT TYPE**	**3. DATES COVERED** *(From – To)*
12-03-2007	**Doctoral Dissertation**	Jan 1998 – Mar 2007

4. TITLE AND SUBTITLE

Dynamic Response of a Collidant Impacting a Low Pressure Airbag

5a. CONTRACT NUMBER

5b. GRANT NUMBER

5c. PROGRAM ELEMENT NUMBER

6. AUTHOR(S)

Dreher, Peter, A.

5d. PROJECT NUMBER

5e. TASK NUMBER

5f. WORK UNIT NUMBER

7. PERFORMING ORGANIZATION NAMES(S) AND ADDRESS(S)

Air Force Institute of Technology
Graduate School of Engineering and Management (AFIT/EN)
2950 Hobson Way
WPAFB OH 45433-7765

8. PERFORMING ORGANIZATION REPORT NUMBER

AFIT/DS/ENY/07-09

9. SPONSORING/MONITORING AGENCY NAME(S) AND ADDRESS(ES)

10. SPONSOR/MONITOR'S ACRONYM(S)

11. SPONSOR/MONITOR'S REPORT NUMBER(S)

12. DISTRIBUTION/AVAILABILITY STATEMENT

APPROVED FOR PUBLIC RELEASE; DISTRIBUTION UNLIMITED.

13. SUPPLEMENTARY NOTES

14. ABSTRACT

There are many uses of low pressure airbags, both military and commercial. Many of these applications have been hampered by inadequate and inaccurate modeling tools.

This dissertation contains the derivation of a four degree-of-freedom system of differential equations from physical laws of mass and energy conservation, force equilibrium, and the Ideal Gas Law. Kinematic equations were derived to model a cylindrical airbag as a single control volume impacted by a parallelepiped collidant. An efficient numerical procedure was devised to solve the simplified system of equations in a manner amenable to discovering design trends. The largest public airbag experiment, both in scale and scope, was designed and built to collect data on low-pressure airbag responses, otherwise unavailable in the literature. The experimental results were compared to computational simulations to validate the simplified numerical model. Experimental response trends are presented that will aid airbag designers. The two objectives of using a low pressure airbag to demonstrate the feasibility to 1) accelerate a munition to 15 feet per second velocity from a bomb bay, and 2) decelerate humans hitting trucks below the human tolerance level of 50 G's, were both met.

15. SUBJECT TERMS

Dynamics

16. SECURITY CLASSIFICATION OF:			**17. LIMITATION OF ABSTRACT**	**18. NUMBER OF PAGES**	**19a. NAME OF RESPONSIBLE PERSON**
REPORT	**ABSTRACT**	**c. THIS PAGE**			Dr. Robert A. Canfield PhD
U	**U**	**U**	**UU**	211	**19b. TELEPHONE NUMBER** *(Include area code)* (937) 255-6565, ext 4723; e-mail: Robert.Canfield@afit.edu